# Asymmetric Cessna Citation II Stall Model Identification using a Roll moment-based Kirchhoff method

**MSc Thesis**

D. de Fuijk

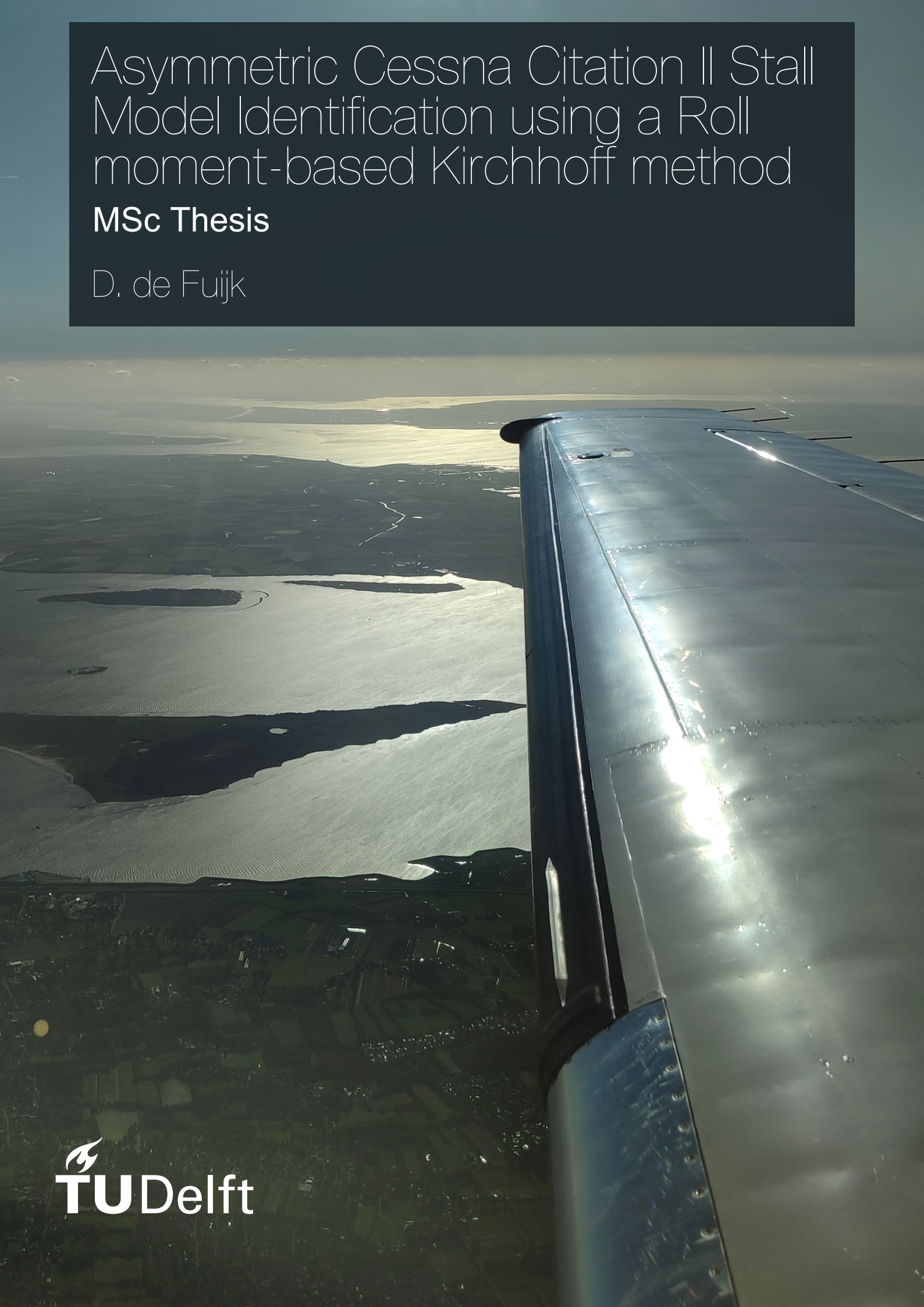

TU Delft

# Asymmetric Cessna Citation II Stall Model Identification using a Roll moment-based Kirchhoff method

MSc Thesis

by

D. de Fuijk

to obtain the degree of Master of Science
at the Delft University of Technology
to be defended publicly on August 30, 2023 at 13:00

*Thesis committee*:

| | | |
|---|---|---|
| Chair: | Dr.ir. C.C. de Visser | TU Delft, AE, Control & Simulation |
| Supervisors: | Dr.ir. C.C. de Visser | |
| | Dr.ir. D.M. Pool | TU Delft, AE, Control & Simulation |
| External examiner: | Dr. S.J. Hulshoff | TU Delft, AE, Aerodynamics |
| Place: | Faculty of Aerospace Engineering, Delft | |
| Project Duration: | September, 2022 - August, 2023 | |
| Student number: | 4562968 | |

An electronic version of this thesis is available at `http://repository.tudelft.nl/`.

Faculty of Aerospace Engineering · Delft University of Technology

# Preface

This work presents the culmination of my research efforts in the final year of my Master education in Aerospace Engineering. Almost an entire year's worth of hard work, exciting new experiences, and a lot of trial-and-error have led to the output in this report. I can honestly say that I am proud of the result, which was my main objective when first diving into these models and literature. When reading this work, I hope you find that it has made a contribution, however small, to the overarching objective of effective aircraft stall pilot training in simulators.

It was my personal goal to complete the Master in 2 years. After delaying my Bachelor graduation, I felt it was time to pick up the pace. By setting my graduation date right before the 2-year deadline, I am proud to say that I am still on the right track. Achieving this required a lot of motivation. Admittedly, it was not too difficult to motivate myself when Coen and Daan — my supervisors — mentioned that we would be able to conduct our own stall flight tests, hardly a month into my thesis work. Flying these experiments was an occasion that one would usually never get the chance to experience. It was worth all the motion sickness that comes with flying about 20 stall maneuvers in roughly an hour's time. As a bonus, I got some useful data out of it! I would like to thank Dr.ir. Alexander in 't Veld and ir. Hans Mulder for their hard work and enthusiasm in the cockpit, trying to get the PH-LAB to do all these extreme things we asked for.

While I am thanking people, Coen en Daan must be mentioned again. Every so-called "stall meeting" has been a pleasure, with a great combination of lightheartedness and serious, unfiltered feedback. For every meeting, I found myself going in with a million questions and ideas, and coming out with my head cleared and my priorities straight. This helped me to make steady progress and eventually set my own finish line. I would also like to thank Dr. Steven Hulshoff for taking place on the graduation committee. Patrick and Sybren, for making the stall meetings fun and relatable. My friends, for sticking together while we are slowly scattering away from university and Delft. My family, for always being supportive and trusting my decisions. Last but not least, I want to thank Irene for pushing me to be the best version of myself.

On a technical note, I would like to provide you with some structure. This thesis report consists of 4 parts. First, a general introduction of the thesis is given, defining the research objectives and questions. Then, the scientific paper is presented, providing the most important results and conclusions. Subsequently, the literature study and some preliminary work are included in the preliminary thesis report. Finally, the thesis conclusion provides an overview of the findings of the entire research.

# Contents

# Nomenclature

## Abbreviations

| Abbreviation | Definition |
|---|---|
| AHRS | Attitude and Heading Reference System |
| AOA | Angle Of Attack |
| AWS | Abrupt Wing Stall |
| CG | Center of Gravity |
| CAST | Commercial Aviation Safety Team |
| CICTT | AST/ICAO Common Taxonomy Team |
| DADC | Digital Air Data Computer |
| DOF | Degree Of Freedom |
| ECEF | Earth-centered Earth-fixed (reference frame) |
| EKF | Extended Kalman Filter |
| FAA | Federal Aviation Administration |
| FL | Flight Level |
| FPR | Flight Path Reconstruction |
| FSTD | Flight Simulation Training Device |
| FTC | Flight Test Card |
| FTIS | Flight Test Instrumentation System |
| GPS | Global Positioning System |
| ICAO | International Civil Aviation Organization |
| ICATEE | International Committee for Aviation Training in Extended Envelopes |
| IEKF | Iterated Extended Kalman Filter |
| KF | Kalman Filter |
| LE | Leading Edge |
| LOC-I | Loss of control In-flight |
| MOF | Multivariate Orthogonal Functions |
| MSE | Mean Square Error |
| NASA | National Aeronautics and Space Administration |
| NLR | Netherlands Aerospace Center |
| OLS | Ordinary Least Squares |
| PSE | Predicted Square Error |
| QR | Quasi-random (disturbance inputs) |
| RMS | Root Mean Square |
| SQP | Sequential Quadratic Programming |
| TAS | Total Airspeed |
| TE | Trailing Edge |
| UKF | Unscented Kalman Filter |
| WLS | Weighted Least Squares |

# Roman Symbols

| Symbol | Definition | Unit |
|---|---|---|
| $A$ | Acceleration / Regression matrix | $\mathrm{m}/\mathrm{s}^2$ / - |
| $a$ | Upper bound of a model term | - |
| **a** | The set of regression variables | - |
| $a_1$ | Kirchhoff's flow separation shaping parameter | - |
| $C$ | Aerodynamic coefficient | - |
| $c$ | Normal coordinate to airfoil surface | m |
| $\bar{c}$ | Mean aerodynamic chord | m |
| $e$ | Oswald's efficiency number | - |
| $G$ | Time-derivative of the flow separation point | - |
| $g_0$ | Gravitational acceleration constant | $\mathrm{m}/\mathrm{s}^2$ |
| $\mathbf{H}_J$ | Hessian matrix of cost function $J$ | - |
| $J$ | Cost function | - |
| $L$ | Dimension of the augmented state vector | - |
| $L_f$ | Lie derivative operator | - |
| $p$ | Roll rate | $\mathrm{rad}\,\mathrm{s}^{-1}$ |
| $P$ | Auto-covariance matrix of the UKF state | - |
| **p** | The set of orthogonalized regression variables | - |
| $\mathcal{O}$ | Observability matrix | - |
| $q$ | Pitch rate | $\mathrm{rad}\,\mathrm{s}^{-1}$ |
| $Q$ | Process noise covariance matrix of the UKF | - |
| $r$ | Yaw rate | $\mathrm{rad}\,\mathrm{s}^{-1}$ |
| $R$ | Observation noise covariance matrix of the UKF | - |
| $R^2$ | Coefficient of determination | - |
| $S$ | Partial derivative of $X$ w.r.t. $X$-parameters | - |
| $u$ | Velocity along body $x$-axis | $\mathrm{m}\,\mathrm{s}^{-1}$ |
| $U$ | Theil's statistic | - |
| **u** | UKF input vector | - |
| $V$ | Velocity | $\mathrm{m}\,\mathrm{s}^{-1}$ |
| $v$ | Velocity along body $y$-axis | $\mathrm{m}\,\mathrm{s}^{-1}$ |
| **v** | UKF process noise vector | - |
| VAF | Variance accounted for | - |
| $w$ | Velocity along body $z$-axis | $\mathrm{m}\,\mathrm{s}^{-1}$ |
| $W$ | UKF Sigma point weight / Wind velocity | - / $\mathrm{m}\,\mathrm{s}^{-1}$ |
| $w$ | Sensor noise | - |
| $w_N$ | Standard normally distributed random variable | - |
| $X$ | Flow separation point | - |
| $x$ | Position along $x$-axis of a given coordinate system | m |
| $\mathcal{X}$ | Sigma-points set around UKF state estimate | - |
| **x** | UKF state vector | - |
| $y$ | Position along $y$-axis of a given coordinate system | m |
| **y** | UKF measurements vector | - |
| $\mathcal{Y}$ | Sigma-points set around UKF measurement prediction | - |
| $z$ | Position along $z$-axis of a given coordinate system | m |

# Greek Symbols

| Symbol | Definition | Unit |
|---|---|---|
| $\alpha$ | Angle of attack / UKF spreading parameter | rad / - |
| $\beta$ | Angle of sideslip / UKF tuning parameter | rad / - |
| $\tau_1$ | Kirchhoff's time constant of lag | s |
| $\tau_2$ | Kirchhoff's time constant of aerodynamic hysteresis | s |
| $\alpha^\star$ | Kirchhoff's flow separation scheduling parameter | rad |
| $\delta_*$ | Deflection of control surface * | rad |
| $\Lambda$ | Wing aspect ratio | - |
| $\lambda$ | UKF scaling parameter / sensor bias | - / - |
| $\kappa$ | UKF spreading parameter | - |
| $\phi$ | Roll angle | rad |
| $\theta$ | Pitch angle / Parameter vector | rad / - |
| $\psi$ | Yaw angle | rad |
| $\Gamma$ | Orthogonalization matrix | - |
| $\hat{\phi}$ | The maximum-likelihood parameters | - |
| $\sigma$ | Standard deviation | - |
| $\rho_{xy}$ | The cross-correlation between variables $x$ and $y$ | - |

## Subscripts

| Symbol | Definition |
|---|---|
| $0$ | Steady-state |
| $a$ | Aileron |
| $D$ | Drag force |
| $E$ | Earth-fixed reference frame |
| $e$ | Elevator |
| $k$ | Time step k |
| $L$ | Lift force / Left wing |
| $l$ | Roll moment / Airfoil or section lift force |
| $m$ | Pitch moment |
| $n$ | Yaw moment |
| $P$ | Point in a given coordinate system |
| $R$ | Right wing |
| $r$ | Rudder |
| $si$ | sidewash |
| $t$ | Horizontal tail |
| $up$ | Upwash |
| $w$ | Specified wing |
| $wb$ | Wing body |
| $Y$ | Lateral force |

## Superscripts

| Symbol | Definition |
|---|---|
| $\dot{}$ | Time derivative |
| $\hat{}$ | Estimate |
| $\tilde{}$ | Non-dimensionalized variable |
| a | Augmented |
| $m$ | UKF Weights for new state estimate |
| $c$ | UKF Weights for updated covariance matrix |

# List of Figures

# List of Tables

# Part I

# Thesis Introduction

*As this part was originally included in the preliminary report, it has been assessed for the course AE4020 Literature Study.

# Introduction

The largest contributor to fatal flight accidents is Loss of Control - In Flight (LOC-I), as categorized by the AST/ICAO Common Taxonomy Team (CICTT) [1, 2]. This categorization includes incidents related to aerodynamic stall: the highly nonlinear, unsteady and unpredictable state of an aircraft that occurs when airflow over a wing separates from the surface. As a result, the Federal Aviation Administration (FAA) imposed that from 2019 onwards, all civil aviation pilots require training on recognizing, preventing, and recovering aerodynamic stall [3]. This training is largely performed in flight simulators, due to cost and safety concerns. In general, the fidelity of the current flight simulators is limited in the stall regime. For this reason, the FAA has recently released updated simulator stall model qualification requirements [3]. A stall modeling task force was founded at the Control and Simulation department of the TU Delft Aerospace Engineering faculty, with the objective to develop stall modeling methods, that serve the higher goal of effective pilot stall training, at a relatively low cost.

The International Committee for Aviation Training in Extended Envelopes (ICATEE) identified a set of key characteristics that must be represented in the stall and post-stall flight model [4]. These characteristics include longitudinal and lateral-directional effects. Many of the longitudinal effects have been successfully identified by system identification research [5, 6, 7, 8, 9]. However, the lateral-directional effects have proved difficult to identify with these techniques. These methodologies describe stall effects for the entire wing, while flow separation properties can differ per span-wise location on the wing.

Some lateral-directional stall effects can be explained by the concept of asymmetric stall. While in the earlier-mentioned research, flow separation is described over a single span-wise location, asymmetric stall describes that the wing surfaces do not stall simultaneously. Several identification attempts take this phenomenon into account by considering the stall-related variables on each wing separately [10, 11, 12].

This work builds on a baseline model, created through earlier efforts from the task force [13, 9]. The focus of this research is on applying modifications that allow for modeling asymmetric stall effects and potential variations in lateral-directional control surface effectiveness.

## Research Objective

A set of objectives was generated that describes the focus of this work. The primary research objective of this thesis is described as follows:

**Research Objective**

To improve the model fidelity of the Cessna Citation II dynamic stall model by applying asymmetric stall modifications and to identify variations in lateral-directional control effectiveness by using system identification techniques, applied to specifically gathered flight data.

The primary research objective is split into a set of sub-objectives:

1. To gather flight test data that are suitable for the identification of lateral-directional stall behavior and asymmetric stall characteristics.
2. To process the newly gathered flight data and select the maneuvers from the overall database that allows for the identification of a model that describes longitudinal and lateral-directional behavior.
3. To obtain an optimal aircraft state estimate from the gathered flight data, by applying a readily available Unscented Kalman Filter.
4. To design a suitable parameter estimation methodology and accurately estimate the parameters of the selected model structure.
5. To select a model structure that enables the representation of the asymmetric stall characteristics and variations in control surface effectiveness, and of which the parameters can be accurately estimated with the selected flight data.
6. To verify and validate the identified stall model using a subset of the selected flight data that was not used for identification.

## Research Question

In order to maintain focus on the relevant tasks to be completed several research questions are developed. The main research question of this thesis goes as follows:

**Main Research Question**

How can the asymmetric stall behavior and variations in lateral-directional control effectiveness of a Cessna Citation II aircraft best be identified from flight test data and included in the existing dynamic stall model?

Similarly to the research objective, the research question is split into focused sub-questions:

**Research Question 1**

Which flight test maneuvers and control inputs are suitable for identifying lateral-directional stall behavior, including potential variations in control surface effectiveness?

**Research Question 2**

How can the local angle of attack of the aircraft wings be determined?

**Research Question 3**

Which nonlinear parameter estimation methodology is suitable for efficient and sufficiently accurate estimation of the parameters of the selected stall model structure from flight data?

**Research Question 4**

How can the parameters that describe the flow separation point be identified from the flight-derived roll moment coefficient and a suitable roll moment model structure?

**Research Question 5**

What modifications to Kirchhoff's flow separation model are required to enable it to effectively model asymmetric stall behavior and variations in control surface effectiveness?

## Research Methodology

The structuring of this thesis is similar to the general system identification framework and it is visually presented in Figure 1.

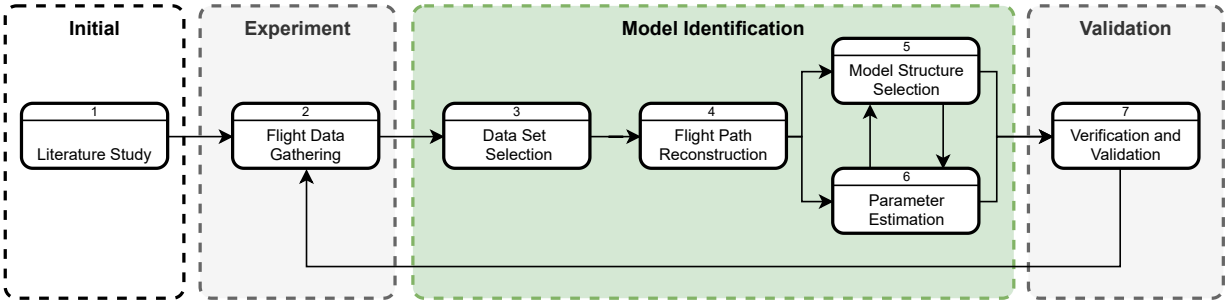


**Figure 1:** The research methodology and structure of the thesis.

**Initial phase** An extensive literature study is performed in the initial phase. The findings are reported in Chapter 1. Note that literature was consulted frequently in the subsequent phases, but the baseline that was required for the experiment phase was made in the initial phase.

**Experiment phase** The experiment phase consists of the experiment design, planning, and execution. The conducted experiments were specifically designed to induce asymmetric stall effects. The decisions that were made are presented in Chapter 2.

**Model identification phase** The first step of the model identification phase is the data set selection. In order to obtain a stall model that explains specific (asymmetric) stall effects, a careful selection of maneuvers must be included in the data set. Moreover, two complete data sets are introduced and compared at a later stage. The relevant choices are documented in Chapter 2.

Flight path reconstruction is applied to the raw data in order to minimize the effect of measurement errors and obtain an optimal state estimate. The type of Kalman Filter implementation is selected and analyzed based on the findings of previous work at the research group [13, 9]. Some modifications in the model equations are suggested for application in this thesis. This step is presented in Chapter 3.

The model structure selection and the parameter estimation steps are iterative in nature. The details and interaction of these steps are explained in Chapter 4 and Chapter 5, respectively. Note that an important research objective, modeling potential variations in control surface effectiveness, is both a matter of model structure selection and parameter estimation.

**Validation phase** The results of the model identification phase are interpreted through the validation step. The data sets are split into a training set and a validation set. The model identification phase makes use of the training set, while the validation phase uses the validation set. Through validation, important conclusions can be made about the model's quality. Chapter 4 and Chapter 5 include descriptions of validation steps to be taken at a later stage in this research.

# Part II

## Scientific Paper

# Asymmetric Cessna Citation II Stall Model Identification using a Roll moment-based Kirchhoff method

Dirk de Fuijk *
*Faculty of Aerospace Engineering, Delft University of Technology, Delft, The Netherlands*

**Adequate modeling of the unsteady aerodynamics during flow separation is critical for effective pilot training in Flight Simulation Training Devices. Over the years, a stall modeling method rooted in Kirchhoff's theory of flow separation has gained popularity due to its relative simplicity and suitability for parameter identification from flight data. This method describes the lift using a single internal flow separation point variable. A major drawback of Kirchhoff's method comes from the one-dimensionality of the flow separation point, limiting the representation of asymmetric flow separation. The goal of this work is to improve the existing Cessna Citation II dynamic stall model fidelity by applying Kirchhoff's method for each wing surface, separately. The main contribution is the identification of asymmetric flow separation development, using the flight-derived roll moment and a roll moment model based on the differential flow separation between the wing surfaces. Transformations of the flow separation variables were chosen by a Multivariate Orthogonal Functions selection algorithm to capture the stall-related nonlinearities of the roll moment, yaw moment, and lateral force. The longitudinal model structures are adopted from the existing, validated baseline stall model. The lateral-directional model outputs are in good agreement with the validation flight data, showing an average reduction of 48% in Mean Squared Error (MSE) compared to the baseline stall model. In contrast, the longitudinal model output results in an average MSE increase of 88%, suggesting that the estimated asymmetric flow separation parameters are unsuitable for longitudinal stall modeling. A promising way to incorporate the benefits of the proposed method is suggested, by adopting a hybrid approach that combines separate sets of flow separation parameters — symmetric and asymmetric variants — for the longitudinal and lateral-directional models, respectively.**

## Nomenclature

*Roman Symbols*

| | | |
|---|---|---|
| $a$ | = | Linear acceleration [m/s$^2$] |
| $\mathbf{a}$ | = | Regression variable vector |
| $A$ | = | Regression matrix |
| $a_1$ | = | Flow separation parameter - shaping [-] |
| $b$ | = | Aircraft wing span [m] |
| $\bar{c}$ | = | Mean chord length [m] |
| $C_*$ | = | Aerodynamic force/moment coefficient [-] |
| $I_*$ | = | Mass moment of inertia about *-axis [kgm$^2$] |
| $J$ | = | Objective function value [-] |
| $l$ | = | Aircraft length [m] |
| $m$ | = | Aircraft mass [kg] |
| $M$ | = | Mach number [-] |
| $n$ | = | Load factor [-] (unless otherwise specified) |
| $N$ | = | Number of data points |
| $\mathbf{p}$ | = | Orthogonalized regression variable vector |
| $p, q, r$ | = | Pitch / roll / yaw rate [rad/s] |
| $R^2$ | = | Explained variance [-] |
| $S$ | = | Wing surface aera [m$^2$] |
| $X$ | = | Flow separation point variable [m] |
| $y_w$ | = | Moment arm of single-wing lift vector [m] |

*Greek Symbols*

| | | |
|---|---|---|
| $\alpha$ | = | Angle of attack [°] |
| $\alpha^*$ | = | Flow separation scheduling parameter [rad] |
| $\beta$ | = | Sideslip angle [°] |
| $\Delta K_\alpha$ | = | Kirchhoff regressors differential [-] |
| $\delta_a$ | = | Aileron deflection [°] |
| $\delta_e$ | = | Elevator deflection [°] |
| $\delta_r$ | = | Rudder deflection [°] |
| $\epsilon$ | = | Residual vector |
| $\gamma_{k,j}$ | = | Gram-Schmidt scaling parameter [-] |
| $\phi$ | = | Bank angle [°] / orthogonal parameter vector |
| $\psi$ | = | Heading angle [°] |
| $\rho$ | = | Pearson's linear correlation coefficient [-] |
| $\sigma$ | = | Standard deviation |
| $\sigma_y$ | = | Scaling parameter for PSE metric [-] |
| $\tau_1$ | = | Flow separation parameter, transient effects [s] |
| $\tau_2$ | = | Flow separation parameter, quasi-steady effects [s] |
| $\theta$ | = | Pitch angle [°] / parameter vector |

*MSc Student, Control & Simulation, Faculty of Aerospace Engineering, d.defuijk@gmail.com.

*Subscripts*

| | | |
|---|---|---|
| 0 | = | Steady state / Initial value |
| $b$ | = | Body-fixed reference frame |
| $D$ | = | Drag force |
| $l$ | = | Roll moment |
| $L$ | = | Lift force / Left wing |
| $m$ | = | Pitch moment |
| $n$ | = | Yaw moment |
| $R$ | = | Right wing |
| $T$ | = | Thrust force |
| $Y$ | = | Lateral force |

*Superscripts*

| | | |
|---|---|---|
| $\bar{}$ | = | Mean value |
| $\dot{}$ | = | Time-derivative |
| $\hat{}$ | = | Estimate |
| $^\top$ | = | Transpose vector |

# I. Introduction

Aerodynamic forces and moment models are traditionally based on stability and control derivatives [1]. This approach has led to adequate dynamic aircraft models for the nominal flight envelope. However, in the stall and post-stall flight conditions, aerodynamic forces and moments exhibit nonlinear and noticeable unsteady effects as a result of aircraft motion. Furthermore, the effectiveness of a control surface can be reduced due to potential interactions with the turbulent wake resulting from separated flow. A recent study conducted wind tunnel experiments with a scaled aircraft model to investigate lateral control authority during stall, identifying a reduction of approximately 40% in aileron effectiveness [2].

Adequate modeling of the unsteady aerodynamics during flow separation is critical for pilot training in Flight Simulation Training Devices (FSTDs), for upset situations and loss-of-control in flight (LOC-I) [3, 4], as nearly 40% of LOC-I accidents are categorized as stall-related [5].

Recently, Computational Fluid Dynamics (CFD) methods have been employed to evaluate entire aircraft stall models [6]. The EU-funded project "Simulation of Upset Recovery in Aviation" (SUPRA) introduced a complex approach, based on wind tunnel data and complemented by CFD analysis [4, 7]. While these methods can achieve high levels of accuracy, they often come with the drawbacks of being computationally expensive and requiring rigorous validation procedures. Hence, model identification from flight data remains relevant.

A popular stall modeling approach is based on Kirchhoff's theory of flow separation. First introduced by Goman and Khrabrov [8], Kirchhoff's method aims to model the lift using an internal flow separation variable $X$, a coordinate describing the location of the flow separation point on the upper airfoil surface. Conveniently, this variable has also been shown to adequately model the nonlinearities of the drag and the pitch moment [9, 10]. A direct measurement of the flow separation point is difficult to obtain. Alternatively, it has been approximated using a first-order ordinary differential equation (ODE), of which the parameters are estimated from wind tunnel tests, flight data, or a combination of the two [9–11]. The main limitation of Kirchhoff's method is that the flow separation point is generally considered as a one-dimensional coordinate, rendering it unsuitable for describing any flow separation asymmetry. To combat this issue, Singh and Jategaonkar [12] modeled the normal force of each wing separately using Kirchhoff's theory, whereas Lutze et al. [13] included additional lift surfaces and applied a quadratic polynomial approximation. This paper explores variants of both approaches.

This paper is part of a series of efforts at the TU Delft Faculty of Aerospace Engineering. Initially, a partial stall model of a Cessna Citation II research aircraft was created based on Kirchhoff's method, which was limited to the longitudinal dynamics [14]. The model was then extended to include estimates of the lateral-directional coefficients. Moreover, an algorithm based on multivariate orthogonal functions was employed for model structure selection, and an efficient nonlinear parameter identification methodology was introduced [15]. The flow separation parameters were identified solely from flight data. This work also identified a reduction in elevator effectiveness in stall, using the damping effect of the flow separation variable. The resulting stall model showed good longitudinal performance, but no flow separation description was included in the lateral-directional model structures, leading to a lacking representation of the associated nonlinearities. This model will be referred to as the baseline stall model.

The goal of this work is to improve the Cessna Citation II dynamic stall model fidelity by applying asymmetric stall modifications to Kirchhoff's method. The main contribution is the identification of asymmetric flow separation development, using the flight-derived roll moment and a roll moment model based on the differential flow separation between the wing surfaces. Additionally, an attempt is made to identify any variations in lateral-directional control effectiveness. To reach the set objectives, flight experiments were conducted using TU Delft's laboratory aircraft, dedicated to gathering data containing strong asymmetric and dynamic excitation, as well as control surface deflections

during a set of stall maneuvers. The flow separation parameters are identified through a nonlinear optimization, and the resulting separation variables are subsequently treated as fixed internal state variables. For this purpose, a roll-moment model structure is selected based on an analysis of Kirchhoff's model and an alternative first-order approximation.

The performed flight experiments and the resulting data are detailed in Section II. Subsequently, the system identification methodology is explained in Section III. Section IV presents the results of the model identification and validation processes. The results are further interpreted and discussed in Section V, after which conclusions are finally drawn in Section VI.

## II. Flight Experiments and Data

### A. Flight Experiments

*1. Research Aircraft*

All flight experiments were conducted with a Cessna Citation II (550) aircraft (PH-LAB), a twinjet originally built for executive travel. It is co-owned by TU Delft and Netherlands Aerospace Center (NLR). A comprehensive Flight Test Instrumentation System (FTIS) is installed, which aggregates all the measurement data from the sensors. A crucial part of the measurement equipment is the air data boom connected to the aircraft nose, as highlighted along with the body-fixed reference frame in Fig. 1. This device allows for accurate measurements of the airflow angles.

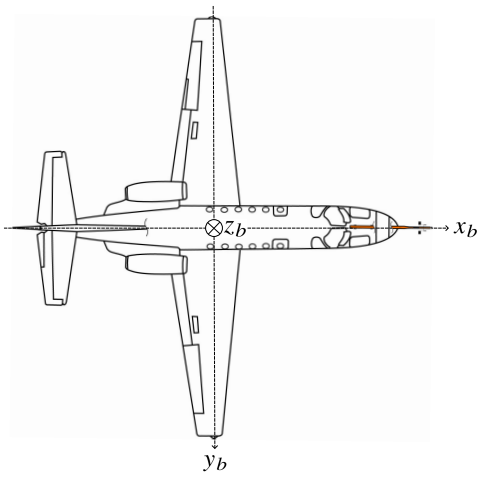


**Fig. 1 Top view of the research aircraft, including the body-fixed reference frame and a highlighted air data boom. Adapted from van Ingen et al. [15].**

**Table 1 Cessna Citation II general specifications.**

| Dimensions | | | Mass and inertia | | |
|---|---|---|---|---|---|
| $b$ | 15.9 | m | MTOW | 6600 | kg |
| $l$ | 14.4 | m | MLW | 6100 | kg |
| $\bar{c}$ | 2.09 | m | $m_{\text{dry}}$ | 4157 | kg |
| $S$ | 30.0 | $m^2$ | $I_{xx}$ | 12392 | $kgm^2$ |
| | | | $I_{yy}$ | 31501 | $kgm^2$ |
| | | | $I_{zz}$ | 41908 | $kgm^2$ |
| | | | $I_{xz}$ | 2252.2 | $kgm^2$ |

*2. Experiment Design*

All new stall maneuvers were conducted in clean configuration, between Flight Level (FL) 150 and 200. Since a large bulk of the previous stall data was gathered at this altitude, this choice allows for model validation using a combination of the data sets.

The classic quasi-steady stall maneuver, during which the airspeed is reduced at approximately -1 kt/s, has proven ineffective for parameter estimation purposes [10]. In this condition, unsteady state variables such as pitch rate $q$ and angle of attack rate $\dot{\alpha}$ are close to null, while other states vary simultaneously and approximately linearly, leading to strong correlations. These conditions make parameter estimation a difficult task and any resulting model will be of a low fidelity. Instead, two types of dynamic maneuvers were applied during the stall maneuvers, quasi-random disturbance (QR) inputs and 3-2-1-1. Both input types are displayed in Fig. 2. QR refers to the pilot attempting to apply seemingly random inputs with as little correlation as possible, a piloting technique based on the description of Morelli et al. [16].

The 3-2-1-1 maneuver is a multi-step signal, originally proposed by Koehler and Wilhelm [17]. Its signal power is distributed uniformly over a wide frequency range. The naming is inspired by the time units of control surface deflection in a certain direction: 3 units positive, 2 negative, 1 positive, and 1 negative. During the experiments, a fly-by-wire system was available to apply automatic 3-2-1-1 inputs, ensuring reliable dynamic roll axis excitation [18]. To avoid reaching excessively large bank angles, it was chosen to direct the longest positive input ("3") in the opposite direction of the stall approach bank angle. Hence, all 3-2-1-1 maneuvers were initiated to the left.

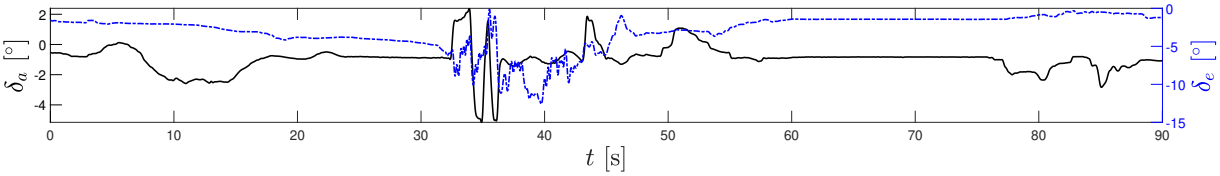


**Fig. 2 An example of a simultaneous 3-2-1-1 aileron input and a QR elevator input.**

The newly conducted experiments are exclusively $1.1g$ accelerated stalls (to the right), with the purpose of inducing asymmetric flow separation effects. The term "accelerated" refers to a stall maneuver that is performed with a reference bank angle, or load factor $n_z$. To further impose asymmetry, 6 stall maneuvers were performed with a reference sideslip angle. The objective was to reach $\beta_{\text{ref}} = 5°$, which was in practice difficult to maintain for the pilots. The fact that this choice required significant rudder inputs provided an additional benefit for parameter identification, as van Ingen et al. [15] noted that only a subset of the previous data included sufficient rudder inputs for accurate estimation of the yaw moment model parameters.

To quantify any variations in lateral-directional control surface effectiveness, control inputs must be included both in the pre-stall and post-stall region. Van Ingen et al. [15] recommended the application of dynamic inputs such as 3-2-1-1's in the pre-stall region, and including it in the data set. However, due to the limited flight time, it was chosen to abandon this approach. Instead, the pre-stall aileron inputs required for the accelerated stall approach are included.

### B. Flight Data

For this research, flight data is utilized from two recent experiments. In 2018, experiments were designed for general dynamic stall modeling [15]. In 2022, experiments were specifically designed and conducted for the current research. The primary objective of the new flight experiments was to gather flight test data suitable for the identification of lateral-directional stall behavior and asymmetric flow separation characteristics. This paper refers to two different data sets, ASYM and VAN INGEN. Table 2 contains descriptions of the stall maneuvers that are included in each set. VAN INGEN included only the maneuvers carried out in 2018, which led to the identification and validation of the baseline stall model [15]. These experiments consisted of wing-level symmetric and accelerated stall maneuvers. $1.1g$ and $1.3g$ turns were his data set. ASYM contains all the 2022 maneuvers and a subset of accelerated stalls from 2018. This data set is used for the identification and validation of the proposed stall model. ASYM is randomly split into a training set of 24 maneuvers and a validation set of 6 maneuvers (an 80-20 split). When presenting flight data or identification results, this paper will refer to the maneuver IDs in the two right-most columns of Table 2. An overview of the resulting maneuver characteristics can be found in Fig. 3. The approximate distributions of the bank angle and sideslip angle are visualized in Fig. 3a and Fig. 3b, respectively. Strong lateral excursions are found for all maneuvers. Also, note that set 14 is the only stall maneuver that was initiated in a left turn. Finally, Fig. 3b shows that sets 55-30 generally contain larger sideslip angles, but the difficulty to maintain the reference angle is evident.

All recorded data are pre-processed by applying a zero-phase low-pass Butterworth filter of order 4, as this choice provided satisfactory results in previous stall modeling efforts [14, 15]. This step is taken to combat the disturbances due to stall buffet vibrations and amplified noise from numerical differentiation. The latter disturbance source is relevant for the rotational acceleration signals (e.g. $\dot{p}$) and the rates of the airflow angles $\dot{\alpha}$, $\dot{\beta}$.

The final pre-processing step is flight path reconstruction using an Unscented Kalman Filter (UKF), to provide an optimal estimate of the aircraft state during the maneuvers. Van Horssen et al. [14] first applied this filter and demonstrated its effectiveness for the purpose of stall modeling. Van Ingen et al. [15] adapted the observation model for the airflow angle measurements from the air data boom. Please consult these references for further details on flight path reconstruction.

**Table 2 The stall maneuvers contained in the ASYM and VAN INGEN data sets.**

| Data set | FL | $n_z$ [-] | $\beta_{\text{ref}}$ [°] | Input ($\delta_a$ \| $\delta_e$) | Reps | Training Sets | Validation Sets |
|---|---|---|---|---|---|---|---|
| **ASYM** | 150-200 | 1.1g | 0 | QR \| QR | 12 | 1-4, 8-11, 13, 18, 19 | 12 |
| | 150-200 | 1.1g | 0 | 3211 \| QR | 5 | 20, 21, 24 | 22, 23 |
| | 150-200 | 1.1g | 5 | QR \| QR | 1 | | 25 |
| | 150-200 | 1.1g | 5 | 3211 \| QR | 5 | 26-30 | |
| | 150-200 | 1.3g | 0 | QR \| QR | 7 | 5, 6, 14, 15, 17 | 7, 16 |
| **VAN INGEN** | 80-110 | 1.0g | 0 | QR \| QR | 2 | 1, 2 | |
| | 110-150 | 1.0g | 0 | QR \| QR | 4 | 3,4, 6 | 5 |
| | 150-200 | 1.0g | 0 | QR \| QR | 11 | 8-11, 13-15, 33, 34 | 7, 12, 16 |
| | 150-200 | 1.1g | 0 | QR \| QR | 10 | 17-19, 24, 26-28 | 23, 25 |
| | 150-200 | 1.3g | 0 | QR \| QR | 7 | 20, 21, 29-32 | 22 |

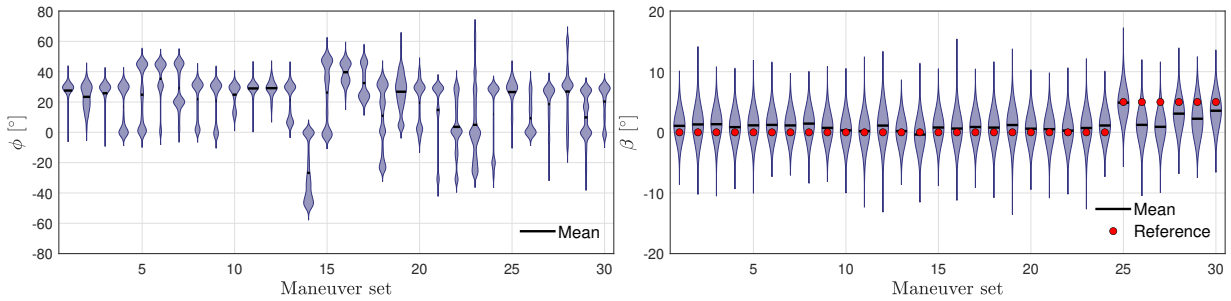


**(a) Bank angle.** **(b) Sideslip angle.**

**Fig. 3 Violin plots presenting the approximate distribution of the states that are expected to be relevant for inducing asymmetric stall effects.**

### C. Aerodynamic Coefficients

The aerodynamic force and moment coefficients cannot be measured directly in flight. Instead, the following dynamic relationships are employed to compute these quantities from the available measurements [15, 16, 19]. The force coefficients in the aircraft body frame are computed directly from the linear acceleration measurements $a_x$, $a_y$, and $a_z$. The aircraft dimensions and inertial parameters can be found in Table 1.

$$C_X \equiv -C_A = \frac{(ma_x - X_T)}{\bar{q}S} \qquad C_Y = \frac{ma_y}{\bar{q}S} \qquad C_Z = -C_N = \frac{(ma_z - Z_T)}{\bar{q}S} \tag{1}$$

where $m$ is the aircraft mass, and $\bar{q}$ is the dynamic pressure. $X_T$ and $Z_T$ are the contributions of the thrust along the specified axes, where $Z_T$ is set equal to 0, meaning the thrust contribution along the $z_b$-axis is neglected. The model will be expressed in the aerodynamic frame, which is rotated by $\alpha$ and $\beta$ with respect to the body frame.

$$C_D = -C_X \cos\alpha \cos\beta + C_Y \sin\beta - C_Z \sin\alpha \cos\beta \qquad C_L = -C_Z \cos\alpha + C_X \sin\alpha \tag{2}$$

The moment coefficients are computed using the rotational accelerations $\dot{p}, \dot{q}, \dot{r}$ and the known dimensions and inertial parameters. The rotational accelerations are not measured directly, but they are computed through numerical differentiation of the roll rate $p$, pitch rate $q$, and yaw rate $r$. The resulting signals are subsequently low-pass filtered to reduce any amplified noise originating from the numerical method.

$$C_l = \frac{I_{xx}}{\bar{q}Sb}\left[\dot{p} - \frac{I_{xz}}{I_{xx}}(pq + \dot{r}) + \frac{(I_{zz} - I_{yy})}{I_{xx}}qr\right] \tag{3}$$

$$C_m = \frac{I_{yy}}{\bar{q}S\bar{c}}\left[\dot{q} + \frac{(I_{xx} - I_{zz})}{I_{yy}}pr + \frac{I_{xz}}{I_{yy}}\left(p^2 - r^2\right)\right] + \frac{1}{\bar{q}S\bar{c}}X_T(z_e - z_{cg}) \tag{4}$$

$$C_n = \frac{I_{zz}}{\bar{q}Sb}\left[\dot{r} - \frac{I_{xz}}{I_{zz}}(\dot{p} - qr) + \frac{\left(I_{yy} - I_{xx}\right)}{I_{zz}}pq\right] \tag{5}$$

Note the thrust-based correction in the pitch moment relationship, where $z_e$ and $z_{cg}$ are the vertical locations of the engine and the center of gravity, respectively. In subsequent sections, the resulting set of aerodynamic force and moment coefficients will be referred to as measurements, while acknowledging that they are, in fact, reconstructed.

## III. Methodology

### A. Kirchhoff's Flow Separation Model

The description of nonlinear behavior in the proposed stall model is based on Kirchhoff's theory of flow separation. This model describes the lift coefficient of an airfoil $C_L$ at high angle of attack $\alpha$:

$$C_L = C_{L_\alpha}\left(\frac{1 + \sqrt{X}}{2}\right)^2 \alpha \tag{6}$$

where $C_{L_\alpha}$ is the airfoil's lift slope. The flow separation point $X$ is a non-dimensional coordinate that represents the position of the separation point on the upper surface of the airfoil. It ranges from 0 to 1, where $X = 1$ indicates fully attached flow and $X = 0$ corresponds to fully separated flow [8].

Prior stall modeling efforts have demonstrated that the lift generated by a wing surface at high angle of attack is dependent on $\alpha$, $\dot{\alpha}$ and the motion prehistory of the aircraft [8, 9]. This time-varying response of aerodynamic forces as a result of modifying flow conditions is referred to as unsteady aerodynamics. A distinction is made between the steady flow separation point $X_0$ and the unsteady flow separation point $X$. The steady variant is approximated by:

$$X_0(\alpha) = \frac{1}{2}\left\{1 - \tanh\left(a_1\left(\alpha - \alpha^*\right)\right)\right\} \tag{7}$$

The practicality of this approximation was demonstrated in its suitability for identification purposes, as it requires the determination of only two parameters ($a_1$, $\alpha^*$), and the tanh function is fully continuous [9]. $a_1$ is a shaping parameter that describes the abruptness of the stall. $\alpha^*$ schedules the flow separation in terms of $\alpha$, and is generally referred to as the stall angle of attack. It represents the angle of attack at which the flow separation point reaches 50% of the chord, in steady conditions. Both parameters are mainly determined by airfoil and wing configuration [20].

However, $X_0$ does not describe flow separation accurately in unsteady flow conditions ($\dot{\alpha} \neq 0$). The description of unsteady aerodynamic processes is summarized into two groups: quasi-steady effects and transient effects. Quasi-steady effects, such as circulation and boundary-layer effects, tend to cause hysteresis from attached flow to flow separation and vice versa, by an amount approximately proportional to $\dot{\alpha}$. The parameter $\tau_2$ is introduced to model these effects [9]:

$$X(\alpha, \dot{\alpha}) = X_0(\alpha - \tau_2\dot{\alpha}) \tag{8}$$

where $\tau_2$ depends mostly on airfoil shape and wing configuration [9].

The transient effects are modeled by introducing a first-order Ordinary Differential Equation (ODE) with parameter $\tau_1$, reflecting that any disturbance of separated flow is followed by a relaxation back to the steady-state [21]. $\tau_1$ is primarily dependent on the free-stream flow characteristics and the trailing edge flow characteristics of the wing-body, and it is independent of the airfoil and wing configuration [20].

$$\tau_1\frac{dX}{dt} + X = X_0(\alpha - \tau_2\dot{\alpha}) \tag{9}$$

Substitution of Eq. (7) yields the single ODE:

$$\tau_1\frac{dX}{dt} + X = \frac{1}{2}\left\{1 - \tanh\left(a_1\left(\alpha - \tau_2\dot{\alpha} - \alpha^*\right)\right)\right\} \tag{10}$$

Van Ingen et al. [15] referred to the total set of parameters $\{\tau_1, \tau_2, a_1, \alpha^*\}$ as the "$X$-parameters", a term that is also adopted in this paper.

**B. Asymmetric Kirchhoff Model**

A significant portion of stall modeling efforts that applied Kirchhoff's model only yielded satisfactory results for the longitudinal model. In order to include stall effects in the lateral-directional model, Singh and Jategaonkar [22] proposed to add differential lift and drag terms to the roll moment and yaw moment model, respectively:

$$\Delta\hat{C}_l = \left[(C_L)_L - (C_L)_R\right] \frac{y_w}{b} \tag{11}$$

$$\Delta\hat{C}_n = \left[(C_D)_L - (C_D)_R\right] \frac{y_w}{b} \tag{12}$$

where $\Delta\hat{C}_l$ and $\Delta\hat{C}_n$ are the additions to the roll and yaw moment model structure, and subscripts $L$ and $R$ denote the left and right wing, respectively. $b$ denotes the wing span, and $y_w$ is the moment arm of the wing, which Singh and Jategaonkar [22] assumed equal to $\frac{b}{2}$.

Lutze et al. [13] considered a similar differential of lift surface coefficients for the multi-axis unsteady modelling of an F-18 aircraft. For instance, the roll moment model structure applied contributions from four separate lift surfaces:

$$\hat{C}_l = \left[(C_{N_1})_L - (C_{N_1})_R\right] \frac{y_w}{b} + \left[(C_{N_2})_L - (C_{N_2})_R\right] \frac{y_t}{b} + C_{Y_t} \frac{z_t}{b} \tag{13}$$

where $(C_{N_1})_L$ and $(C_{N_1})_R$ are the normal force contributions of the individual wing surfaces, and $(C_{N_2})_L$ and $(C_{N_2})_R$ are the normal force contributions of the individual horizontal tail surfaces. Finally, $C_{Y_t}$ denotes the lateral force generated by the vertical tail and $y_t$ and $z_t$ are the moment arms for the horizontal tail and vertical tail, respectively. In this work, all described force coefficients were modeled as quadratic polynomials of the flow separation variable of the respective surface.

*1. Asymmetric Stall Description using the Roll Moment*

The aerodynamic coefficient that is most important for describing asymmetric stall characteristics is the roll moment coefficient, as it is directly dependent on lift differentials between lift surfaces. In this research, only the differential between the main wing surfaces is considered. The individual surface lift coefficients of Eq. (11) are modeled by Kirchhoff's model.

$$\Delta\hat{C}_l = \left[(C_{L_\alpha})_L \left(\frac{1+\sqrt{X_L}}{2}\right)^2 \alpha_L - (C_{L_\alpha})_R \left(\frac{1+\sqrt{X_R}}{2}\right)^2 \alpha_R\right] \frac{y_w}{b} \tag{14}$$

where $\alpha_L$ and $\alpha_R$ denote the local angle of attack at a distance $y_w$ on the left and right wing surface, respectively.

Symmetric wings would imply equal airfoil properties, resulting in the simplification $C_{l_{\Delta K_\alpha}} = (C_{L_\alpha})_L = (C_{L_\alpha})_R$. For simplicity, the notation $\Delta K_\alpha$ is introduced:

$$\Delta\hat{C}_l = C_{l_{\Delta K_\alpha}} \Delta K_\alpha \frac{y_w}{b} \quad \text{with} \quad \Delta K_\alpha = \left(\frac{1+\sqrt{X_L}}{2}\right)^2 \alpha_L - \left(\frac{1+\sqrt{X_R}}{2}\right)^2 \alpha_R \tag{15}$$

Note that Kirchhoff's model was developed for airfoils. In Eq. 15, it is assumed that it can provide an adequate description of the difference in lift between entire wing surfaces. However, the lift of an aircraft is generally modeled with more than a single model term. Considering the fact that Kirchhoff's model may not be suitable for a single wing surface, a simpler alternative description of asymmetric stall is proposed:

$$\Delta\hat{C}_l = C_{l_{\Delta X}} \Delta X \frac{y_w}{b} \quad \text{with} \quad \Delta X = (X_L - X_R) \tag{16}$$

This is a simplification of Lutze et al.'s description in Eq (13): the dependence of the left wing surface lift on $X_L$, is approximated as a first-order polynomial, where the bias is included in the general bias term of the model ($C_{l_0}$). The same holds for the right wing surface. The symmetry property of the aircraft is again taken into account, to obtain a single parameter $C_{l_{\Delta X}}$. The flow separation variables are each governed by their own ODEs:

$$(\tau_1)_{L,R} \frac{dX_{L,R}}{dt} + X_{L,R} = \frac{1}{2}\left\{1 - \tanh\left(a_1\left(\alpha_{L,R} - \tau_2 \dot{\alpha}_{L,R} - \alpha^*\right)\right)\right\} \tag{17}$$

Finally, for the longitudinal models, the symmetric flow separation variable $X$ is computed by taking the mean of $X_L$ and $X_R$ at every data point:

$$X = \frac{X_L + X_R}{2} \tag{18}$$

*2. Local Angle of Attack Computation*

The local angle of attack at an arbitrary point $P$ is computed through a kinematic relationship that describes the local airflow velocity, whereby the aircraft is assumed to be a rigid body [23]:

$$\alpha_P = \text{atan}\left(\frac{w_P}{u_P}\right) = \text{atan}\left(\frac{w - q\Delta x_P + p\Delta y_P}{u - r\Delta y_P + q\Delta z_P}\right) \tag{19}$$

where $\Delta \boldsymbol{X_p} = [\Delta x_P \ \Delta y_P \ \Delta z_P]^\top$ are the distances from the aircraft center of gravity (CG) to the point $P$. For the left and right wings only the lateral offset is relevant: $\Delta \boldsymbol{X_{L,R}} = [0, \pm y_w, 0]^\top$. Since $y_w$ is to describe a moment arm of the lift vector, ideally this value is equal to the distance to the center of lift of a single wing surface, measured from the fuselage center line. As an approximation, it is set equal to the lateral location of the Mean Aerodynamic Chord (MAC). Fig. 4 presents a reconstructed response of the local angles of attack to a 3-2-1-1 aileron input, during an accelerated stall maneuver. Note that the angle of attack at the CG is the mean of the local variants.

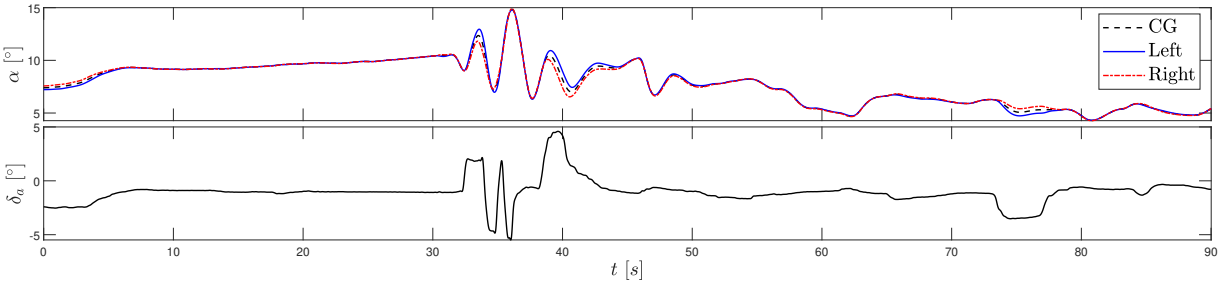


**Fig. 4 The response of the local and general angle of attack to a 3-2-1-1 aileron input ($t \approx 30$ s to $t \approx 40$ s), during an accelerated stall maneuver (ASYM set 21).**

### C. Identification Problem and Approach

The main objective of the identification procedure is the creation of a 6-DOF aerodynamic model of the aerodynamic force and moment coefficients. As such, the downstream identification task is the estimation of the parameter vectors of the coefficients of lift ($C_L$), drag ($C_D$), lateral force ($C_Y$), roll moment ($C_l$), pitch moment ($C_m$), and yaw moment ($C_n$):

$$\hat{\theta}_{C_L}, \hat{\theta}_{C_D}, \hat{\theta}_{C_Y}, \hat{\theta}_{C_l}, \hat{\theta}_{C_m}, \hat{\theta}_{C_n} \tag{20}$$

where each parameter vector is estimated separately and the parameters to be estimated are selected by distinct model structure selection procedures. Transformations of $X_L$ and $X_R$ must be included in the model structures in order to describe asymmetric flow separation. No direct measurement of these variables is available in flight; they must be estimated from flight data. The $X$-parameters provide a convenient description of the flow separation variables. Once these parameters are known or estimated, $X_L$ and $X_R$ can be determined by solving their respective ODEs, i.e. Eq. (17). Hence, the second set of parameters to estimate consists of the $X$-parameters:

$$\hat{\theta}_X = [\ \tau_1 \quad \tau_2 \quad a_1 \quad \alpha^* \ ]^\top \tag{21}$$

The parameter estimation approach is split into two parts: the nonlinear $X$-parameter estimation and the linear $C_i$-parameter estimation. A similar split was made for the identification of the baseline stall model [15]. This approach is applied to take advantage of mostly linear $\hat{C}_i$ model structures. By regarding the flow separation variables as fixed regressor variables, the linearity is retained, enabling the use of well-known, reliable, and efficient linear regression methods [19]. Moreover, the model structure selection step is simplified, as iterations of candidate models can be evaluated in quick succession. The resulting overall identification approach consists of four interdependent stages, as visualized by Fig. 5.

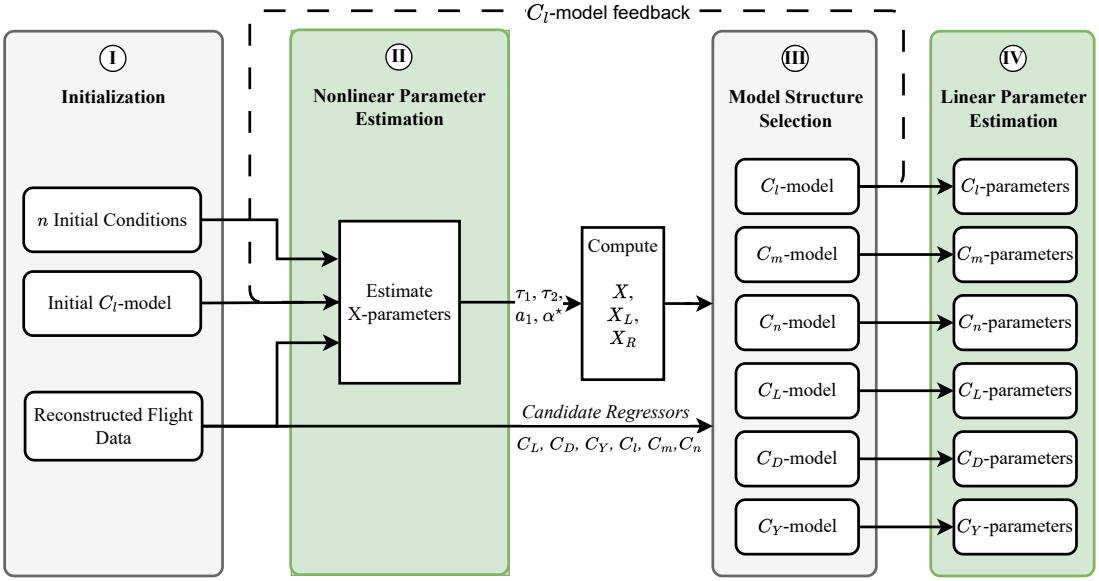


**Fig. 5 A flowchart describing the proposed identification approach.**

### D. Step I: Initial Roll Moment Model Selection

To perform the nonlinear optimization, an initial guess of a suitable roll moment model structure is required. The conventional linearized model structure is suitable outside the stall region [19]:

$$\hat{C}_l(x,\theta)_{\text{lin}} = C_{l_0} + C_{l_\beta}\beta + C_{l_p}p + C_{l_r}r + C_{l_{\delta_a}}\delta_a + C_{l_{\delta_r}}\delta_r \tag{22}$$

In order to identify asymmetric flow separation characteristics in Step II of Fig. 5, $X_L$ and $X_R$ must be included in the initial roll moment model. Two mathematical formulations of asymmetric stall were introduced in section III.B. The effectiveness of the parameter identification task is evaluated for both formulations, to determine whether a modification of Kirchhoff's model is required or a simpler approximation is sufficient. Eq. (15) and Eq. (16) are appended to the conventional roll moment model to obtain the Model A-I and Model B-I, respectively. Here, "I" denotes the first iteration of the roll moment model structure selection process.

- Model A-I:

$$\hat{C}_l(x,\theta)_0 = \hat{C}_l(x,\theta)_{\text{lin}} + C_{\Delta K_\alpha}\Delta K_\alpha \frac{y_w}{b} \quad \text{with} \quad \Delta K_\alpha = \left(\frac{1+\sqrt{X_L}}{2}\right)^2 \alpha_L - \left(\frac{1+\sqrt{X_R}}{2}\right)^2 \alpha_R \tag{23}$$

- Model B-I:

$$\hat{C}_l(x,\theta)_0 = \hat{C}_l(x,\theta)_{\text{lin}} + C_{l_{\Delta X}}\Delta X \frac{y_w}{b} \quad \text{with} \quad \Delta X = (X_L - X_R) \tag{24}$$

Note that the simplicity of the additional term of model B comes form the exclusion of local angles of attack: once the $X$-parameters are estimated, these local computations are no longer required for evaluating the model output.

### E. Step II: Nonlinear Parameter Estimation

A nonlinear optimization method is employed for the identification of the flow separation parameters. The nonlinearity of the problem originates from the ODEs of Eq. (17). The objective function is the mean squared error (MSE) of the roll moment model output $\hat{C}_l(\theta,x)$ with respect to the measurement $C_l$.

$$\hat{\theta} = \arg\min_{\theta} J(\theta,x) \quad \text{with} \quad J(\theta,x) = \frac{1}{N}\left(C_l - \hat{C}_l(\theta,x)\right)^\top \left(C_l - \hat{C}_l(\theta,x)\right) \tag{25}$$

where $C_l, \hat{C}_l \in \mathbb{R}^{N\times 1}$ and $N$ denotes the number of data points in a training set.

As mentioned in Section III.A, the $X$-parameters are mostly dependent on airfoil and wing configuration. Only $\tau_1$ is determined by the free-stream velocity. Both conditions are assumed to be equal between the wing surfaces. Hence, a single set of $X$-parameters is to be estimated:

$$(\theta_X)_L = (\theta_X)_R = \theta_X = \begin{bmatrix} \tau_1 & \tau_2 & a_1 & \alpha^* \end{bmatrix}^\top \tag{26}$$

The parameter vector associated to this optimization is the result of appending the $C_l$-parameters to the $X$-parameters. Note that these $C_l$-parameter estimates are not directly used for the final roll moment model. These additional estimates provide a method of verification of the optimization, as they should converge to similar values. For the first iteration, the introduced initial roll moment model structures yield the parameter vectors of the associated optimization problems:

- Model A-I:

$$(\theta_{nl})_A = \begin{bmatrix} \tau_1 & \tau_2 & a_1 & \alpha^* & C_{l_0} & C_{l_\beta} & C_{l_p} & C_{l_r} & C_{l_{\delta_a}} & C_{l_{\delta_r}} & C_{l_{\Delta K_\alpha}} \end{bmatrix}^\top \tag{27}$$

- Model B-I:

$$(\theta_{nl})_B = \begin{bmatrix} \tau_1 & \tau_2 & a_1 & \alpha^* & C_{l_0} & C_{l_\beta} & C_{l_p} & C_{l_r} & C_{l_{\delta_a}} & C_{l_{\delta_r}} & C_{l_{\Delta X}} \end{bmatrix}^\top \tag{28}$$

Lower and upper bounds are enforced on the parameters, to shrink the solution space. The optimization is performed by an Interior Point algorithm implementation, using the `fmincon` function from MATLAB's optimization toolbox. This implementation cannot guarantee convergence to a global optimum. In fact, in the best case a local optimum can be obtained. If the objective function in the optimization problem and the feasible region are both convex, then any local solution of the problem is in fact a global solution [24]. Since the feasible region is solely defined by lower and upper bounds on the parameters, it is convex. However, proving convexity of the objective function is complex and outside of the scope of this paper. Instead, the objective function is computed for 500 randomly generated initial conditions. The best 300 of these conditions, as ranked by the initial objective function value, are used for the optimization. The runs corresponding to an objective function value within 2% of the lowest result are averaged to obtain the final parameter estimates. This method is employed to increase the confidence of converging to a global optimum, and it is repeated for every maneuver in the training set.

The interior point algorithm requires the computation of the cost function gradient with respect to the parameters. Finite difference methods can be especially prone to numerical errors when they are applied to the solution of a differential equation [25]. Hence, the gradient is specified semi-analytically, as described in Appendix VI.B [15].

### F. Step III: Model Structure Selection

The general objective of the model structure selection procedure (Step III in Fig. 5) is to generate a compact model that retains adequate complexity to capture the nonlinearities associated with aircraft stall [26]. Minimizing the number of model terms enhances parameter identifiability, leading to improved accuracy in parameter estimates and prediction performance. The interdependence of the model structure selection tasks is further detailed in Fig. 6. The roll moment model structure $\hat{C}_l(x, \theta)$ must be selected first, as any changes in this model could result in different $X$-parameter estimates. Once these parameter estimates are fixed, the remaining model structures can be selected. Finally, it is chosen to keep the longitudinal model structures equal to those of the previous stall model. These structures have been shown to capture the nonlinearities of aircraft stall adequately [15]. The newly estimated $X$-parameters are used for the evaluation of this model, providing the opportunity to evaluate the proposed method for the application of longitudinal modeling.

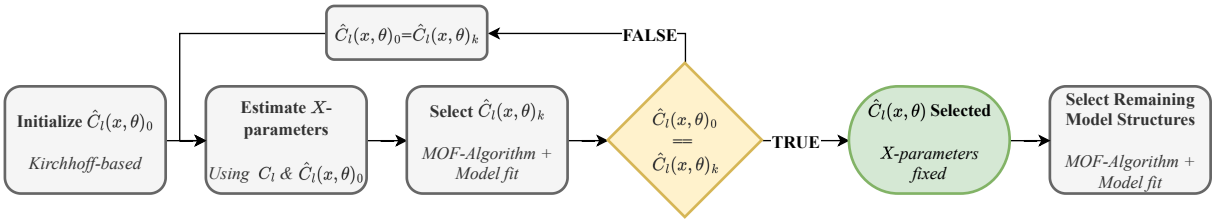


**Fig. 6 The process of model structure selection, starting from the initial roll moment model.**

*1. Multivariate Orthogonal Functions Algorithm*

Model structure selection and parameter estimation are coupled procedures. While selecting a model structure is a prerequisite for parameter estimation, evaluating the adequacy of a postulated model requires parameter estimates. This circular dependence makes the problem difficult to solve objectively [26]. A possible solution is the concept of stepwise regression, where statistical hypothesis testing is employed to select model terms from a pool of proposed terms [27].

An additional challenge lies in the potential correlation between independent variables. An intuitive example is the correlation between the rate of change of angle of attack $\dot{\alpha}$ and the pitch rate $q$. Assuming a model structure including both terms is adequate, the regressors of the resulting least-squares problem likely have high correlations, rendering the parameter estimation problem ill-conditioned, resulting in inaccurate parameter estimates [26].

To tackle these challenges, Morelli [26] applied a Multivariate Orthogonal Functions (MOF) modeling algorithm, with the purpose of global aerodynamic modeling. Subsequent work has proven the effectiveness of this technique for the application of aircraft stall modeling [15, 16]. Hence, this selection method is employed in this paper.

The initial inputs to the algorithm are the pool of independent variables. Based on the base regressors and some maximum term order, a set of candidate model terms is generated. As a first step, a bias term is included:

$$\mathbf{a_1} = \mathbf{p_1} = \mathbf{1} \tag{29}$$

where $\mathbf{a_1}$ is the original bias variable, which is in this case equal to the orthogonalized bias variable $\mathbf{p_1}$. A Gram-Schmidt orthogonalization procedure is performed to all remaining candidate terms with respect to the currently selected terms, resulting in the orthogonalized regression variables $\mathbf{p_j}$, which are linear combinations of the original regression variables $\mathbf{a_j}$.

$$\mathbf{p}_j = \mathbf{a}_j - \sum_{k=1}^{j-1} \gamma_{k,j}\mathbf{p}_k, \quad j = 2, 3, \ldots, n, \quad \text{where} \quad \gamma_{k,j} = \frac{\mathbf{p}_k^\top \mathbf{a}_j}{\mathbf{p}_k^\top \mathbf{p}_k} \tag{30}$$

The Predicted Square Error (PSE) is a combination of the fit error (MSE) and a linear complexity penalty term. This metric is used for the evaluation of the candidate model terms.

$$\text{PSE} = \frac{(\mathbf{y} - \hat{\mathbf{y}})^\top (\mathbf{y} - \hat{\mathbf{y}})}{N} + \sigma_y^2 \frac{n}{N} \tag{31}$$

where $\hat{\mathbf{y}}$ denotes the model output resulting from the currently selected orthogonal regressors and $\mathbf{y}$ is the measurement vector $C_i$. $N$ and $n$ indicate the number of data points and the number of currently selected model terms, respectively. $\sigma_Y^2$ acts as a scaling parameter. To be effective, a scaling parameter should be independent of the selected model structure. Therefore, it is set equal to the variance of the signal to be modeled $\sigma_{C_i}^2$. Since $\mathbf{p}_j$ is an orthogonal set, the change in PSE resulting from the addition of candidate $j$ to the model structure can be determined explicitly:

$$\Delta\text{PSE}_j = -\frac{\left(\mathbf{p}_j^\top \mathbf{y}\right)^2}{\mathbf{p}_j^\top \mathbf{p}_j} + \sigma_y^2 \frac{1}{N} \tag{32}$$

The candidate term that leads to the greatest reduction in PSE is added to the model. Orthogonalization, PSE computation, and term selection are repeated until $\Delta\text{PSE}_j \leq 0 \; \forall \; j \in \{1, 2, ..., n\}$, indicating that the reduction in MSE is outweighed by the added complexity of any term.

Once the termination condition is met, a matrix $P = [\ \mathbf{p}_1 \quad \mathbf{p}_2 \quad \ldots \quad \mathbf{p}_n\ ]$ is constructed. This is a regression matrix for obtaining the maximum-likelihood parameters $\hat{\phi}$ associated with the orthogonalized regressors. A standard Ordinary Least Squares (OLS) procedure is applied to obtain $\hat{\phi}$. Using a matrix $\Gamma$, a collection of $\gamma_{k,j}$ variables, the OLS result $\hat{\mathbf{y}} = P\hat{\phi}$ is transformed back to the original regression form $\hat{\mathbf{y}} = A\hat{\theta}$:

$$A = P\Gamma \quad \text{with} \quad \Gamma = \begin{bmatrix} 1 & \gamma_{1,2} & \gamma_{1,3} & \cdots & \gamma_{1,n} \\ 0 & 1 & \gamma_{2,3} & \cdots & \gamma_{2,n} \\ 0 & 0 & 1 & \cdots & \gamma_{3,n} \\ \vdots & \vdots & \vdots & \ddots & \vdots \\ 0 & 0 & 0 & \cdots & 1 \end{bmatrix} \tag{33}$$

Finally, the optimal original parameter vector $\hat{\theta}$ is obtained through substitution:

$$\hat{\mathbf{y}} = P\hat{\phi} = PI\hat{\phi} = P\left(\Gamma\Gamma^{-1}\right)\hat{\phi} = A\Gamma^{-1}\hat{\phi}, \quad \longleftrightarrow \quad \hat{\theta} = \Gamma^{-1}\hat{\phi} \tag{34}$$

When the optimal parameter vector has been obtained, the contribution of the term to the model output is tested. This test is carried out by comparing the Root Mean Square (RMS) of the model output $\hat{\mathbf{y}}$ with the RMS of the unchanged model output.

$$\text{RMS} = \frac{1}{N}\sqrt{\hat{\mathbf{y}}^\top\hat{\mathbf{y}}} \tag{35}$$

If the reduction in RMS (Root Mean Square) falls below a threshold of 0.5%, the corresponding term is eliminated from consideration due to its negligible influence. This operation marks the completion of the model structure selection algorithm for a particular dataset. The algorithm is repeated for all maneuver sets. Generalization is achieved by tallying the number of instances a regressor is selected. If the term is selected in at least 50% of the data sets, it is strongly considered for the final model. Although the outcomes of this algorithm offer valuable insights into the assessment of model term effectiveness, additional analyses may be necessary to establish a robust model. These analyses could involve comparisons of model fit, estimations of parameter correlations, consultation of literature, and other engineering judgement.

*2. Candidate Regression Variables*

The reconstructed flight data amounts to a pool of candidate regressors, to be used in the model structure selection. The performance of the described selection algorithm relies completely on the combined explanatory value of this candidate pool.

The pool of candidate regressors considered in this paper can be found in Table 3. Several different categories of regressors are identified. A bias term is included in every model. To employ additional a priori knowledge, a linearized quasi-steady analytical aircraft model is taken as a reference [19], where a distinction is made between regressors that describe symmetric and asymmetric motion. Note that lateral-directional models could in fact benefit from the addition of a regressor from the symmetric category, and vice versa. The signals in the "measured" category are directly available from the reconstructed flight data, and they form the most commonly appearing regressors in literature. The inclusion of $C_T$ is based on errors in the aircraft's engine model. This is further detailed by van Ingen et al. [15] and outside the scope of this work. To include unsteady effects, time-derivatives of the flow angles are included. Finally, a set of transformations of the flow separation variables is included. A preliminary collinearity analysis of the entire candidate pool was performed to investigate the similarity between the candidates. The results of this analysis can be found in Appendix VI.A. Including highly similar regressors could result in ambiguous model selection results. Finally, for the remainder of this paper, any mentions of rotational rates are referring to the dimensionless rates:

$$p = \frac{\tilde{p}b}{2V} \quad (36) \qquad q = \frac{\tilde{q}c}{V} \quad (37) \qquad r = \frac{\tilde{r}b}{2V} \quad (38) \qquad \dot{\alpha} = \frac{\tilde{\dot{\alpha}}c}{V} \quad (39) \qquad \dot{\beta} = \frac{\tilde{\dot{\beta}}b}{2V} \quad (40)$$

**Table 3 The candidate regression variables categorized by model type.**

| Regressor Type | Symmetric | Asymmetric |
|---|---|---|
| **Bias** | **1** | **1** |
| **Measured** | $\alpha$, $q$, $C_T$, $M$, $\delta_e$ | $\beta$, $p$, $r$, $\delta_a$, $\delta_r$ |
| **Time-derivative** | $\dot{\alpha}$ | $\dot{\beta}$ |
| **Flow Separation** | $X$, $(1-X)$ | $\Delta X\frac{y_w}{b}$, $\Delta K_\alpha\frac{y_w}{b}$ |

## G. Step IV: Linear Parameter Estimation

Given a set of six linear-in-the-parameters model structures, Step IV concerns the identification of the $C_i$-parameters. The selected model structures are linear polynomials:

$$\hat{C}_i = \theta_{C_{i_1}}\boldsymbol{a}_1 + \theta_{C_{i_2}}\boldsymbol{a}_2 + \ldots + \theta_{C_{i_n}}\boldsymbol{a}_n, \quad \text{for} \quad i \in \{L, D, Y, l, m, n\} \tag{41}$$

where $\hat{C}_i$ is the model output of force or moment $i$, $\boldsymbol{a}_j$ are the regressor vectors and $\theta_{C_{i_j}}$ are the parameters from the vector $\theta_{C_i}$. Using the matrix notation the equation reduces to the regression form:

$$\hat{C}_i = A\theta_{C_i}, \quad \text{with} \quad A = [\boldsymbol{a}_1\ \boldsymbol{a}_2\ \ldots\ \boldsymbol{a}_n] \tag{42}$$

The OLS solution is applied to minimize the model error $\epsilon = C_i - \hat{C}_i$, where $C_i$ denotes the measurement vector. This results in the closed-form solution for all parameter vectors:

$$\hat{\theta}_{C_i} = (A^\top A)^{-1} A^\top C_i, \quad \text{for} \quad i \in \{L, D, Y, l, m, n\} \tag{43}$$

# IV. Results

The described methodology is applied to the flight data to obtain the stall model. Due to the interdependencies in the approach of Fig 5, the order of presentation of the results is quite particular. The initial roll moment model structure selection (Step I) was detailed in Section III.D. Converging to a final roll moment model structure is a prerequisite for estimating the final set of $X$-parameters. Therefore, this process is described first (Step IIIa). Subsequently, the final nonlinear optimization results are detailed (Step II) and the remaining model structures are selected (Step IIIb). When the $X$-parameters and all model structures are fixed, the results of the linear regression step are shown (Step IV), presenting the complete stall model. Finally, the model is validated using a subset of the flight test data set.

## A. Step IIIa: $C_l$-Model

The most important model structure is that of the roll moment coefficient. The two initial models were introduced as Model A-I and Model B-I, a couple of conventional linear model structures, each appended with a term describing asymmetric flow separation (Eq. (23) and Eq. (24), respectively). The intermediate and final nonlinear optimizations of both models result in the sets of parameter estimates presented in Table 4, and will be discussed throughout this section.

**Table 4 $X$-parameter estimates of the intermediate roll moment models, for the $C_l$-model structure selection.**

| | **Optimization** | **Model A-I** | | **Model B-I** | | **Model A-II** | | **Final Model A** | | **Final Model B** | |
|---|---|---|---|---|---|---|---|---|---|---|---|
| $\theta$ | **Bounds** | $\hat{\theta}$ | $\sigma_{\hat{\theta}}$ | $\hat{\theta}$ | $\sigma_{\hat{\theta}}$ | $\hat{\theta}$ | $\sigma_{\hat{\theta}}$ | $\hat{\theta}$ | $\sigma_{\hat{\theta}}$ | $\hat{\theta}$ | $\sigma_{\hat{\theta}}$ |
| $\tau_1$ [s] | [0.001, 0.50] | 0.0950 | 0.0681 | 0.1166 | 0.0598 | 0.1015 | 0.0475 | 0.0923 | 0.0459 | 0.0971 | 0.0282 |
| $\tau_2$ [s] | [0.000, 0.80] | 0.6047 | 0.1497 | 0.5386 | 0.1486 | 0.5830 | 0.1473 | 0.4487 | 0.1409 | 0.5526 | 0.1636 |
| $a_1$ [-] | [15.00, 40.0] | 19.404 | 3.1643 | 17.269 | 2.9987 | 19.054 | 4.2976 | 18.203 | 1.4527 | 16.865 | 1.1672 |
| $\alpha^*$ [rad] | [0.100, 0.35] | 0.1494 | 0.0406 | 0.1744 | 0.0363 | 0.1760 | 0.0296 | 0.1694 | 0.0253 | 0.1730 | 0.0194 |

*1. Model A*

To initiate the process, the model structure selection algorithm is run using the $X$-parameters from Model A-I, yielding the selected regressors of Fig. 7a. The candidate regressors on the vertical axis are selected in the number of maneuver sets projected on the horizontal axis. A grey bar indicates that the corresponding regressor is frozen into the model, either due to selection in a previous iteration, or it concerns a bias term.

Two noteworthy observations arise. Firstly, $\Delta X \frac{y_w}{b}$ is evaluated to be more useful at describing the roll moment than $\Delta K_\alpha \frac{y_w}{b}$. This is a surprising result, as the $X$-parameters were optimized using Model A, which included only the latter regressor. Secondly, the selection of $p$ just barely reaches the 50% threshold, while the baseline stall model structure selection resulted in $p$ having the second-largest contribution to the roll moment model [15]. Moreover the associated parameter $C_{l_p}$ is the roll damping, an important parameter describing the lateral dynamic stability of the aircraft [28].

A second iteration of the algorithm is performed to obtain the optimal structure. All the terms that satisfy the 50% threshold are frozen into the model. In the second iteration, $r$ still does not satisfy the threshold. However, including this regressor resulted in an improved model fit, after linear regression (-2.5% validation MSE). Also, as described in Appendix VI.A, this signal is not strongly correlated to other candidates, making the inclusion unlikely to cause estimation issues. Hence, it is chosen to include it in the model structure. The second iteration of Model A is selected:

$$\text{Model A-II:} \quad \hat{C}_l(x, \theta) = C_{l_0} + C_{l_\beta}\beta + C_{l_p} p + C_{l_r} r + C_{l_{\delta_a}} \delta_a + C_{L_\alpha} \Delta K_\alpha \frac{y_w}{b} + C_{L_X} \Delta X \frac{y_w}{b} \tag{44}$$

To confirm that the model structure has converged, another $X$-parameter estimation step is required, using Model A-II. The parameter estimates in Table 4 indicate that including $\Delta X \frac{y_w}{b}$ causes an increase of 18% in the $\alpha^*$ estimate. The remaining parameter estimates are relatively close to the estimates of Model A-I.

Fig. 7c and Fig. 7d present the results of the selection algorithm using these newly gained parameter estimates. Again, $p$ and $r$ initially do not cross the threshold. In fact, when performing a second iteration (Fig. 7d), only $r$ is of sufficient explanatory value to include in the model. The model fit worsens slightly when adding $p$, as the validation MSE increases with 0.7%. Therefore, this regressor is excluded from the model.

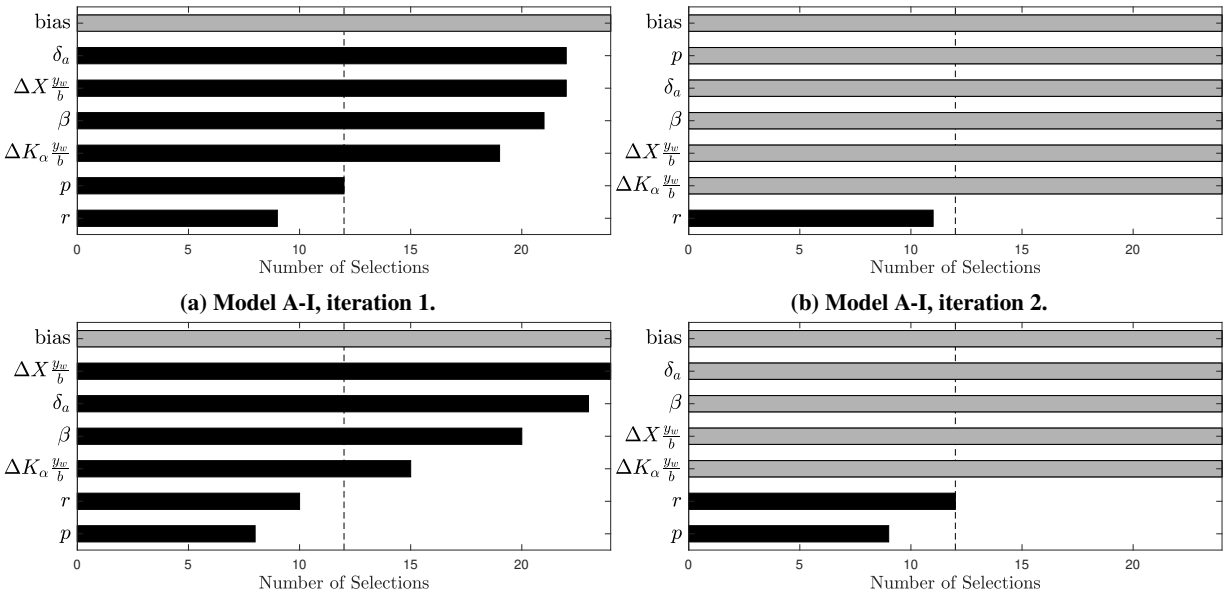


**(a) Model A-I, iteration 1.**




**(b) Model A-I, iteration 2.**




**(c) Model A-II, iteration 1.**




**(d) Model A-II, iteration 2.**

**Fig. 7 $C_l$-Model structure selection algorithm results, starting from Model A-I.**

*2. Model B*

Using Model B-I for $X$-parameter estimation further indicates that the inclusion of $\Delta X \frac{y_w}{b}$ leads to a higher $\alpha^*$ estimate than $\Delta K_\alpha \frac{y_w}{b}$, as presented in Table 4. The results of the selection algorithm using these $X$-parameter estimates can be found in Fig. 8a. Again, $\Delta X \frac{y_w}{b}$ is clearly preferred over $\Delta K_\alpha \frac{y_w}{b}$. This result is is to be expected, as the $X$-parameters were optimized using the former regressor. The rotational rates $p$ and $r$ do not satisfy the threshold. The preliminary collinearity analysis in Appendix VI.A show that from the asymmetric regressors, $p$, $K_\alpha \frac{y_w}{b}$, and $\Delta X \frac{y_w}{b}$ have a relatively high similarity. For the second iteration, it is chosen to evaluate the unique explanatory value of the $\Delta K_\alpha \frac{y_w}{b}$, $p$, by freezing $\Delta X \frac{y_w}{b}$, $\delta_a$ and $\beta$ into the model structure. As shown in Fig. 8b, the second iteration does include $r$, but $\Delta K_\alpha$ and $p$ are excluded, indicating that the latter regressors do not provide sufficient additional explanatory power to include them in addition to $\Delta X \frac{y_w}{b}$.

$$\text{Model B-II:} \quad \hat{C}_l(x,\theta) = C_{l_0} + C_{l_\beta}\beta + C_{l_r} r + C_{l_{\delta_a}}\delta_a + C_{L_X}\Delta X \frac{y_w}{b} \tag{45}$$

A final $X$-parameter estimation is performed using Model B-II. The obtained $X$-parameters (Table 4) lead to the selection algorithm results in Fig. 8c. Both asymmetric flow separation regressors are initially selected. With the same reasoning as in the previous paragraph, only $\Delta X \frac{y_w}{b}$ is frozen into the model, and a second iteration is performed. A similar result is observed: $p$ and the $\Delta K_\alpha \frac{y_w}{b}$ do not provide sufficient additional benefit. While $r$ only barely crosses the threshold, testing its contribution resulted in a validation MSE reduction of approximately 3%, leading to the decision to add it to the model. Hence, the roll moment model has converged to Eq. (45).

During these iterations, attempts were made to allow second-order regressors in the model, which only led to the selection of regressors that have little to no physical meaning. This also means that no cross-term with the flow separation variable could be found that adequately models the variations in aileron effectiveness.

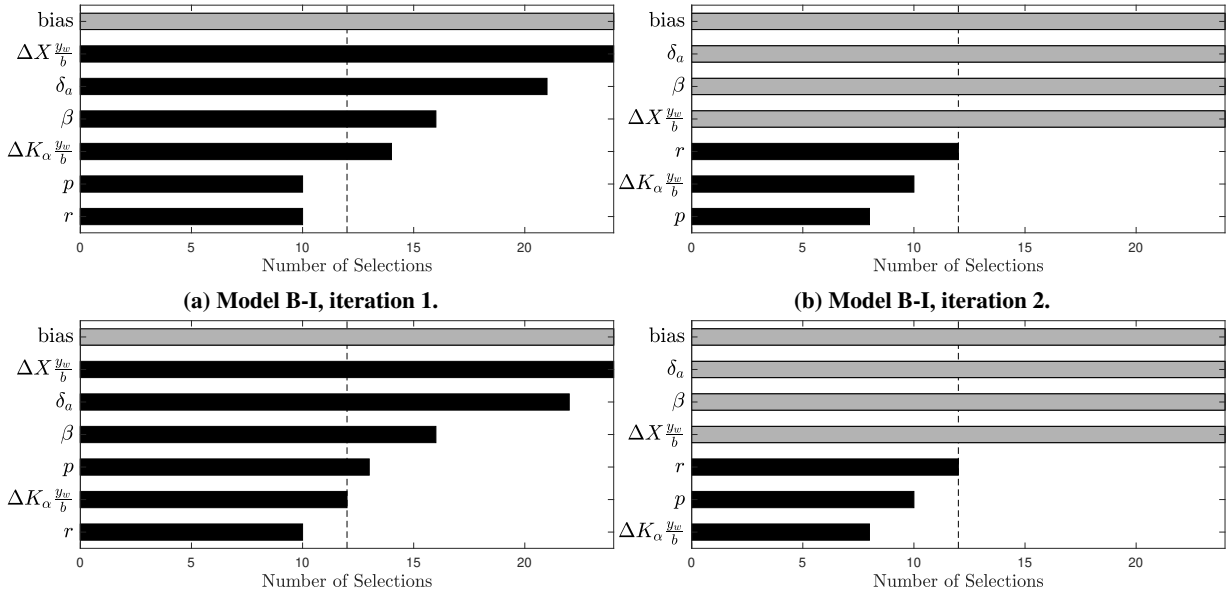


**(a) Model B-I, iteration 1.**




**(b) Model B-I, iteration 2.**




**(c) Model B-II, iteration 1.**




**(d) Model B-II, iteration 2.**

**Fig. 8 $Cl$-Model structure selection algorithm results, starting from Model B-I.**

To conclude the process of converging to two proposed roll moment models, the final structures are:

- Model A:

$$\hat{C}_l(x,\theta) = C_{l_0} + C_{l_\beta}\beta + C_{l_r} r + C_{l_{\delta_a}}\delta_a + C_{l_{\Delta K_\alpha}}\Delta K_\alpha \frac{y_w}{b} + C_{l_{\Delta X}}\Delta X \frac{y_w}{b} \tag{46}$$

- Model B:

$$\hat{C}_l(x,\theta) = C_{l_0} + C_{l_\beta}\beta + C_{l_r} r + C_{l_{\delta_a}}\delta_a + C_{l_{\Delta X}}\Delta X \frac{y_w}{b} \tag{47}$$

Table 5 presents the model fit for the intermediate and final models, on the validation set. The model fit metrics that are used in this paper are MSE and the explained variance $R^2$. For Model B, every step in the selection procedure improves the model fit, whereas Model A's performance deteriorates with the final step. The final Model B showcases an MSE reduction of approximately 10%, with respect to final Model A. This result indicates that the inclusion of the $\Delta K_\alpha$-term in Model A does not sufficiently improve the model, when the $\Delta X$-term is already included.

The contributions of each model term are presented for an example maneuver, in Fig. 9a and Fig. 9b, for Models A and B, respectively. The bottom plot presents the asymmetry in flow separation. Evidently, in Model A the $\Delta K_\alpha$-term has a much smaller contribution than the $\Delta X$-term. The contributions of the remaining terms are generally very similar between the models. Note that $r$ has a relatively small contribution to the model output. As discussed, this regressor is retained in the models due to its positive effect on the model fit.

**Table 5 Performance of the intermediate and the selected model structures, evaluated by the validation fit.**

| **Model Structure** | **MSE** | $\bar{R^2}$ | $min(R^2)$ | $max(R^2)$ |
|---|---|---|---|---|
| Model A-I | 1.78E-6 | 0.69 | 0.55 | 0.81 |
| Model A-II | 1.54E-6 | 0.75 | 0.59 | 0.83 |
| **Final Model A** | 1.57E-6 | 0.73 | 0.55 | 0.83 |
| Model B-I | 1.49E-6 | 0.74 | 0.55 | 0.85 |
| **Final Model B** | 1.41E-6 | 0.75 | 0.63 | 0.86 |

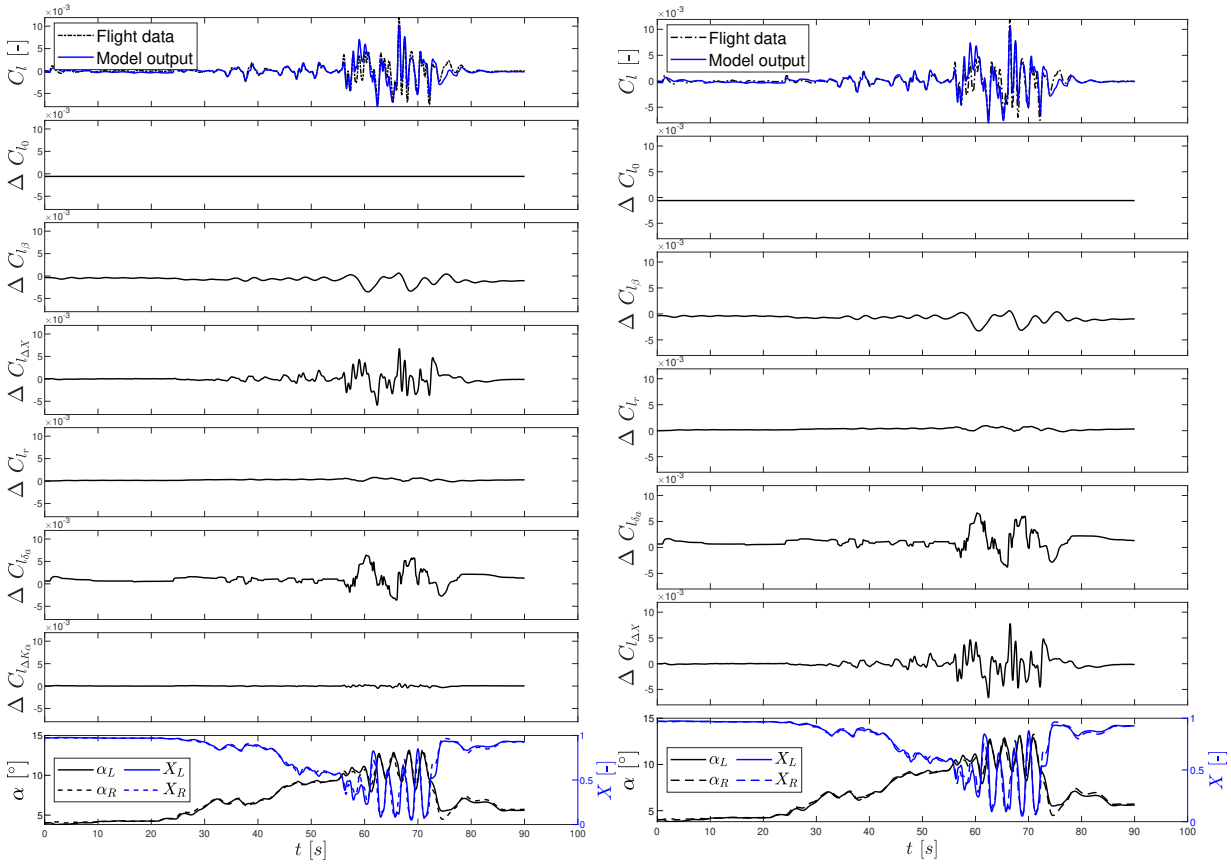


**(a) Model A.** **(b) Model B.**

**Fig. 9 Model term contributions to the output of the proposed $C_l$-models (ASYM set 7).**

### B. Step II: Nonlinear Optimization

The objective of Step II of Fig. 5 is to provide adequate estimates of the $X$-parameters. Since there is no flow separation measurement available, the estimates are analyzed by their variances, distributions, and a comparison with the baseline stall model. The optimization is verified by a cost function analysis and a comparison of nonlinear optimization results with the results of linear regression.

*1. X-Parameter Estimates Analysis*

In the following discussions, only the final selected structures of Models A and B are considered. The $X$-parameter estimates and their standard deviations can be found in Table 6, for both proposed models and the baseline model [15]. Generally, the estimates of Model B have smaller standard deviations than the Model A estimates, with the exception of $\sigma_{\tau_2}$ of Model A being roughly 2% smaller than that of Model B. The general trend of differences in variances between these models is likely due to $\Delta X$ and $\Delta K_\alpha$ providing similar contributions to the model output. Since Model B only includes $\Delta X$, such ambiguity does not exist. While the parameter values are generally quite close between the proposed models, the largest relative difference is observed for $\tau_2$. This is also the parameter with the largest relative estimate variance.

The newly found $X$-parameter estimates provide insight into the fundamental difference between the proposed roll-based method and the lift-based method that was used for the baseline model. Evidently from Table 6, the variances of the parameter estimates are generally much smaller for Models A and B, than for the baseline model. For instance, $\sigma_{\tau_1}$ and $\sigma_{a_1}$ of Model B are over 80% smaller than the corresponding baseline model estimates. Conversely, $\sigma_{\tau_2}$ of the proposed method is almost twice as large as for the lift-based method. A possible reason for this observation is the fact that many of the lift-based $\tau_2$ estimates were close to the lower bound of zero [15]. If the feasible region had been larger,

the variance may have been larger as well. $\sigma_{\alpha^*}$ are relatively close for each model, indicating that the onset of the stall is identifiable from both the lift and roll moment, with similar certainty.

Clear differences exist between the lift-based and roll-based parameter estimates. The roll-based method returns an $\alpha^*$ estimate of approximately 9.9° (Model B), whereas the lift-based approach yields $\alpha^* = 11.9°$, indicating that the lateral nonlinear effects occur at a lower angle of attack than the lift loss. However, the $a_1$ estimates of the roll-based method are between 35% and 40% smaller than that of the lift-based approach, implying that the lateral stall effects occur earlier, but are less abrupt. Mathematically, $a_1$ scales with the value of $\tau_2$, which could mean that this scaling parameter compensates for the relatively high value of $\tau_2$. An explanation of the discrepancy between $\tau_1$ and $\tau_2$ estimates between the roll-based and lift-based methods is based on the ODEs of the flow separation points, introduced in Eq. (17). $\tau_1$ and $\tau_2$ describe similar lagging effects, but they are modeled differently in a mathematical sense. $\tau_2$ determines the lag or hysteresis effect due to the local angle of attack rates. The asymmetric flow separation regressors both describe some differential of the flow separation variables. The local angle of attack differential between the wings is strongly correlated with the roll rate, as will be further discussed in Section V. Hence, the time-derivative of this differential, represented by the asymmetric stall regressors, is likely correlated with the rotational acceleration in the roll axis, and therefore with the roll moment. This could explain why the $\tau_2$ estimate of the proposed method is much larger and the remaining lag parameter $\tau_1$ smaller. Increasing $\tau_2$, thereby enhancing the asymmetric stall regressor's similarity to the local angle of attack rate differential, increases the similarity of the regressor with the roll moment.

**Table 6** $X$**-parameter estimates using the selected roll moment model and the previous lift-based method. The lowest standard deviation of a given parameter is bold-faced.**

| | Optimization | Model A | | Model B | | Baseline Model [15] | |
|---|---|---|---|---|---|---|---|
| $\theta$ | Bounds | $\hat{\theta}$ | $\sigma_{\hat{\theta}}$ | $\hat{\theta}$ | $\sigma_{\hat{\theta}}$ | $\hat{\theta}$ | $\sigma_{\hat{\theta}}$ |
| $\tau_1$ [s] | [0.001, 0.50] | 0.0923 | 0.0459 | 0.0971 | **0.0282** | 0.2547 | 0.1565 |
| $\tau_2$ [s] | [0.000, 0.80] | 0.4487 | 0.1409 | 0.5526 | 0.1636 | 0.0176 | **0.0819** |
| $a_1$ [-] | [15.00, 40.0] | 18.203 | 1.4527 | 16.865 | **1.1672** | 27.671 | 6.7177 |
| $\alpha^*$ [rad] | [0.100, 0.35] | 0.1694 | 0.0253 | 0.1730 | **0.0194** | 0.2084 | 0.0202 |

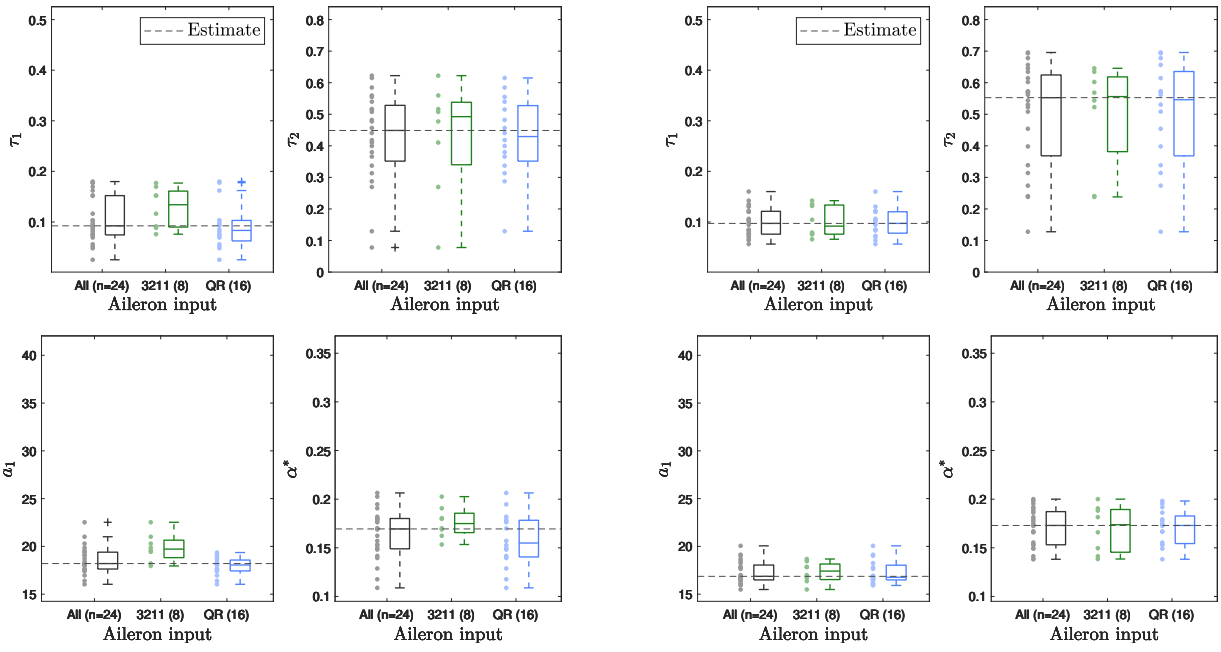


**(a) Model A** **(b) Model B**

**Fig. 10** $X$**-parameter estimates distribution over the training sets, grouped by the type of dynamic aileron input.**

The distribution of the $X$-parameter estimates over the training sets is visualized by means of box plots in Fig. 10a and Fig. 10b, for Models A and B, respectively. The plots are grouped by the aileron input that was applied during the stall maneuver. The parameters of Model A are more sensitive to the type of aileron input than the parameters of Model B. Most notably for $a_1$, the boxes of the 3-2-1-1 and QR maneuvers do not overlap. From both figures, it is confirmed that $\tau_2$ is the most difficult parameter to identify, as the estimates cover a large part of the feasible solution space.

*2. Nonlinear Optimization Analysis*

The nonlinear optimization indirectly influences the model performance, as the linear regression step aims to optimize the same model structure. Unlike this nonlinear optimization, the linear regression technique described in Section III.G provides a guaranteed global optimum. The $C_l$-parameters are estimated for both processes, allowing for the verification of the nonlinear optimization results. The correlation plots of Fig. 11a and Fig. 11b display the $C_l$-parameter estimates from all training sets, for Models A and B, respectively. On the horizontal axis, the results from OLS are displayed, and the vertical axis represents the results obtained from the Interior Point (IP) method. When the methods yield similar results, a distinct diagonal pattern is observable. Additionally, Pearson's linear correlation coefficient between the sets is included in each plot. While this analysis cannot prove the convergence to a global optimum of the $X$-parameters, it provides insight into the consistency of the found solutions.

Generally, Model B exhibits a significantly stronger similarity in parameter estimates compared to Model A. Specifically, when examining Model A, the estimates for $C_{l_{\Delta X}}$ display the weakest correlation. Conversely, the $C_{l_{\Delta K_\alpha}}$ estimates are highly correlated. The optimization process may encounter difficulties when the corresponding regressors depict similar phenomena. The optimizations of Model B exhibit a high correlation for the estimates of every parameter. Especially important to highlight is the high correlation coefficient between the optimizations of $C_{l_{\Delta X}}$, further motivating the inclusion of only a single asymmetric stall regressor.

From the results of the MOF-algorithm, the validation model fit evaluations and the analysis in this section, Model B is identified as the most suitable $C_l$-model structure. The associated estimated $X$-parameters are used for the selection of the remaining models and the resulting linear regression problems.

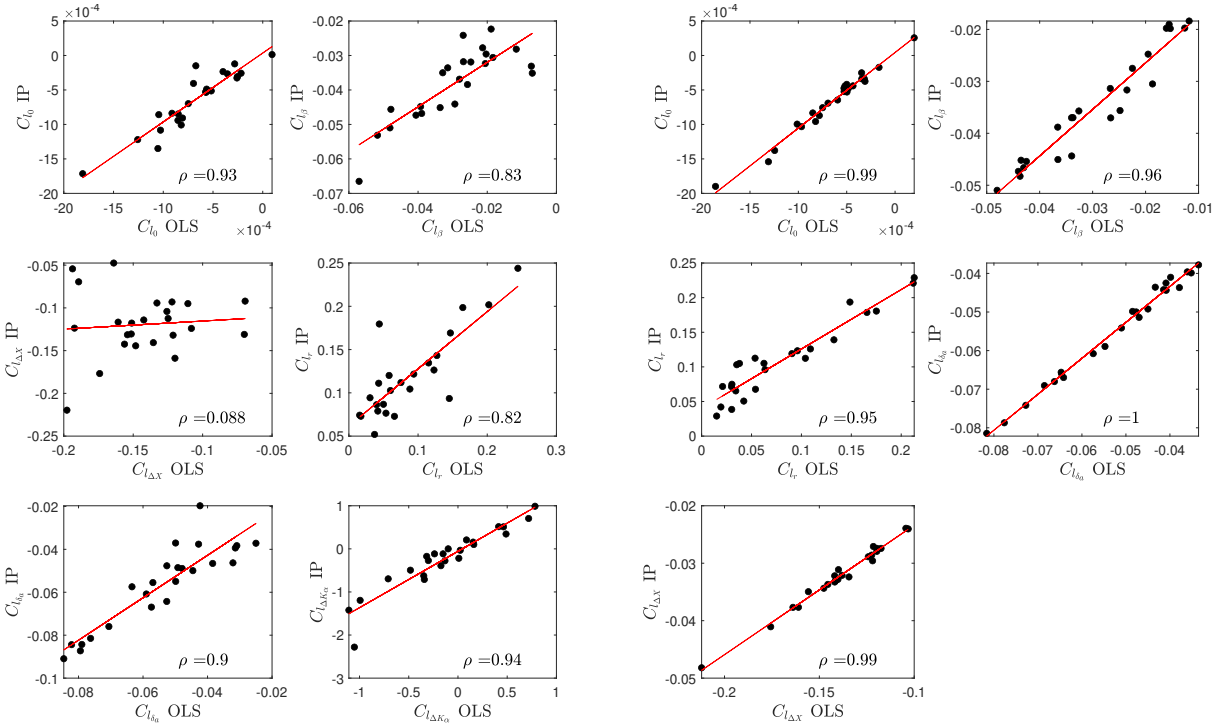


**(a) Model A.** **(b) Model B.**

**Fig. 11 Correlation plots showing the similarity between the linear and nonlinear optimization results. $\rho$ denotes Pearson's linear correlation coefficient between the sets of estimates.**

### C. Step IIIb: Remaining Force and Moment Coefficient Models

The remaining model structures are selected using the $X$-parameter estimates associated to the selected $C_l$-model. This section describes this selection procedure. The performed analyses are based on the results of the MOF-algorithm, validation fit after performing OLS, comparisons with literature, and the visible contributions of regressors to the model output.

#### *1. $C_n$-model*

The selection algorithm results in Fig. 12a indicate that $\beta$ and $\Delta X \frac{y_w}{b}$ are the regressors with the most explanatory value for the yaw moment model. Interestingly, the algorithm selects not only the rudder deflection but also the aileron deflection. The value of including these regressors is confirmed by Fig. 12b, displaying the contribution of each model term. $p$ is also considered but adding it to the structure increases the validation MSE by over 40%, eliminating it from consideration. Instead, $r$ is included in the first iteration, as the literature suggests it is essential in describing the yaw moment [15, 19]. In the second iteration, $\alpha$ is identified as a suitable candidate. In literature, this regressor is not usually part of the yaw moment model, as it only describes the symmetric flow variations [15, 22]. While its contribution in Fig. 12b is small, adding this regressor improved the model validation fit, by a 19% MSE reduction. Also, note that this model term is most active during the stall, which could mean that it provides a correction of a bias generated by the selected asymmetric stall term. The final $C_n$ model structure is thus obtained:

$$\hat{C}_n = C_{n_0} + C_{n_\beta}\beta + C_{n_r} r + C_{n_{\delta_a}}\delta_a + C_{n_{\delta_r}}\delta_r + C_{n_{\Delta X}}\Delta X \frac{y_w}{b} + C_{n_\alpha}\alpha \tag{48}$$

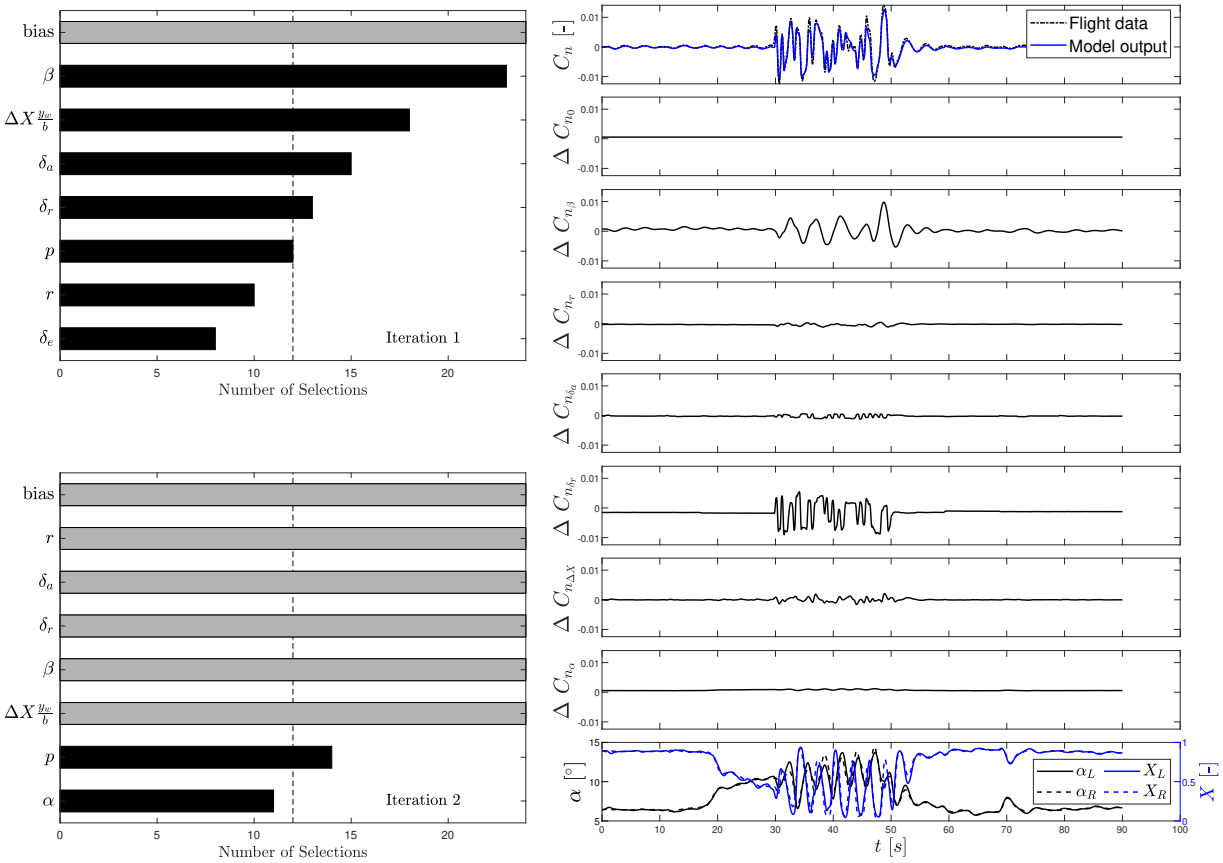


**(a) Results of 2 iterations of the MOF algorithm.** **(b) Model term contributions, after OLS (ASYM set 16).**

**Fig. 12 $C_n$-model structure selection results.**

*2. $C_Y$-model*

The selection algorithm was run for the lateral force model to obtain the regressors displayed in Fig. 13a. The contributions of the selected model terms can be found in Fig. 13b. Similarly to the $C_l$-model and $C_n$-model, $\Delta X \frac{y_w}{b}$ is preferred over $\Delta K_\alpha \frac{y_w}{b}$. Again, both the aileron and rudder deflections are selected in the first iteration. Notably, $p$ and $r$ are excluded in the first iteration. In the second iteration, $r$ is included and $p$ is excluded. Moreover, adding $p$ again deteriorated the validation fit, leading to the decision to exclude it. The model structure selection process for the lateral force has resulted in

$$\hat{C}_Y = C_{Y_0} + C_{Y_\beta}\beta + C_{Y_r} r + C_{Y_{\delta_a}} \delta_a + C_{Y_{\delta_r}} \delta_r + C_{Y_{\Delta X}} \Delta X \frac{y_w}{b} \tag{49}$$

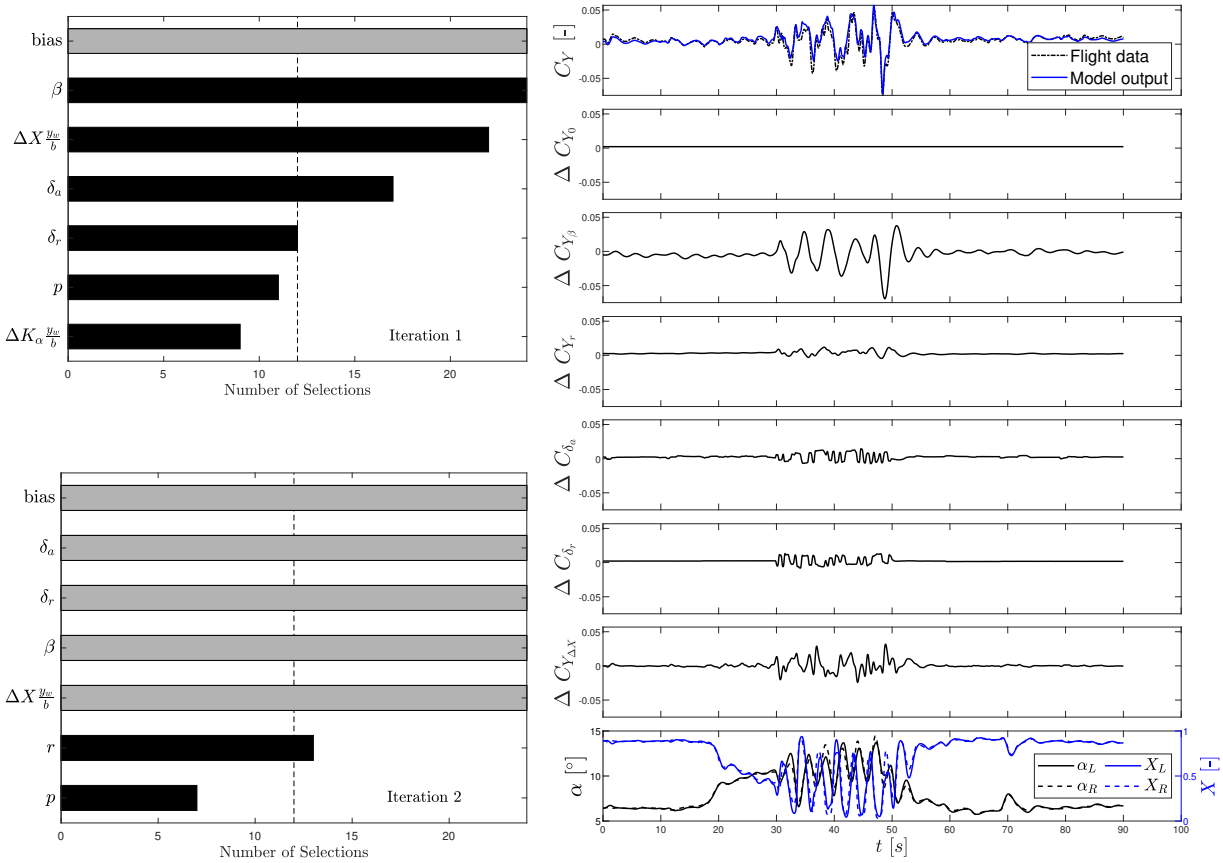


**(a) Results of 2 iterations of the MOF algorithm.** **(b) Model term contributions, after OLS (ASYM set 16).**

**Fig. 13 $C_Y$-model structure selection results.**

*3. Longitudinal Models*

As previously discussed, the longitudinal model structures are taken directly from previous work [15]. For completeness, they are included in this model structure description. The longitudinal model structures include three transformations of $X$, one for each model:

$$\begin{aligned}
\hat{C}_L &= C_{L_0} + C_{L_\alpha} \left( \frac{1+\sqrt{X}}{2} \right)^2 \alpha + C_{L_{\alpha^2}} (\alpha - 6°)_+^2 \\
\hat{C}_D &= C_{D_0} + C_{D_\alpha}\alpha + C_{D_{\delta_e}}\delta_e + C_{D_X}(1-X) + C_{D_{C_T}} C_T \\
\hat{C}_m &= C_{m_0} + C_{m_\alpha}\alpha + C_{m_{X\delta_e}} \max(0.5, X)\delta_e + C_{m_{C_T}} C_T
\end{aligned} \tag{50}$$

The Kirchhoff term is included in the lift model. As Kirchhoff's model was developed for airfoils, a correction term is added to model the entire aircraft lift, based on a univariate spline in $\alpha$ with zero-order continuity:

$$(\alpha - 6^\circ)_+^2 = \begin{cases} (\alpha - 6^\circ)^2 & \text{when} \quad \alpha \geq 6^\circ \\ 0 & \text{when} \quad \alpha < 6^\circ \end{cases} \tag{51}$$

The $(1 - X)$-term in the drag model describes a drag increase due to flow separation. Finally, $\max(0.5, X)\delta_e$ in the pitch moment model provides a reducing effect on the elevator effectiveness, with an upper limit of 50% reduction.

### D. Step IV: Aerodynamic Parameter Estimates

Table 7a and Table 7b present the outcomes of the parameter estimation process for the asymmetric and symmetric aerodynamic model equations, respectively. These tables display the estimated parameter values, the standard deviations of the estimates across the data sets, and the findings of two statistical tests. The one-sample Kolmogorov-Smirnov (KS) test provides a test decision, regarding the null hypothesis that the estimates from the data sets follow a standard normal distribution, as opposed to the alternative hypothesis that they do not conform to such a distribution [29]. In the current estimation problem, this test provides a method of outlier detection. Also, if the estimates are significantly non-normal, it could be worth considering alternative model structures that better account for the data distribution. The one-sample parametric $t$-test here returns a test decision for the null hypothesis that the population mean is equal to zero, against the alternative of a non-zero mean. In this case, the $t$-test can provide information on whether a parameter should be included in the model at all. Significance levels of 0.1 and 0.01 were used, for the KS-tests and $t$-tests, respectively. A Bonferroni correction was applied for the $t$-test, to combat the multiple comparisons problem. This problem is introduced due to simultaneously considering a set of statistical inferences, one for each parameter per model [30].

According to the KS-test results, all estimated aerodynamic parameters can be assumed to originate from a normal distribution. The $t$-test returns that the bias parameters of $C_n$, $C_Y$, and $C_D$ are zero-mean. The biases of the lateral-directional models are expected to be small as these coefficients generally oscillate around zero. A small drag bias was also identified by van Ingen et al. [15], who hypothesized that the inclusion of $C_{D_{C_T}}$ caused this effect. These bias parameters are all retained in the models, due to their persisting importance for modeling any constant offsets. The $C_{Y_{\delta_r}}$ estimates are also close to zero. This result is also in line with the findings of van Ingen et al. [15], where $C_{Y_{\delta_r}}$ was not even included in the model structure, due to a negative effect on the validation fit. In the current case, the parameter was retained due to its positive influence on the validation fit, as discussed in Section IV.C. This discrepancy is likely due to the application of more rudder inputs throughout ASYM than VAN INGEN.

In Table 8, correlation matrices can be found for the parameters of every model. The data indicates that the $\alpha$-related parameters of the longitudinal models are correlated with the bias parameters. In general, the correlations are caused by pre-stall stretches of approximately constant angle of attack in the training sets. The pair $(C_{L_0}, C_{L_\alpha})$ in Table 8d, showcase an especially strong correlation of $\rho = 0.98$. Note that van Ingen et al. [15] also identified strong correlations for this pair, $\rho = 0.90$. However, the fact that the current $C_{L_\alpha}$ estimates are even more similar to the bias parameter estimates indicates that the current $X$-parameters are less suitable for modeling the lift using Kirchhoff's model than van Ingen's $X$-parameters. While the model term associated with $C_{L_\alpha}$ still has a strong positive effect on the model fit, the estimates are less certain as the standard deviations of $C_{L_0}$ and $C_{L_\alpha}$ are approximately doubled. All $\alpha$-related parameters were retained in the model, due to their strong positive contributions to model fit.

Finally, consider the estimate of the lateral control surface effectiveness parameter, $C_{l_{\delta_a}} = -0.0501$. The flow separation variables were ineffective at describing any variations in the roll control authority, as explained in Section IV.A. However, the estimate is 41% smaller than the estimate of the baseline model, $C_{l_{\delta_a}} = -0.0853$ [15]. Note that the latter model did not include any stall-related model terms in the roll moment model structure. The only difference between the structures of these models is the swapping of $p$ with $\Delta X \frac{y_w}{b}$. Interestingly, $\Delta X \frac{y_w}{b}$ is less correlated with $\delta_a$ than $p$, as can be seen in Appendix VI.A. As a result, the standard deviation of the $C_{l_{\delta_a}}$ estimates is less than half of the value of the previous model, indicating an improved certainty of the parameter estimate.

**Table 7 Aerodynamic parameter estimates, with standard deviations and results of statistical tests. KS-test: N = normally distributed, X = not normally distributed. $t$-test: o = zero-mean, * = not zero-mean,**

**(a) Asymmetric models.**

| | Estimates | | KS-test | | $t$-test | |
|---|---|---|---|---|---|---|
| $\theta_{C_i}$ [-] | $\hat{\theta}$ | $\sigma_{\hat{\theta}}$ | $p$ | $h$ | $p$ | $h$ |
| $C_{l_0}$ | -0.0006 | 0.0004 | 0.5267 | N | 0.0389 | * |
| $C_{l_\beta}$ | -0.0279 | 0.0108 | 0.7790 | N | 0.0000 | * |
| $C_{l_r}$ | 0.0661 | 0.0562 | 0.8271 | N | 0.6019 | * |
| $C_{l_{\delta_a}}$ | -0.0501 | 0.0104 | 0.6221 | N | 0.0000 | * |
| $C_{l_{\Delta X}}$ | -0.1274 | 0.0145 | 0.7102 | N | 0.0000 | * |
| $C_{n_0}$ | 0.0006 | 0.0011 | 0.8810 | N | 0.0687 | o |
| $C_{n_\beta}$ | 0.0709 | 0.0093 | 0.7497 | N | 0.0000 | * |
| $C_{n_r}$ | -0.0598 | 0.0590 | 0.6226 | N | 0.0000 | * |
| $C_{n_{\delta_a}}$ | 0.0113 | 0.0043 | 0.9600 | N | 0.0000 | * |
| $C_{n_{\delta_r}}$ | 0.0493 | 0.0267 | 0.1090 | N | 0.0000 | * |
| $C_{l_{\Delta X}}$ | -0.0302 | 0.0110 | 0.3024 | N | 0.0000 | * |
| $C_{n_\alpha}$ | 0.0049 | 0.0056 | 0.5810 | N | 0.0000 | * |
| $C_{Y_0}$ | 0.0021 | 0.0100 | 0.5576 | N | 0.2691 | o |
| $C_{Y_\beta}$ | -0.5013 | 0.0629 | 0.9420 | N | 0.0000 | * |
| $C_{Y_r}$ | 0.6204 | 0.5314 | 0.8824 | N | 0.0001 | * |
| $C_{Y_{\delta_a}}$ | -0.1344 | 0.0390 | 0.9847 | N | 0.0000 | * |
| $C_{Y_{\delta_r}}$ | -0.0725 | 0.2683 | 0.2270 | N | 0.0917 | o |
| $C_{Y_{\Delta X}}$ | -0.4588 | 0.0663 | 0.8865 | N | 0.0000 | * |

**(b) Symmetric models.**

| | Estimates | | KS-test | | $t$-test | |
|---|---|---|---|---|---|---|
| $\theta_{C_i}$ [-] | $\hat{\theta}$ | $\sigma_{\hat{\theta}}$ | $p$ | $h$ | $p$ | $h$ |
| $C_{L_0}$ | 0.2480 | 0.0897 | 0.9210 | N | 0.0000 | * |
| $C_{L_\alpha}$ | 4.3991 | 0.8553 | 0.7341 | N | 0.0000 | * |
| $C_{L_{\alpha^2}}$ | 18.854 | 5.2721 | 0.3663 | N | 0.0000 | * |
| $C_{D_0}$ | -0.0078 | 0.0167 | 0.9037 | N | 0.0038 | o |
| $C_{D_\alpha}$ | 0.3372 | 0.1219 | 0.7914 | N | 0.0000 | * |
| $C_{D_{\delta_e}}$ | -0.1715 | 0.0743 | 0.8754 | N | 0.0000 | * |
| $C_{D_{1-X}}$ | 0.0246 | 0.0120 | 0.9937 | N | 0.0000 | * |
| $C_{D_{C_T}}$ | 0.4301 | 0.0743 | 0.6382 | N | 0.0000 | * |
| $C_{m_0}$ | 0.0324 | 0.0190 | 0.9607 | N | 0.0000 | * |
| $C_{m_\alpha}$ | -0.5497 | 0.1171 | 0.6830 | N | 0.0000 | * |
| $C_{m_{\delta_e X}}$ | -0.9220 | 0.1445 | 0.8446 | N | 0.0000 | * |
| $C_{m_{C_T}}$ | 0.0857 | 0.0974 | 0.9830 | N | 0.0004 | * |

### E. Stall Model Validation

The presented aerodynamic parameters have resulted in a 6-DOF stall model, that should be capable of adequately describing the nonlinearities of flow separation. To validate the model, the model fit is evaluated using the validation data set. This data set contains 6 stall maneuvers and was not used in the identification phase. Refer to Table 2 for the contents of the data set. Table 9 presents the results of the training procedure and this validation step. The training and validation model fit metrics are in similar ranges, indicating that the model has been neither overfitted, nor underfitted.

The validation fit is visualized in Fig. 14, which presents the model output of the best- and worst-performing validation sets. Both Table 9 and Fig. 14 present a satisfactory agreement with the data of the lateral-directional models. This result confirms that using a flow separation differential in the roll moment model structure allows for the identification of asymmetric flow separation characteristics. Moreover, the identified flow separation variables are capable of adequately capturing the nonlinearities of the lateral force and the yaw moment.

Conversely, the longitudinal models present a lacking description of the flight data. The model structures were directly taken from a validated stall model. $X$ is computed by averaging the local flow separation variables $X_L$ and $X_R$, which are each evaluated using the roll-based $X$-parameter estimates. This approach is less suitable for longitudinal stall modeling using Kirchhoff's method, as the resulting flow separation variable is not fully capable of accurately describing the flow separation effects of the drag and the pitch moment. For instance, some of the maneuver sets have a negative $R^2$ value. This means that the prediction is worse than the mean of the measurement, generally indicating a poor model fit. The lift model provides a decent prediction of the validation data, as the explained variance ranges from 0.63 to 0.86. The resulting stall model will be compared to alternatives in Section V to gain more perspective on its validity.

**Table 8 Correlation matrices of the aerodynamic force and moment parameter estimates. Entries with absolute values larger than or equal to 0.75 are highlighted.**

**(a) $C_l$-parameters.**

| | $C_{l_0}$ | $C_{l_\beta}$ | $C_{l_r}$ | $C_{l_{\delta_a}}$ | $C_{l_{\Delta X}}$ |
|---|---|---|---|---|---|
| $C_{l_0}$ | 1.00 | | | | |
| $C_{l_\beta}$ | 0.08 | 1.00 | | | |
| $C_{l_r}$ | -0.10 | -0.46 | 1.00 | | |
| $C_{l_{\delta_a}}$ | 0.51 | 0.52 | -0.12 | 1.00 | |
| $C_{l_{\Delta X}}$ | 0.04 | -0.35 | 0.20 | 0.11 | 1.00 |

**(b) $C_n$-parameters.**

| | $C_{n_0}$ | $C_{n_\beta}$ | $C_{n_r}$ | $C_{n_{\delta_a}}$ | $C_{n_{\delta_r}}$ | $C_{n_{\Delta X}}$ | $C_{n_\alpha}$ |
|---|---|---|---|---|---|---|---|
| $C_{n_0}$ | 1.00 | | | | | | |
| $C_{n_\beta}$ | -0.01 | 1.00 | | | | | |
| $C_{n_r}$ | 0.06 | -0.52 | 1.00 | | | | |
| $C_{n_{\delta_a}}$ | -0.07 | 0.19 | 0.23 | 1.00 | | | |
| $C_{n_{\delta_r}}$ | **0.80** | 0.41 | -0.03 | 0.14 | 1.00 | | |
| $C_{n_{\Delta X}}$ | -0.01 | -0.41 | 0.30 | -0.05 | -0.13 | 1.00 | |
| $C_{n_\alpha}$ | -0.39 | 0.30 | -0.06 | 0.38 | 0.14 | -0.06 | 1.00 |

**(c) $C_Y$-parameters.**

| | $C_{Y_0}$ | $C_{Y_\beta}$ | $C_{Y_r}$ | $C_{Y_{\delta_a}}$ | $C_{Y_{\delta_r}}$ | $C_{Y_{\Delta X}}$ |
|---|---|---|---|---|---|---|
| $C_{Y_0}$ | 1.00 | | | | | |
| $C_{Y_\beta}$ | -0.07 | 1.00 | | | | |
| $C_{Y_r}$ | 0.44 | -0.39 | 1.00 | | | |
| $C_{Y_{\delta_a}}$ | 0.08 | 0.39 | 0.02 | 1.00 | | |
| $C_{Y_{\delta_r}}$ | **0.89** | 0.08 | 0.29 | -0.03 | 1.00 | |
| $C_{Y_{\Delta X}}$ | 0.27 | -0.46 | 0.29 | -0.51 | 0.24 | 1.00 |

**(d) $C_L$-parameters.**

| | $C_{L_0}$ | $C_{L_\alpha}$ | $C_{l_{\alpha^2}}$ |
|---|---|---|---|
| $C_{L_0}$ | 1.00 | | |
| $C_{L_\alpha}$ | **-0.98** | 1.00 | |
| $C_{l_{\alpha^2}}$ | -0.01 | -0.09 | 1.00 |

**(e) $C_D$-parameters.**

| | $C_{D_0}$ | $C_{D_\alpha}$ | $C_{D_{\delta_e}}$ | $C_{D_{1-X}}$ | $C_{D_{C_T}}$ |
|---|---|---|---|---|---|
| $C_{D_0}$ | 1.00 | | | | |
| $C_{D_\alpha}$ | **-0.86** | 1.00 | | | |
| $C_{D_{\delta_e}}$ | 0.04 | 0.38 | 1.00 | | |
| $C_{D_{1-X}}$ | 0.55 | **-0.75** | -0.37 | 1.00 | |
| $C_{D_{C_T}}$ | -0.55 | 0.19 | -0.40 | -0.04 | 1.00 |

**(f) $C_m$-parameters.**

| | $C_{m_0}$ | $C_{m_\alpha}$ | $C_{m_{\delta_e X}}$ | $C_{m_{C_T}}$ |
|---|---|---|---|---|
| $C_{m_0}$ | 1.00 | | | |
| $C_{m_\alpha}$ | **-0.79** | 1.00 | | |
| $C_{m_{\delta_e X}}$ | 0.30 | 0.25 | 1.00 | |
| $C_{m_{C_T}}$ | **-0.76** | 0.52 | -0.20 | 1.00 |

**Table 9 Aerodynamic model fit properties, averaged over the training sets and validation sets.**

| | **Training** | | | | **Validation** | | | |
|---|---|---|---|---|---|---|---|---|
| Model | MSE | $\bar{R^2}$ | $min(R^2)$ | $max(R^2)$ | MSE | $\bar{R^2}$ | $min(R^2)$ | $max(R^2)$ |
| $C_l$ | 1.03E-6 | 0.77 | 0.42 | 0.89 | 1.41E-6 | 0.75 | 0.63 | 0.86 |
| $C_n$ | 4.85E-7 | 0.65 | 0.27 | 0.89 | 8.50E-7 | 0.68 | 0.36 | 0.92 |
| $C_Y$ | 4.11E-5 | 0.63 | 0.16 | 0.92 | 5.73E-5 | 0.65 | 0.25 | 0.89 |
| $C_L$ | 4.09E-3 | 0.80 | 0.55 | 0.91 | 3.51E-3 | 0.78 | 0.67 | 0.87 |
| $C_D$ | 1.13E-4 | 0.70 | -0.15 | 0.84 | 1.10E-4 | 0.67 | 0.29 | 0.80 |
| $C_m$ | 2.10E-4 | 0.50 | -0.34 | 0.80 | 1.83E-4 | 0.43 | -0.25 | 0.64 |

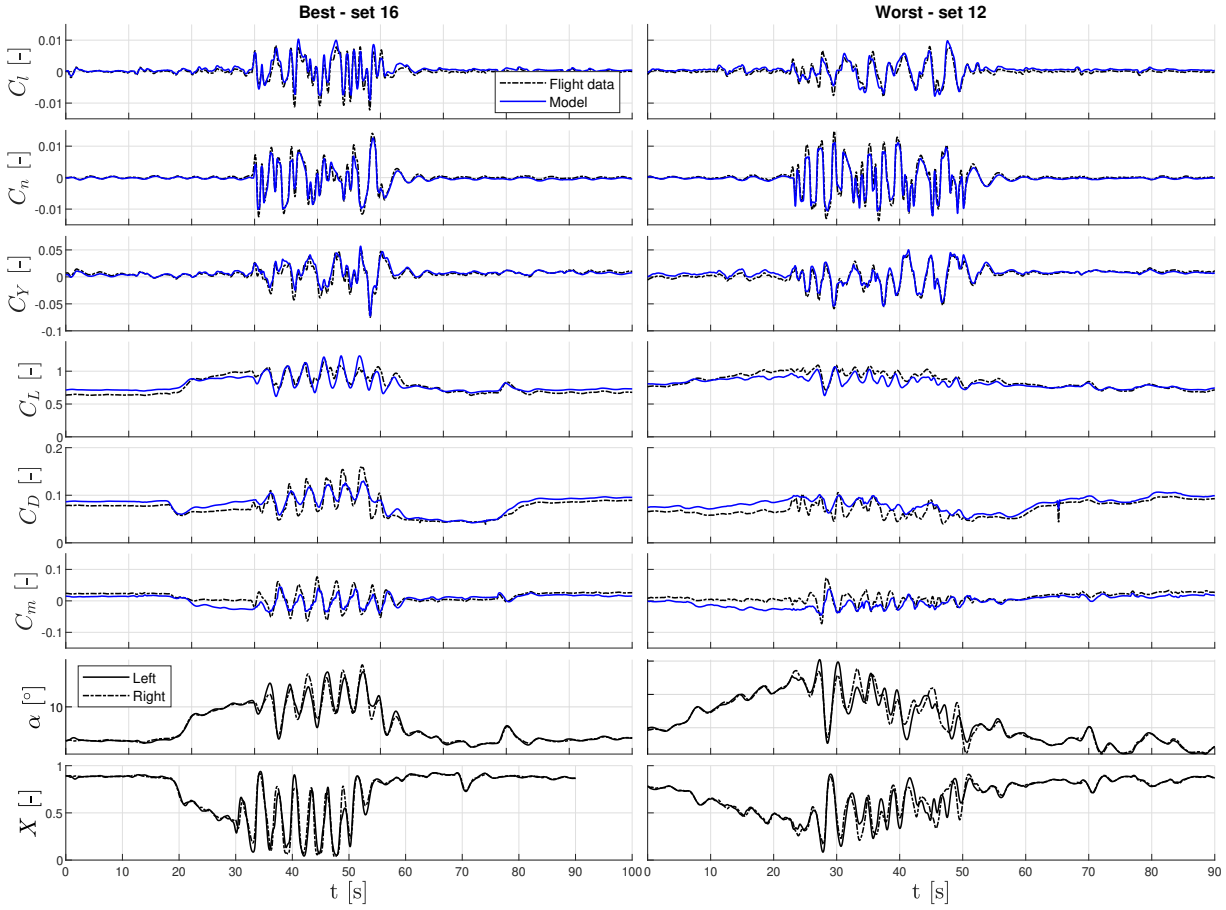


**Fig. 14 Model validation plots, presenting the model output of the best- and worst-performing validation sets.**

## V. Discussion

This research has presented a methodology for identifying asymmetry in aircraft stall characteristics, based on flight data. Using this methodology, a stall model was created for TU Delft's Cessna Citation II laboratory aircraft. New flight experiments were conducted to maximally excite the stall-related dynamics in the lateral-directional axes of the aircraft. The identification approach consists of estimating flow separation development using the flight-derived roll moment, and subsequently estimating aerodynamic model parameters. This section discusses the results of the presented model, starting with an analysis of the proposed asymmetric stall regressors. The model performance is then compared with previous models of the aircraft. Finally, the work that remains for future efforts to obtain a full-envelope stall model is discussed.

### A. Analysis of Asymmmetric Stall Regressors

In this paper, two options were presented to describe flow separation asymmetry. Both approaches are based on the assumption that the roll moment contains the most information on flow separation asymmetry, as it is a direct description of wing lift asymmetry. The flow separation variables $X_L$ and $X_R$ were defined for the left and the right wing, respectively. The first option was to apply Kirchhoff's flow separation lift model to the left and right wing surfaces, to obtain a description of lift differential ($\Delta K_\alpha$, as introduced in Eq. (15)). The second option contains no direct information on the local angles of attack and simply describes the difference between the flow separation variables ($\Delta X$). Note that the parameters of these variables are still estimated using the local angles of attack.

Since the pre- and post-stall regions are included in the training sets, some portion of the data has little to no flow separation on either wing surface, meaning $X_L \approx X_R \approx 1$. In this case, $\Delta K_\alpha$ reduces to $\alpha_L - \alpha_R = \Delta\alpha$ and $\Delta X = 0$. The angle of attack differential, by itself, provides no information on flow separation. It merely provides some description of

the rolling motion of the aircraft. In fact, $p$ and $\Delta\alpha$ are strongly inversely correlated, as evidenced by Fig. 15. Generally, for every data set the correlation coefficient between these variables $|\rho| > 0.99$. This result comes from the computation method of the local angles of attack, which is recounted here:

$$\alpha_P = \text{atan}\left(\frac{w_P}{u_P}\right) = \text{atan}\left(\frac{w - q\Delta x_P + p\Delta y_P}{u - r\Delta y_P + q\Delta z_P}\right) \tag{52}$$

where the only nonzero offset is $\Delta y_P$ for the current purpose, and $r$ is generally much smaller than $p$ during the performed stall maneuvers. This makes the difference between $\alpha_L$ and $\alpha_R$ almost entirely dependent on $p$.

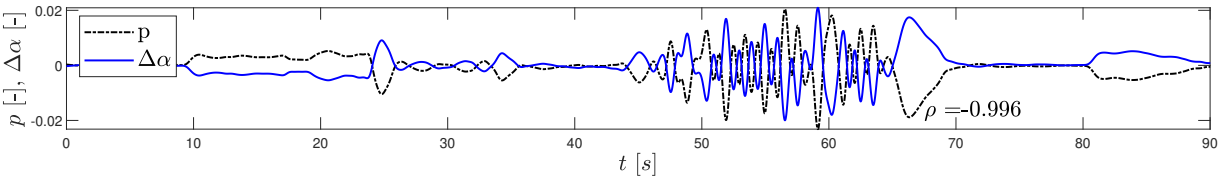


**Fig. 15 Visualization of the inverse correlation between $p$ and $\Delta\alpha$ (ASYM set 8).**

To investigate any potential estimation issues when including either asymmetric flow separation terms, the $X$-parameters from the baseline model [15] are used to analyze the correlation of these parameters with $p$. The results are presented in Fig. 16. Three time-intervals are analyzed: pre-stall, deep stall and post-stall. These intervals are crudely defined as follows: deep stall occurs when $X < 0.75$ for the first time, and finishes when this threshold is crossed for the last time. Evidently, the degree of correlation between $p$ and $\Delta K_\alpha$ is highly dependent on the amount of flow separation, as the deep stall region showcases a much smaller correlation than the pre- and post-stall regions. This phenomenon is not clearly observed for the pair ($p$,$\Delta X$), between which the correlation is low to moderate in each region.

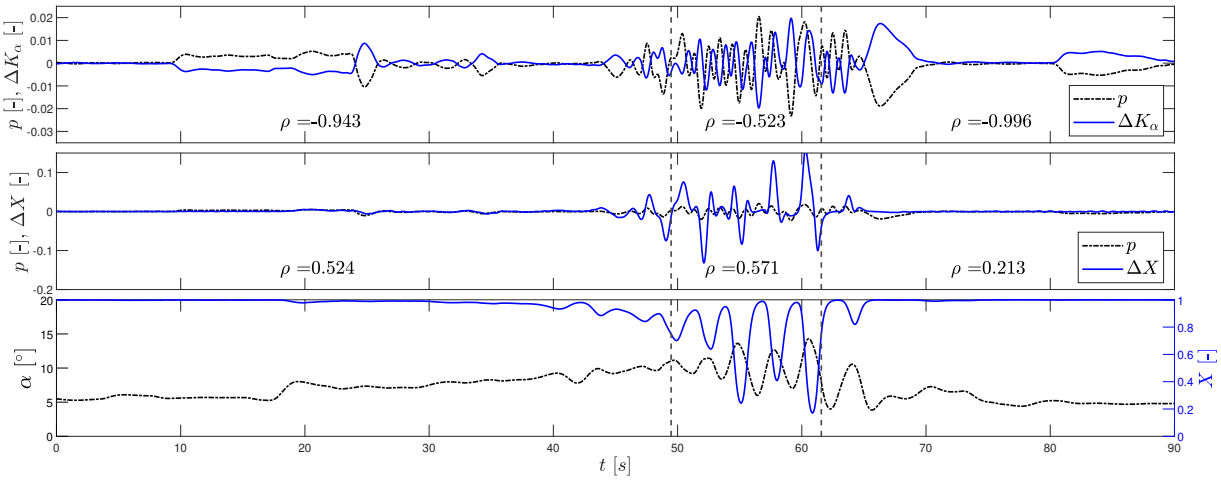


**Fig. 16 A correlation analysis of the asymmetric flow separation regressors (ASYM set 8). The region within the vertical dashed lines is where deep stall is defined. $\rho$ denotes Pearson's linear correlation coefficient evaluated over each region.**

Since the above analysis is dependent on a crude partitioning method, a continuous approach is presented in Figs. 17a and 17b for the pairs ($p$, $\Delta K_\alpha$) and ($p$, $\Delta X$), respectively. The data points are color-coded by the value of $X$ at the given point. A strong linear correlation is visible by a diagonal pattern in the data points. The dependency of correlation on $X$ is evident for the pair ($p$, $\Delta K_\alpha$), by the dark red color on the clearly defined diagonal pattern, and the different color-coding of the points that are located away from this diagonal. The diagonal is much less defined for the pair ($p$, $\Delta X$), although some dependency of $X$ on the correlation is visible.

The analysis described in this section provides an explanation for the model structure selection results. $p$ is generally an important regressor for lateral-directional models. However, for the considered stall maneuvers it is correlated with the asymmetric flow separation regressors, which are more capable of describing the nonlinearities in these models. As

a result, $p$ was omitted from these model structures. The analysis confirms that the amount of correlation of the pair ($p$, $\Delta K_\alpha$) is highly dependent on the amount of flow separation. A similar effect is observed for the pair ($p$, $\Delta X$), to a lesser extent. A possible solution is the introduction of a univariate spline regressor that takes the value of $\Delta K_\alpha$ or $\Delta X$, only when activated in the stall region. This would require a clear definition of the stall region and a method of computing the gradient of this spline term with respect to the model parameters.

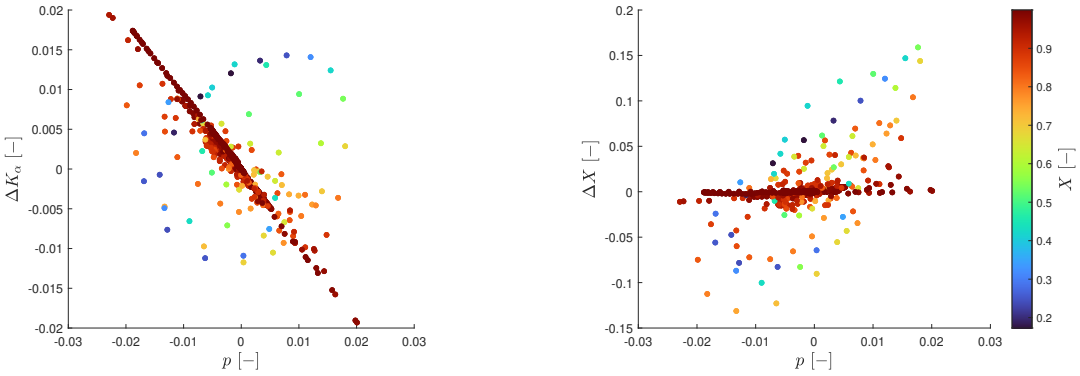


**(a)** $p$ **and** $\Delta K_\alpha$**.** **(b)** $p$ **and** $\Delta X$

**Fig. 17 Correlation plots, color-coded by the value of $X$ (ASYM set 8).**

### B. Performance Comparison with Previous Stall Models

Several aerodynamic models have been developed for this Cessna Citation II aircraft. A numerical performance comparison can be found in Table 10, which presents the validation fit metrics for the proposed model, the baseline stall model [15], and the nominal envelope model [31]. The last-mentioned model does not include specific stall-related dynamics and was identified in the normal flight envelope. It is included in this comparison to evaluate the merit of the current methodologies. The longitudinal model structures of the proposed model and the baseline stall model are equal but feature different $X$-parameter values, and therefore different aerodynamic parameter estimates. The observations are visualized for an example maneuver in Figs. 18a and 18b, for the lateral-directional the longitudinal axes, respectively.

The proposed model showcases the best prediction performance for $C_l$, $C_n$, and $C_Y$. When evaluating the lateral-directional outputs of the baseline stall model on the ASYM data set, the MSE increases with 228%, 207%, and 155% respectively. Refer to Table 10 for all relative differences in MSE and $R^2$ with respect to the proposed model. The proposed methodology of estimating flow separation parameters from the roll moment has proven effective at improving the lateral-directional model fidelity. Conversely, the fidelity of the longitudinal models $C_L$, $C_D$, and $C_m$ worsens with the new $X$-parameters, as the previous model performs greater in terms of MSE and $R^2$. The relative fidelity reduction of the longitudinal models is consistently smaller than the relative improvement of the lateral-directional models. Moreover, the proposed model performs better than the nominal envelope model, in every axis.

**Table 10 Comparison of the proposed model performance with previous Cessna Citation II models. The model fit properties are computed for the 6 validation sets, including the relative difference with the proposed model.**

| | **Proposed Stall Model** | | **Baseline Stall Model** [15] | | **Nominal Envelope Model** [31] | |
|---|---|---|---|---|---|---|
| Model | MSE | $\bar{R^2}$ | MSE | $\bar{R^2}$ | MSE | $\bar{R^2}$ |
| $C_l$ | 1.41E-6 | 0.75 | 3.20E-6 (+228%) | 0.44 (-42%) | 5.21E-5 (+3694%) | -6.24 |
| $C_n$ | 8.50E-7 | 0.68 | 1.80E-6 (+207%) | 0.23 (-67%) | 5.39E-5 (+6345%) | -18.9 |
| $C_Y$ | 5.73E-5 | 0.65 | 8.86E-5 (+155%) | 0.50 (-23%) | 3.57E-3 (+6232%) | -15.2 |
| $C_L$ | 3.51E-3 | 0.78 | 1.45E-3 (-59%) | 0.91 (+16%) | 5.37E-3 (+53%) | 0.64 |
| $C_D$ | 1.10E-4 | 0.67 | 5.78E-5 (-47%) | 0.84 (+25%) | 1.94E-3 (+1745%) | -5.02 |
| $C_m$ | 1.83E-4 | 0.43 | 1.39E-4 (-24%) | 0.62 (+44%) | 1.22E-3 (+667%) | -2.84 |

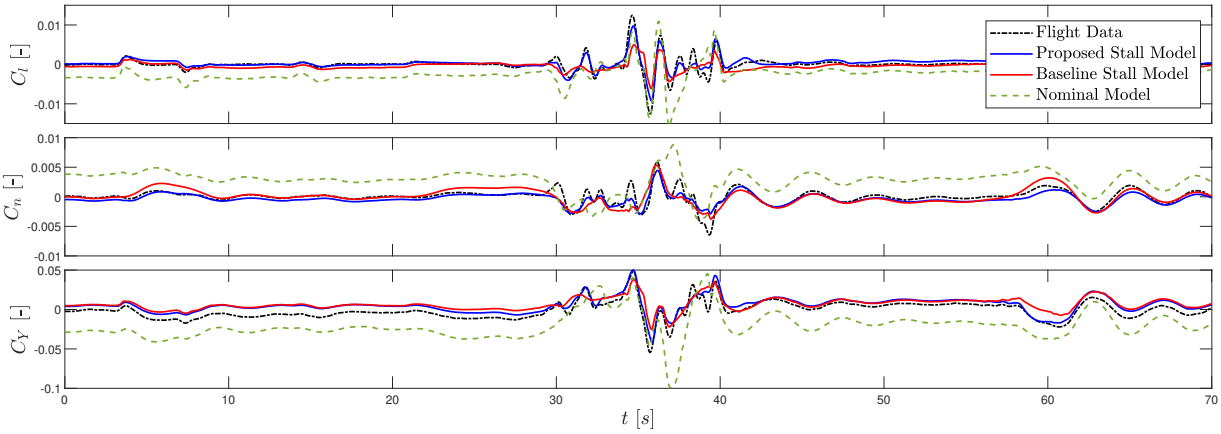


**(a) Asymmetric models.**

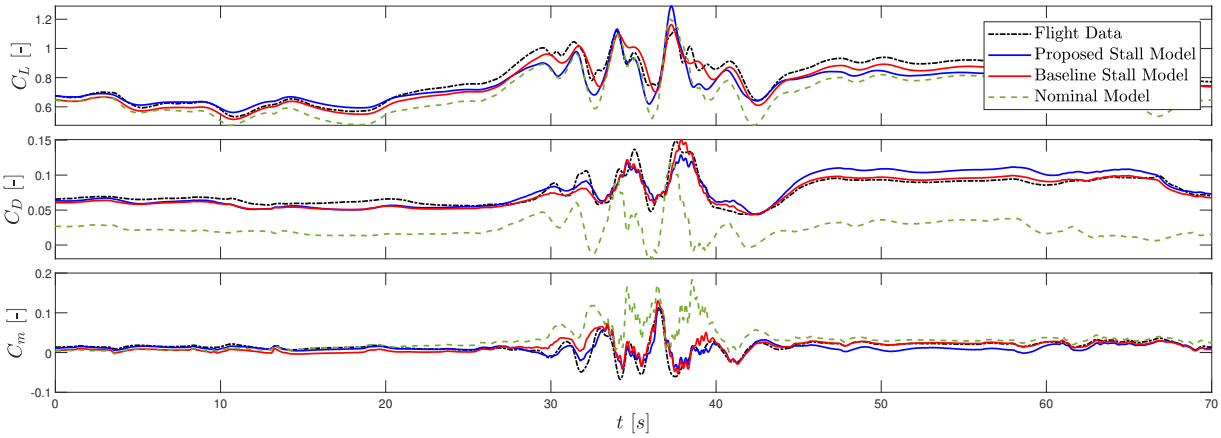


**(b) Symmetric models.**

**Fig. 18 A comparison of the flight data, the proposed stall model output, the baseline stall model [15], and the nominal envelope model [31] (ASYM set 22).**

### C. Remaining Work Towards a Full-Envelope Stall Model

From the results of this research, several recommendations can be made for future flight experiments. The most important design choices of the current flight test data set were the inclusion of only accelerated stalls, a subset of stall maneuvers performed with a sideslip angle, and dynamic aileron and elevator inputs during all stall maneuvers. The most notable benefit of including stall approaches with sideslip is that significant rudder inputs are included in the data, leading to the selection of the rudder deflection in the yaw and lateral force models. The difference between the $X$-parameter estimates of maneuvers with 3-2-1-1 and QR aileron inputs was found to be minimal, for the selected roll moment model structure. Since the 3-2-1-1 inputs can be applied automatically in the laboratory aircraft, it is more reliable and therefore preferred over QR in future experiments.

While an average reduction of aileron effectiveness was identified with the current methodology, this parameter is expected to vary over time. Specifically, the effectiveness is expected to reduce with an increasing amount of flow separation. Such variations were not identified in this research. A likely reason for this result is the current application of dynamic maneuvers. The only aileron inputs in the pre-stall region are the inputs required to reach the accelerated stall bank angle. These inputs are relatively small and do not excite the lateral aircraft dynamics fully, as can be seen in the flight data example of Fig. 19. When a dynamic maneuver such as 3-2-1-1 is included in the stall region, most of the roll moment response is due to the inputs in the stall region. The resulting $C_{l_{\delta_a}}$ estimate is based largely on the response of this region. To better identify the variations of this parameter, future flight tests should include dynamic aileron inputs closely before the stall maneuver. Possibly, $X$ or a transformation thereof provides an effect suitable for describing the variations in $C_{l_{\delta_a}}$.

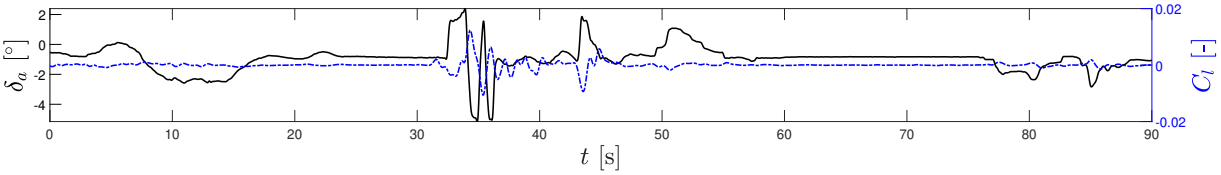


**Fig. 19 An example of a 3-2-1-1 aileron input and the roll moment response (ASYM set 20).**

The discussions in this paper have concluded that the proposed roll moment-based methodology is effective at improving the fidelity of the lateral-directional models, while the previous lift-based approach [15] is more suitable for longitudinal stall modeling. In order to obtain the best of both worlds, a hybrid approach can be applied. In this case, two $X$-parameter sets can be defined: $(\theta_X)_s$ and $(\theta_X)_a$. The symmetric flow separation variable $X$ is computed using $(\theta_X)_s$ and the angle of attack at the C.G., while the asymmetric flow separation variables $X_L$, $X_R$ are computed using $(\theta_X)_a$ and the local angles of attack. This approach would require no additional optimizations, as the models were identified for similar flight conditions, and the lift-based model has shown a good fit on the current validation data set. Using the hybrid approach with $(\theta_X)_s = [0.2547, 0.0176, 27.671, 0.2084]^\top$ [15] and $(\theta_X)_a = [0.0971, 0.5526, 16.865, 0.1730]^\top$ (the estimates of this paper) results in the lateral-directional model fit properties in the first column of Table 10 and the longitudinal properties of the second column.

Finally, to expand the validity of the model, the methodology in this paper should be repeated for other selected altitudes, flaps, and gear configurations. If different parameter estimates are obtained, the parameters can become a function of flight condition, as was done earlier for the nominal flight envelope Citation II model [31]. Note that the model structures and aerodynamic parameter values of the nominal flight envelope model are different from the models discussed in this paper. Some form of blending between the nominal model and the stall model is required to obtain a realistic flight simulation experience. For instance, van Horssen [32] proposed the use of two sigmoid activation functions, facilitating the transition between the models at some range of angle of attack.

## VI. Conclusion

This research set out to improve the lateral-directional model fidelity of the existing Cessna Citation II dynamic stall model. For this purpose, a flight test data set of stall maneuvers was specifically collected to induce asymmetric flow separation effects. The accelerated stall maneuvers included dynamic inputs in 2 axes, and a subset of maneuvers was approached with a reference sideslip angle. Kirchhoff's stall modeling method was modified to include two distinct flow separation variables, each describing the separation development on the respective wing surface. The parameters describing these variables were estimated using the roll moment derived from flight data. An algorithm based on Multivariate Orthogonal Functions was employed to select the structures of the lateral-directional aerodynamic model equations. The longitudinal model structures were taken directly from a baseline stall model. The proposed transformations of the flow separation variables were selected by the algorithm to capture the stall-related nonlinearities of the roll moment, yaw moment, and lateral force. While the flow separation variables were found to be ineffective at describing stall-related variations in roll control authority, the estimated aileron effectiveness parameter is approximately 41% smaller than for the baseline stall model. This result indicates an average reduction of roll control authority over the data set, due to the inclusion of asymmetric stall regressors in the model. The lateral-directional model outputs provide a good fit with the validation flight data set, with an average explained variance of 0.70, and an average improvement of 48% in terms of MSE, compared to the baseline stall model. Conversely, the longitudinal model fit deteriorates with an MSE increase of 88%, and an average explained variance of 0.63. These results indicate that the estimated flow separation parameters are less suitable for longitudinal stall modeling than for lateral-directional stall modeling. Acknowledging this fact, a hybrid Kirchhoff method is proposed, which combines two sets of parameters describing symmetric and asymmetric flow separation separately. In conclusion, the proposed asymmetric stall model identification approach is suitable for identifying asymmetric stall models and provides a method for improving the overall model fidelity. In this context, this research has contributed to the overarching objective of enhancing pilot training in simulators.

# References


[1] Bryan, G., *Stability in Aviation: an Introduction to Dynamical Stability as Applied to the Motion of Aeroplanes*, Macmillan and Company, London, 1911.

[2] Fouda, M., and Taha, H., "Effect of Wing Planform on Airplane Stability and Control Authority in Stall," *AIAA Science and Technology Forum and Exposition, AIAA SciTech Forum 2022 San DIego, CA, USA*, 2022. https://doi.org/10.2514/6.2022-1161.

[3] Nguyen, D., Goman, M., Lowenberg, M., and Neild, S., "Evaluating Unsteady Aerodynamic Effects in Stall Region for a T-Tail Transport Model," *AIAA Science and Technology Forum and Exposition, AIAA SciTech Forum 2022*, American Institute of Aeronautics and Astronautics Inc, AIAA, 2022. https://doi.org/10.2514/6.2022-1932.

[4] Abramov, N., Goman, M., Khrabrov, A., and Soemarwoto, B., "Aerodynamic modeling for poststall flight simulation of a transport airplane," *Journal of Aircraft*, Vol. 56, American Institute of Aeronautics and Astronautics Inc., 2019, pp. 1427–1440. https://doi.org/10.2514/1.C034790.

[5] Lambregts, A. A., Nesemeier, G., Wilborn, J. E., and Newman, R. L., "Airplane upsets: Old problem, new issues," *AIAA Modeling and Simulation Technologies Conference and Exhibit Honolulu, Hawaii, USA*, 2008, pp. 1115–1125. https://doi.org/10.2514/6.2008-6867.

[6] Da Ronch, A., Vallespin, D., Ghoreyshi, M., and Badcock, K. J., "Evaluation of dynamic derivatives using computational fluid dynamics," *AIAA Journal*, Vol. 50, No. 2, 2012, pp. 470–484. https://doi.org/10.2514/1.J051304.

[7] Smaili, M., Soemarwoto, B., Abramov, N., Goman, M., Khrabrov, A., Kolesnikov, E., and Fucke, L., "Pushing Ahead-SUPRA Airplane Model for Upset Recovery," Tech. rep., 2017. URL www.nlr.nl.

[8] Goman, M., and Khrabrov, A., "State-space representation of aerodynamic characteristics of an aircraft at high angles of attack," *Astrodynamics Conference Hilton Head Island, SC, USA*, American Institute of Aeronautics and Astronautics Inc, AIAA, 1992, pp. 759–766. https://doi.org/10.2514/6.1992-4651, URL https://arc.aiaa.org/doi/10.2514/6.1992-4651.

[9] Fischenberg, D., "Identification of an unsteady aerodynamic stall model from flight test data," *20th Atmospheric Flight Mechanics Conference Baltimore, MD, USA*, American Institute of Aeronautics and Astronautics Inc, AIAA, 1995, pp. 138–146. https://doi.org/10.2514/6.1995-3438, URL https://arc.aiaa.org/doi/10.2514/6.1995-3438.

[10] Dias, J., "Unsteady and Post-Stall Model Identification Using Dynamic Stall Maneuvers," *AIAA Atmospheric Flight Mechanics Conference Dallax, TX, USA*, American Institute of Aeronautics and Astronautics (AIAA), 2015. https://doi.org/10.2514/6.2015-2705.

[11] Fischenberg, D., and Jategaonkar, R., "Identification of Aircraft Stall Behavior from Flight Test Data," *RTO SCI Symposium on System Identification for Integrated Aircraft Development and Flight Testing Madrid, Spain*, 1998. https://doi.org/https://doi.org/10.2514/6.1996-3441, URL https://arc.aiaa.org/doi/abs/10.2514/6.1996-3441.

[12] Singh, J., and Jategaonkar, R. V., "Flight determination of configurational effects on aircraft stall behavior," *21st Atmospheric Flight Mechanics Conference San Diego, CA, USA*, Vol. 33, American Institute of Aeronautics and Astronautics, 1996, pp. 657–665. https://doi.org/10.2514/6.1996-3441, URL http://arc.aiaa.org.

[13] Lutze, F., Fan, Y., and Stagg, G., "Multiaxis unsteady aerodynamic characteristics of an aircraft," *24th Atmospheric Flight Mechanics Conference*, American Institute of Aeronautics and Astronautics Inc, AIAA, 1999, pp. 56–64. https://doi.org/10.2514/6.1999-4011.

[14] Van Horssen, L., De Visser, C., and Pool, D., "Aerodynamic Stall and Buffet Modeling for the Cessna Citation II Based on Flight Test Data," *AIAA Modeling and Simulation Technologies Conference*, 2018. https://doi.org/10.2514/6.2018-1167, URL http://arc.aiaa.org.

[15] van Ingen, J., de Visser, C., and Pool, D., "Stall model identification of a cessna citation II from flight test data using orthogonal model structure selection," *AIAA Scitech 2021 Forum Virtual Event*, 2021, pp. 1–29. https://doi.org/10.2514/6.2021-1725, URL https://arc.aiaa.org/doi/10.2514/6.2021-1725.

[16] Morelli, E., Cunningham, K., and Hill, M., "Global Aerodynamic Modeling for Stall/Upset Recovery Training Using Efficient Piloted Flight Test Techniques," *AIAA Modeling and Simulation Technologies (MST) Conference Boston, MA, USA*, 2013. https://doi.org/https://doi.org/10.2514/6.2013-4976, URL https://arc.aiaa.org/doi/10.2514/6.2013-4976.

[17] Koehler, R., and Wilhelm, K., "Auslegung von Eingangssignalen fur die Kennwerter-mittlung," *DFVLR-IB*, 1977, pp. 154–77.

[18] Mulder, M., Lubbers, B., Zaal, P., Van Paassen, M., and Mulder, J., "Aerodynamic Hinge Moment Coefficient Estimation Using Automatic Fly-By-Wire Control Inputs," *AIAA Modeling and Simulation Technologies Conference - Chicago, Illinois*, 2009.

[19] Klein, V., and Morelli, E., *Aircraft System Identification: Theory and Practice*, AIAA, 2006.

[20] Wang, L., Zhao, R., Xu, K., Zhang, Y., and Yue, T., "Identification and Modeling Method of Longitudinal Stall Aerodynamic Parameters of Civil Aircraft Based on Improved Kirchhoff Stall Aerodynamic Model," *Aerospace*, Vol. 10, No. 4, 2023. https://doi.org/10.3390/aerospace10040333.

[21] Greenwell, D., "A review of unsteady aerodynamic modelling for flight dynamics of manoeuvrable aircraft," *Collection of Technical Papers - AIAA Atmospheric Flight Mechanics Conference*, Vol. 2, 2004, pp. 1231–1255. https://doi.org/10.2514/6.2004-5276, URL https://arc.aiaa.org/doi/10.2514/6.2004-5276.

[22] Singh, J., and Jategaonkar, R., "Identification of lateral-directional behavior in stall from flight data," *Journal of Aircraft*, Vol. 33, No. 3, 1995, pp. 627–630. https://doi.org/10.2514/3.46993, URL https://arc.aiaa.org/doi/10.2514/3.46993.

[23] Grauer, J., "Position Corrections for Airspeed and Flow Angle Measurements on Fixed-Wing Aircraft," *NASA TM*, Vol. 219795, 2017. URL http://www.sti.nasa.gov.

[24] Nocedal, J., and Wright, S., *Nocedal, Wright - 2006 - Numerical Optimization (2nd Ed.)*, 2nd ed., 2006.

[25] Norsett, J., Wanner, and Hairer, *Solving Ordinary Differential Equations I*, Springer Berlin Heidelberg, 1993. https://doi.org/10.1007/978-3-540-78862-1.

[26] Morelli, E., "Global nonlinear aerodynamic modeling using multivariate orthogonal functions," *Journal of Aircraft*, Vol. 32, No. 2, 1995, pp. 270–277. https://doi.org/10.2514/3.46712, URL https://arc.aiaa.org/doi/10.2514/3.46712.

[27] Klein, V., Batterson J.G., and Murphy, P., "Determination of Airplane Model Structure from Flight Data by Using Modified Stepwise Regression," *NASA Technical Paper*, Vol. 1916, 1981.

[28] Mulder, J., Van Staveren, W., Van Der Vaart, J., De Weerdt, E., De Visser, C., In 't Veld, A., and Mooij, E., *Lecture Notes AE3202 Flight Dynamics*, Delft University Of Technology, Delft, 2013.

[29] Massey, F., "The Kolmogorov-Smirnov Test for Goodness of Fit," *Journal of the American Statistical Association*, Vol. 46, No. 253, 1951, pp. 68–78. https://doi.org/10.2307/2280095.

[30] Miller, R., *Simultaneous Statistical Inference*, Springer, 1981.

[31] Van Den Hoek, M., De Visser, C., and Pool, D., "Identification of a Cessna Citation II Model Based on Flight Test Data," *4th CEAS Specialist Conference on Guidance, Navigation & Control*, 2017.

[32] van Horssen, L., "Aerodynamic Stall Modeling for the Cessna Citation II," , 2016. URL https://repository.tudelft.nl/islandora/object/uuid%3A7de36b4e-32b5-4da7-836b-c8fa40eb254e.

[33] Leis, J., and Kramer, M., "The Simultaneous Solution and Sensitivity Analysis of Systems Described by Ordinary Differential Equations," Tech. rep., 1988.

# Appendices

## A. Collinearity Analysis of Candidate Regressors

To prepare for the model structure selection, a collinearity analysis is performed within the pool of candidate regressors. If there are extreme correlations between a pair of candidates, it might be beneficial to remove one of the pair from the pool. Since this step is performed before $X$-parameter estimation and considering these parameters change with every iteration of the roll moment model structure selection, they are taken from van Ingen et al. [15]. The correlation matrix is evaluated for every training maneuver set and subsequently averaged.

**Table 11 Correlation matrix of the candidate regressors, averaged over all training maneuver sets.**

| | $p$ | $q$ | $r$ | $\delta_a$ | $\delta_e$ | $\delta_r$ | $\alpha$ | $\dot{\alpha}$ | $\beta$ | $\dot{\beta}$ | $M$ | $C_T$ | $\Delta X \frac{y_w}{b}$ | $\Delta K_\alpha \frac{y_w}{b}$ | $X$ | $1-X$ |
|---|---|---|---|---|---|---|---|---|---|---|---|---|---|---|---|---|
| $p$ | 1.0 | | | | | | | | | | | | | | | |
| $q$ | 0.0 | 1.0 | | | | | | | | | | | | | | |
| $r$ | 0.0 | 0.2 | 1.0 | | | | | | | | | | | | | |
| $\delta_a$ | -0.6 | -0.0 | 0.0 | 1.0 | | | | | | | | | | | | |
| $\delta_e$ | 0.1 | -0.3 | -0.6 | 0.0 | 1.0 | | | | | | | | | | | |
| $\delta_r$ | 0.1 | -0.2 | -0.2 | -0.1 | 0.3 | 1.0 | | | | | | | | | | |
| $\alpha$ | -0.1 | 0.3 | 0.6 | -0.0 | -0.8 | -0.3 | 1.0 | | | | | | | | | |
| $\dot{\alpha}$ | 0.0 | 0.8 | 0.0 | 0.0 | -0.1 | -0.1 | 0.0 | 1.0 | | | | | | | | |
| $\beta$ | 0.2 | 0.1 | 0.3 | -0.3 | -0.1 | -0.4 | 0.1 | 0.1 | 1.0 | | | | | | | |
| $\dot{\beta}$ | 0.3 | -0.0 | -0.4 | -0.3 | 0.0 | 0.0 | -0.1 | 0.0 | 0.0 | 1.0 | | | | | | |
| $M$ | 0.1 | -0.1 | -0.6 | -0.0 | 0.7 | 0.3 | -0.7 | 0.0 | -0.1 | 0.0 | 1.0 | | | | | |
| $C_T$ | 0.1 | -0.1 | -0.5 | 0.0 | 0.5 | 0.2 | -0.6 | 0.0 | -0.1 | 0.0 | 0.5 | 1.0 | | | | |
| $\Delta X \frac{y_w}{b}$ | 0.6 | 0.1 | 0.1 | -0.1 | 0.0 | -0.1 | -0.1 | 0.1 | 0.2 | 0.3 | 0.0 | 0.0 | 1.0 | | | |
| $\Delta K_\alpha \frac{y_w}{b}$ | -0.6 | 0.0 | -0.1 | 0.6 | -0.0 | -0.1 | 0.0 | 0.0 | -0.1 | -0.1 | -0.0 | -0.0 | 0.1 | 1.0 | | |
| $X$ | 0.1 | 0.0 | -0.4 | 0.0 | 0.7 | 0.2 | -0.8 | 0.3 | -0.0 | 0.1 | 0.6 | 0.4 | 0.1 | 0.0 | 1.0 | |
| $1-X$ | -0.1 | -0.0 | 0.4 | -0.0 | -0.7 | -0.2 | 0.8 | -0.3 | 0.0 | -0.1 | -0.6 | -0.4 | -0.1 | -0.0 | -1.0 | 1.0 |

### B. Cost Function Gradient Specification

Obtaining the gradient of the objective function is a non-trivial task. Since the flow separation point is governed by an ODE, the sensitivity cannot be computed directly. The cost function is re-stated for clarity:

$$J(\theta, x) = \frac{1}{N}\left(C_l - \hat{C}_l(\theta, x)\right)^\top \left(C_l - \hat{C}_l(\theta, x)\right) \tag{53}$$

Furthermore, an initial roll moment model is stated for this description. This model includes a term that describes flow separation asymmetry by means of a function $f(X_L, X_R)$.

$$\hat{C}_l = C_{l_0} + C_{l_\beta}\beta + C_{l_p} p + C_{l_r} r + C_{l_{\delta_a}} \delta_a + C_{l_f} f(X_L, X_R) \tag{54}$$

The objective is to find the gradient of the objective function with respect to the parameter vector:

$$\theta_{nl} = \begin{bmatrix} \tau_1 & \tau_2 & a_1 & \alpha^* & C_{l_0} & C_{l_\beta} & C_{l_p} & C_{l_r} & C_{l_{\delta_a}} & C_{l_f} \end{bmatrix}^\top \tag{55}$$

The roll moment model of Eq. (54) is linear in the parameters, making the computation of the gradient with respect to the $C_l$-parameters straightforward. The $X$-parameters are not directly related to the roll moment, but through the ODEs of the local flow separation points:

$$\frac{\mathrm{d}}{\mathrm{d}t} X_w(t, x, \theta_X) = \frac{1}{\tau_1}\left(-X_w + \frac{1}{2} - \frac{1}{2}\tanh\left[a_1\left(\alpha_w - \tau_2 \dot{\alpha_w} - \alpha^*\right)\right]\right) \quad \text{for} \quad w \in \{L, R\} \tag{56}$$

where $x$ denotes the aircraft state. Note that the assumption of a single set of $X$-parameters is maintained in this derivation. The chain rule is applied to obtain the full gradient formulation:

$$\frac{\partial J(\theta_{nl}, x)}{\partial (\theta_{nl})_i} = \begin{cases} \frac{\partial J}{\partial \hat{C}_l}\frac{\partial \hat{C}_l}{\partial X_L}\frac{\partial X_L}{\partial \theta_i} + \frac{\partial J}{\partial \hat{C}_l}\frac{\partial \hat{C}_l}{\partial X_R}\frac{\partial X_R}{\partial \theta_i} & \text{with } (\theta_{nl})_i \in \{\tau_1\ \tau_2\ a_1\ \alpha^*\} \\ \frac{\partial J}{\partial \hat{C}_l}\frac{\partial \hat{C}_l}{\partial \theta_i} & \text{with } (\theta_{nl})_i \in \left\{C_{l_0}\ C_{l_\beta}\ C_{l_p}\ C_{l_r}\ C_{l_{\delta_a}}\ C_{l_f}\right\} \end{cases} \tag{57}$$

Obtaining the sensitivity of the flow separation points to its parameters $\frac{\partial X_L}{\partial \theta_i}$ and $\frac{\partial X_R}{\partial \theta_i}$ is the most challenging step. A method is used that evaluates the gradient numerically and solves the ODE simultaneously, as described by [33]. The previous stall model successfully applied this method for a lift-based formulation [15].

Firstly, the partial derivative of the model with respect to the flow separation variables is written:

$$\frac{\partial \hat{C}_l}{\partial X_w} = C_{l_f} \frac{\partial f}{\partial X_w} \quad \text{for} \quad w \in \{L, R\} \tag{58}$$

The flow separation ODEs of Eq. (56) are rewritten:

$$\frac{\mathrm{d}X_w(t, x, \theta_X)}{\mathrm{d}t} = G_w(X_w, t, x, \theta_X) \quad \text{for} \quad w \in \{L, R\} \tag{59}$$

and the partial derivatives to be obtained are written as follows:

$$\frac{\partial X_w(t, x, \theta_X)}{\partial \theta_X} = S_w(t, x, \theta_X) \quad \text{for} \quad w \in \{L, R\} \tag{60}$$

The partial derivatives of Eq. (59) with respect to $\theta_X$ are taken to get the result:

$$\frac{\partial}{\partial \theta_X} \frac{\mathrm{d}}{\mathrm{d}t} X_w(t, x, \theta_X) = \frac{\partial G_w(X_w, t, x, \theta_X)}{\partial X_w} \frac{\partial X_w(t, x, \theta_X)}{\partial \theta_X} + \frac{\partial G_w(X_w, t, x, \theta_X)}{\partial \theta_X} \quad \text{for} \quad w \in \{L, R\} \tag{61}$$

Finally, Eq. (60) is substituted to obtain an additional ODE:

$$\frac{\mathrm{d}}{\mathrm{d}t} S_w(t, x, \theta_X) = \frac{\partial G_w(X_w, t, x, \theta_X)}{\partial X} S_w(t, x, \theta_X) + \frac{\partial G_w(X_w, t, x, \theta_X)}{\partial \theta_X} \quad \text{for} \quad w \in \{L, R\} \tag{62}$$

where the initial conditions are $S_w(0, x, \theta_X) = \mathbf{0}$. These ODEs are solved numerically for $S_w(t, x, \theta_X)$ to complete the gradient computation of Eq. (57). Note that the solution to the ODE is the only numerical computation step in this description. Hence, the semi-analytical gradient computation is concluded.

### C. Parameter Convergence of Nonlinear Optimization

Fig. 20 presents the convergence behavior of the nonlinear optimization, including a marker with the final estimate. Note that the $C_l$-parameters clearly converge to a single estimate with the lowest objective function value. The $X$-parameters also converge, but the estimates cover a larger part of the solution space. This result further motivates the choice to repeat the optimization at different initial conditions.

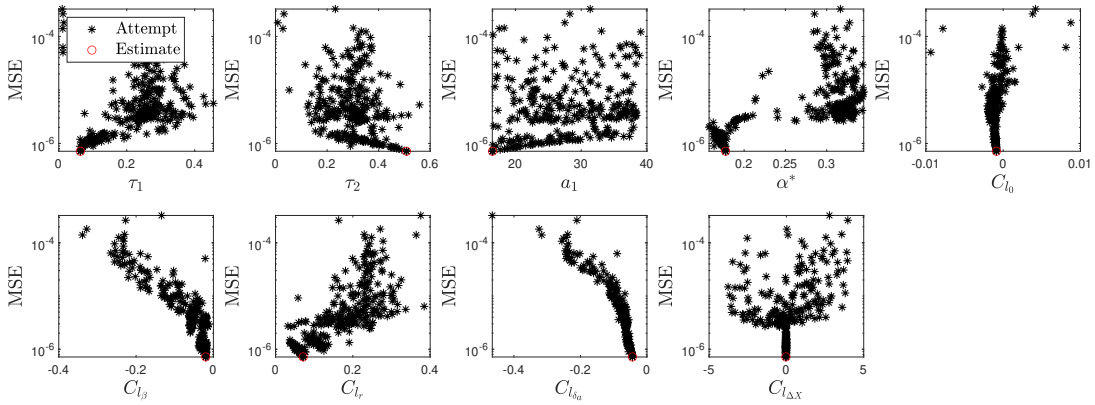


**Fig. 20 Parameter convergence of the final nonlinear optimization, with 300 repetitions (ASYM set 17).**

# Part III

## Preliminary Thesis Report

*This part has been assessed for the course AE4020 Literature Study.

# 1

# A Literature Review Of Stall Model Identification

The concept of aircraft stall has been researched extensively over the previous century. Some of the more recent efforts address the problem of stall model identification from flight data specifically, whereas earlier efforts were generally focused on identifying the stall characteristics for aircraft design purposes. This chapter starts by describing the aerodynamics behind aircraft stall. Subsequently, a timeline of the relevant developments in stall modeling is presented. The most recent and most promising developments for the current application use an approach based on Kirchhoff's flow separation theory. This method and its adaptations are introduced separately. Finally, special attention is paid to modeling the effect of aircraft stall on control surface effectiveness.

## 1.1. The Aerodynamic Stall Phenomenon

This chapter aims to introduce and identify the aerodynamic characteristics of the stall condition. A definition of the phenomenon is presented, and special attention is paid to the type of stall progression. Finally, the regulations and requirements concerning stall modeling are discussed.

### 1.1.1. Aerodynamic Definitions

The lift curve of Figure 1.1 illustrates the typical process of the section lift-coefficient $C_l$ variation with angle of attack (AOA, $\alpha$). Due to the camber of this specific airfoil lift is generated even for some negative values of $\alpha$. $C_l$ increases linearly up until the critical AOA, or stall AOA. The critical AOA depends on wing geometry and airfoil shape. Furthermore, the induced drag increases quadratically with the lift coefficient.

The aerodynamic stall phenomenon occurs when the airflow over the main wing of an aircraft starts separating from the wing surface. The behavior of an aircraft in stall conditions is characterized as highly nonlinear, unsteady, unpredictable, and configuration-dependent. The most notable consequences of this phenomenon are a precipitous decrease in lift and a large increase in drag [14].

The flow separation occurs due to viscous effects. Viscous flow is a widely researched topic that can be described as follows: "a flow where the effects of viscosity, thermal conduction, and mass diffusion are important" [14]. Mass diffusion is only relevant for a gas with gradients in its chemical species and it is deemed irrelevant for the application of airflow over an airfoil.

The influence of friction between the surface and the fluid adjacent to the surface acts to create a force that retards the relative motion. The surface experiences a force in the direction of the flow, tangential to the surface. The flow velocity at the surface is zero and it increases with the distance normal to the surface: a velocity profile is formed. This process is visualized in Figure 1.2.

Another effect of viscosity is an adverse pressure gradient. If flow elements must work their way through increasing pressure, the flow that is retarded by friction could potentially decelerate so much that it reverses its direction, as visually represented by Figure 1.3. The consequence of the reversed flow phenomenon is that the flow separates from the surface and a large wake of recirculating flow is created downstream of the surface, thereby increasing the drag and decreasing the lift. The flow separation point on the surface is located at the point where $\frac{\delta V}{\delta n} = 0$ at the surface, where $V$ denotes the flow velocity and $n$ represents the coordinate normal to the surface [14].

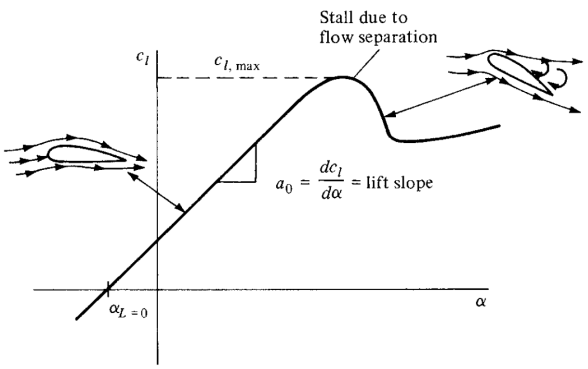


**Figure 1.1:** A schematic of lift-coefficient variation with AOA for a typical section. Adopted from [14].

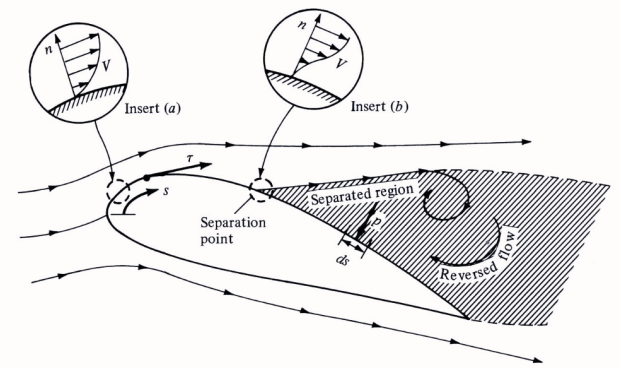


**Figure 1.2:** An illustration of the flow separation process. Adopted from [14].

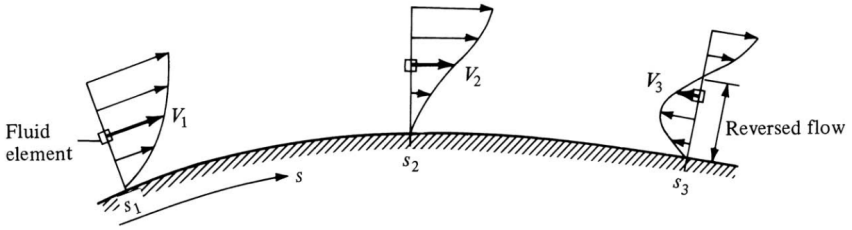


**Figure 1.3:** An illustration of the flow reversal phenomenon. Adopted from [14].

### 1.1.2. Stall Progression

The manner in which the flow separation progresses over the wing can be described in chordwise direction and spanwise direction. The former is dependent on the airfoil geometry and the latter depends on the wing planform.

Stall of an airfoil can progress in several different ways. Three different types of airfoil sections correspond to the section lift curves of Figure 1.4.

The *trailing edge stall* is characteristic of thicker airfoil sections. The turbulent separation starts at the trailing edge, and moves progressively and gradually forward with increasing AOA. The lift curve has a rounded peak and therefore lift loss is not abrupt. In the remainder of this thesis, a trailing edge stall progression is assumed.

The *Leading edge stall* is described as an abrupt separation of the flow near the leading edge of the airfoil, often without reattachment. This type of stall behavior generally occurs on airfoils of symmetrical sections with moderate thicknesses. The peak of the lift curve is sharp. The maximum section coefficient $C_{l_{max}}$ is, therefore, larger than that of airfoils with trailing-edge stall behavior.

Finally, the *thin-airfoil stall* consists of partial separation of the flow starting at the leading edge, and reattachment occurs further downstream: a separation bubble is formed near the leading edge region. The reattachment point moves progressively rearward with an increasing AOA. Figure 1.4 shows the extreme case of a flat plate, but realistically this type of stall progression occurs on sharp-edged airfoils and thin airfoils with a rounded leading edge.

The lateral progression of flow separation is largely dependent on the wing planform design. Recently, a study has researched the effect of the wing planform on the stall progression and the rolling control authority, where five aircraft models with different wing planforms were used for wind tunnel testing at high angles of attack [15]. For rectangular and slightly tapered wing planforms the stall was found to start on the inboard wing sections. Conversely, delta and hybrid wing planforms start stalling at the outboard wing sections. For the cropped elliptical wing, the stall starts at the fuselage, but sufficiently away from the tip sections to initially effect the ailerons.

Since this research concerns system identification of the Cessna Citation II aircraft with a sufficiently thick airfoil, only trailing edge stall is considered relevant. Furthermore, this aircraft has a moderate taper ratio, which would indicate inboard-to-outboard span-wise stall progression.

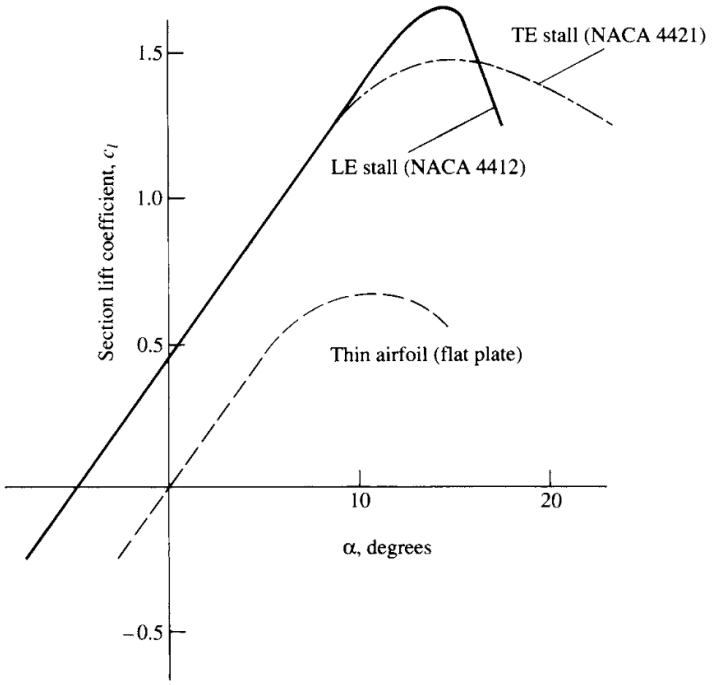


**Figure 1.4:** The section lift curve for trailing-edge (TE) stall, leading-edge (LE) stall and thin airfoil stall. Adopted from [14].

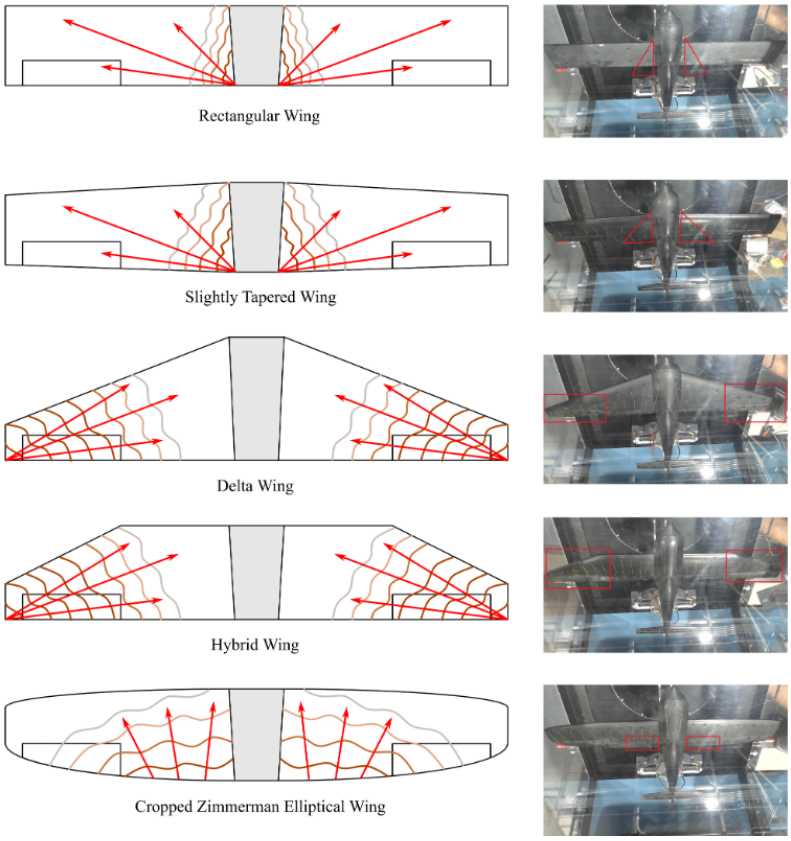


**Figure 1.5:** Lateral stall progression for five different wing planforms. Adopted from [15].

### 1.1.3. Modeling Regulations and Requirements

The International Civil Aviation Organization (ICAO) and the Commercial Aviation Safety Team (CAST) jointly chartered the CAST/ICAO Common Taxonomy Team (CICTT). The objective is to classify accidents and incidents at a high level to permit analysis of the data in support of safety initiatives [2].

Figure 1.6 presents the fatalities by CICTT's Aviation Occurrence Categories of the period 2008 through 2017. The largest contributor to fatal flight accidents is clearly Loss of Control - In Flight (LOC-I). This includes stall-related occurrences [1].

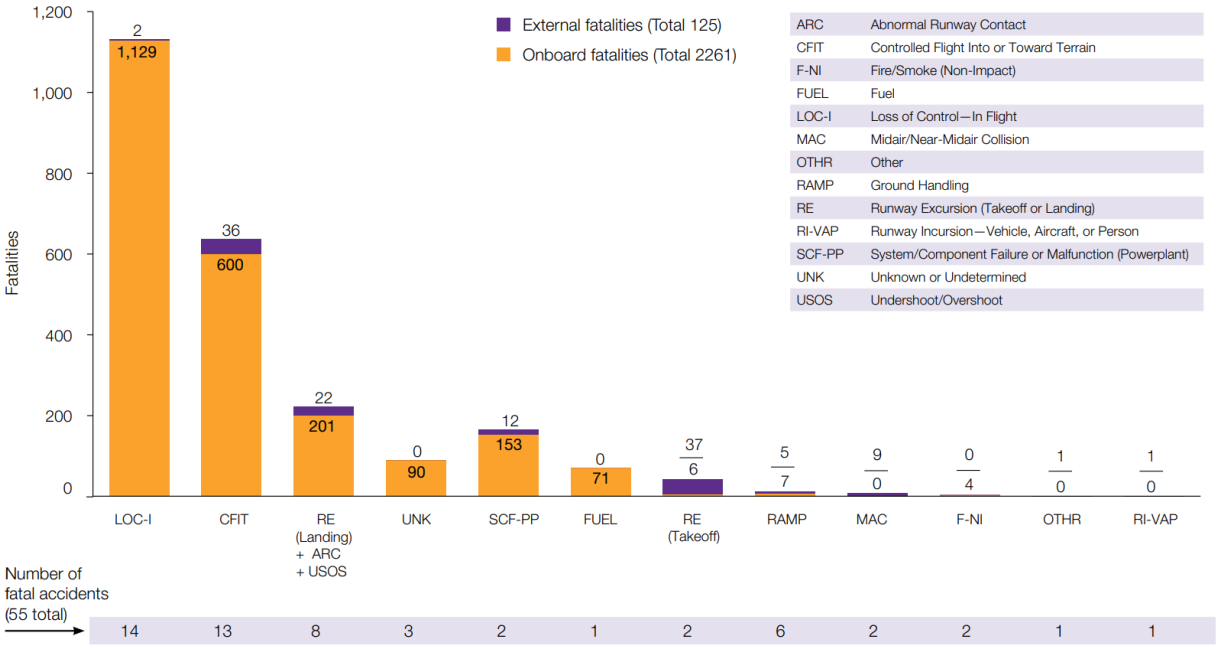


**Figure 1.6:** Fatalities by CICTT Aviation Occurrence Categories of the period 2008 through 2017. Adopted from [1].

Reaching an upset condition during flight does not necessarily imply that an accident is inevitable. Upset recovery is indeed possible to achieve. From 1999 through 2008, for 16 out of 22 LOC-I accidents the primary causal factor was categorized as pilot- or human-induced. Moreover, in all 22 cases, pilots were a contributing causal factor [16].

An obvious solution to this problem is improving the upset recovery training for pilots. The Federal Aviation Administration (FAA) imposed that from 2019 onwards, all civil aviation pilots require training on recognizing, preventing, and recovering aerodynamic stall [3].

These upset training procedures are difficult to perform in actual aircraft, due to cost and safety considerations. Therefore, a good alternative for this purpose is the usage of Flight Simulation Training Devices (FSTDs). In general terms, the model fidelity of the current FSTDs are limited for stall conditions. This could limit the effectiveness of the upset training. This issue is addressed by the FAA by extending the FSTD qualification requirements.

The International Committee for Aviation Training in Extended Envelopes (ICATEE) identified a set of key characteristics that must be represented in a successful stall and post-stall flight model [4].

- Degradation of static and dynamic lateral-directional stability.
- Degradation of control surface effectiveness.
- Uncommanded lateral-directional response.
- Apparent randomness or non-repeatability.
- Changes in pitch stability.
- Mach effects.
- Buffeting.
- Unsteady effects.

**Degradation in static and dynamic lateral-directional stability** Aerodynamic stall has an adverse effect on lateral-directional stability. The lateral stability dictates the response of an aircraft about its roll axis to static or dynamic disturbances. The rolling moment due to sideslip $C_{l_\beta}$ (the effective dihedral) is a primary lateral stability derivative. To obtain desirable lateral control characteristics it is required that its value is negative [17]. A positive sideslip angle means that the nose of the aircraft is rotated to the right with respect to the free stream. The interaction of the wing and the fuselage increases the local AOA on the right wing. Note that for lateral static stability the increase in AOA must result in an increase in lift on that wing, in order to generate a negative rolling moment. This condition $C_{L_\alpha} > 0$ is only true up to the stall AOA. A similar reasoning can be applied to the dynamic lateral stability. During a rolling motion the descending wing experiences an increased local AOA. A negative lift slope results in reduced lift for the descending wing, which yields a positive roll damping $C_{l_p}$.

Directional static stability is described by the condition $C_{n_\beta} > 0$: the aircraft must yaw to the right when subjected to a positive sideslip. The main contributors to static directional stability are the fuselage and the vertical tail, which have a destabilizing and a stabilizing effect, respectively. The effect of the vertical tail can be reduced severely when it is inside the low-energy wake of a stalled wing. A similar effect can be attributed to the dynamic directional stability: the yaw damping $C_{n_r}$ can become ineffective.

**Degradation of control surface effectiveness** The turbulent wake originating from flow separation can reduce the effectiveness of any control surfaces it interacts with. It is also possible that the flow on the control surfaces themselves separates, leading to a stalled control surface. The degradation can be described through the example of the aileron. When deflecting the aileron to incur a rolling motion to the left, the local AOA of the left wing will increase. If the lift slope at the aileron is negative this could cause the opposite of the intended effect: the left wing loses lift due to stall and descends, leading to a further rolling motion to the left.

Similarly, the horizontal and vertical tail can be affected by the turbulent wake of the stalled wing, potentially leading to reduced rudder and elevator effectiveness, respectively.

**Uncommanded lateral-directional response** In reality, it is anticipated that the two wings may not stall exactly simultaneously. Several reasons can exist for this phenomenon. Some examples are small geometry asymmetries, propellers rotating in the same direction and turbulence. When such an asymmetric stall occurs, one wing loses significant lift before the other, resulting in a rolling motion. As discussed before, since the descending wing has a larger local AOA, it could further lose lift, depending on the value of the lift slope. Significant control deflection could be required to counter this rolling motion.

Note that asymmetric stall also produces an asymmetric distribution of drag, leading to a yawing moment. The lateral-directional coupling of the aircraft dynamics implies that this could further increase the uncommanded rolling motion.

Several types of uncommanded lateral-directional motions have been identified at transonic speed by fighter-type aircraft. These motions are commonly described as heavy wing, wing drop, and wing rock. The Abrupt Wing Stall (AWS) Program, a joint program by the National Aeronautics and Space Administration (NASA), the US Navy and Air Force, was initiated to research experiences of unexpected, severe wing-drop motions were encountered by pre-production aircraft, specifically at transonic conditions. The phenomena are described by Figure 1.7.

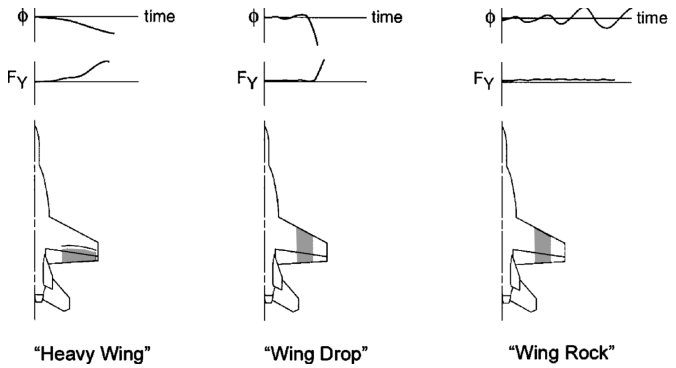


**Figure 1.7:** A description of the different uncommanded lateral motions. Adopted from [18].

**Apparent randomness or non-repeatability.** Small disturbances can grow quickly during stall, due to the highly nonlinear aerodynamics. An example of such a random disturbance is atmospheric turbulence. In general, an exact prediction of the airflow is too complex to be feasible. In this research, randomness is not accounted for in the stall model.

**Changes in pitch stability** For some aircraft configurations a significant pitch-up moment occurs due to entering a stall. Primarily swept wings can lead to this behavior, due to span-wise flow of the boundary layer and upwash at the tips, which encourage separation from the tip [19]. This moves the center of lift forward. The pitch-up moment can become uncontrollable due to the instability. This problem can be solved by limiting the span-wise flow through wing fences. Furthermore, the AOA near the tip can be reduced through wing twist, delaying stall at the tip. Finally, increasing the aspect ratio reduces the change in aerodynamic center.

Another reason for pitch-up instability is the effect of the turbulent wing wake on the tail. The wake from a wing in conventional flight conditions reduces the effective AOA at the tail due to downwash, reducing tail effectiveness. There is a loss of dynamic pressure when the tail enters the wake of a stalled wing. This behavior is especially characteristic of T-tail aircraft. It can potentially lead to a second stable trim point at a very high AOA. Since the elevator effectiveness is already reduced, the control authority could be insufficient to exit the stall [19].

**Mach effects** Mach number is one of the fundamental properties on which the stall characteristics depend. The flow field around the wing changes due to compressibility effects. Moreover, local supersonic flows may occur at airspeeds in the high subsonic range. This occurrence could drastically alter the aircraft stall behavior, due to the creation of shock waves.

As aircraft reach high speeds, the aerodynamic coefficients become a function of Mach number. For the purpose of stall model identification, previous research suggests partitioning flight data based on Mach intervals and determining a different set of coefficients for each interval [8].

**Buffeting** A relatively strong vibration can be felt before an aircraft stall. This phenomenon is commonly referred to as the aerodynamic stall buffet. It is caused by the turbulent flow that is created due to flow separation on the wings. For pilots it is an important cue of an impending stall [20]. Recent research has demonstrated the power of decoupling the low frequency aerodynamic effects and the high frequency aerodynamic effects [13] [13]. In this approach, the low-frequency changes to aerodynamic characteristics are modeled by the well-known model structure based on Kirchhoff's flow separation theory. The model is then augmented with a high-frequency stall buffet model identified based on spectral analysis of the flight test linear acceleration data.

**Unsteady Effects** Flow separation on a wing is not an instantaneous process and is therefore subject to dynamics. Dynamic wind tunnel tests and evaluation of flight test data from highly maneuvrable aircraft have previously demonstrated the lift dependency on not just the AOA, but also its rate $\dot{\alpha}$ and the motion prehistory [21]. Stall modeling research has demonstrated the improvement in model fidelity that follows from including unsteady effects in the model structure [5]. However, care must be taken in selecting terms to avoid high correlations. For instance, $\dot{\alpha}$ and the pitch rate $q$ can have strong correlations. This could lead to ambiguous parameter estimates, as both terms are describing the same phenomena.

## 1.2. A Stall Modeling Timeline

Over the second half of the previous century and the beginning of the current one, an increasing amount of research has been done with the purpose of creating a stall model. This section presents a clear timeline of the progressions in this field.

The research of stall characteristics initially concerned fighter-type aircraft. The first work was mostly concerned with lateral-directional stability, as this was the most critical for the flight safety of newly designed aircraft. Near the end of the 1950s, NASA set out to provide some basic information on the stability and control characteristics in the high AOA range [22]. Results indicated that the chosen configuration became directionally unstable, but maintained positive effective dihedral, control effectiveness and damping in roll and yaw over high AOA ranges. A decade later, a similar analysis of lateral-directional stability characteristics was done by the US Air Force [23]. The experiments consisted of static wind-tunnel tests

and tuft-flow visualization tests. The results indicated that the directional instability was the result of a simultaneous loss of directional stability and effective dihedral at high angles of attack.

In the 1970s more research was done on the lateral-directional effects of the stall condition. For instance, a theoretical investigation resulted in strong indications that the effects of $\dot{\beta}$ derivatives should be considered in attempts to extract lateral-directional parameters at high angles of attack [24]. The accumulation of research on lateral-directional effects led to a broad overview of aerodynamic characteristics at high angles of attack, including possible design choices [19]. This is also the period in which the first efforts of aerodynamic stall modeling from flight data were created, yielding results that demonstrated the feasibility and applicability of the identification approach, to obtain meaningful results [25]. An important note to this study is that insufficient flight data was recorded for the extraction of accurate coefficients. Furthermore, the importance of strong aircraft excitation was emphasized. Similar conclusions were drawn by NASA in a research with a scaled-down F-15 model [26].

In the 1980s, analysis of stall behavior of general aviation aircraft started. Firstly, a review was presented of aerodynamic phenomena that are associated with flight at high AOA [27]. A particular emphasis was put on asymmetric forebody vortices, the oscillatory motion of such vortices, and their relation with the motion of the aircraft. This paper advocated for the development of adequate mathematical models and wind tunnel techniques.

A summary of stall and spin characteristics was published by NASA [28], and the estimation of nonlinear aerodynamic coefficients was described for a sailplane [29]. A novel part of the last-mentioned is the usage of a quaternion-based mathematical model. Moreover, the approach consisted of partitioning flight data in terms of AOA and sideslip, and then fitting a conventional polynomial model to each partition. A similar approach was detailed in [30]. Many stall modeling efforts after this point in time are based on Kirchhoff's flow separation theory. This concept and its applications are discussed separately.

## 1.3. Kirchhoff's Flow Separation Theory

Aircraft stall occurs through flow separation over the wing. This aerodynamic phenomenon can be recognized by a reduction of the lift slope. In the post-stall region a total reduction of the wing lift occurs. Within this range of AOA, the airfoil lift can no longer be described solely as a function of $\alpha$, but unsteady effects are of substantial influence. In the 1990s a relatively simple mathematical model structure was proposed for modeling these nonlinear and dynamic phenomena. The main contribution was the consideration of utilizing coordinates of separation points or vortex breakdown as internal state-space variables [31] [32].

### 1.3.1. Flow Separation Lift Model

The given model structure is valid for airfoils that exhibit trailing edge separation, which requires is to be have sufficient thickness. A non-dimensional coordinate variable $X \in [0, 1]$ is introduced, which presents the position of the separation point on the upper surface of the airfoil. Fully attached flow yields $X = 1$, whereas fully separated flow corresponds to $X = 0$. An assumption is made that separated flow about the airfoil is modeled by Kirchhoff's theory of flow separation, which describes the nonlinear relationship between the lift coefficient and the separation point:

$$C_L = C_{L_\alpha} \left( \frac{1 + \sqrt{X}}{2} \right)^2 \alpha \tag{1.1}$$

Unsteady aerodynamics describe the response of aerodynamic forces and moments to a change in flow condition. Such a change in flow condition could be caused by turbulence or a rapid change in AOA.

The steady-state flow separation point is denoted by $X_0$ and describes the flow separation point under steady flow conditions. A positive AOA rate delays the flow separation point to higher angles of attack. Based on experimental data the movement of the flow separation point in unsteady conditions can be described by Eq. (1.2) [32] [5].

$$\begin{aligned} \tau_1 \frac{dX}{dt} + X &= X_0(\alpha - \tau_2 \dot{\alpha}) \\ \frac{dX}{dt} &= f(t, X, \alpha, \dot{\alpha}) \end{aligned} \tag{1.2}$$

where $\tau_1$ and $\tau_2$ are time constants that describe the unsteady effects in terms of transient effects and hysteresis, respectively. Hysteresis can be described as a phenomenon in which a system's behavior is

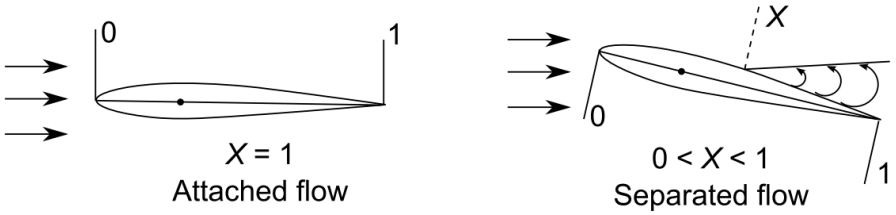


**Figure 1.8:** Illustration of the internal variable X: a non-dimensional coordinate variable representing the position of the separation point on the upper surface of the airfoil. Adopted from [8].

not solely determined by the system's instantaneous state, but also by the system's state history [33].

Furthermore, $a_1$ determines the abruptness of the transition from conventional flight envelope to stalled condition. Finally, $\alpha^*$ schedules the AOA at which stall occurs. It can be shown that at $\alpha = \alpha^*$, the flow is separated up to the halfway point: $X = 0.5$.

The steady flow separation point is in itself a nonlinear function of the AOA and depends on the airfoil and configuration. It can be determined statically through wind tunnel testing. Instead, an approximation can be used [5]:

$$X_0 = \frac{1}{2}\{1 - \tanh(a_1(\alpha - \alpha^*))\} \tag{1.3}$$

This approximation is especially useful for identification purposes, as only $a_1$ and $\alpha^*$ need to be determined and tanh is a continuous function on its entire range. Combining Eq. (1.2) and Eq. (1.3) yields the function that describes the parameter estimation problem.

$$\tau_1 \frac{dX}{dt} + X = \frac{1}{2}\left\{1 - \tanh\left(a_1\left(\alpha - \tau_2\dot{\alpha} - \alpha^*\right)\right)\right\} \tag{1.4}$$

From Eq. (1.4) it is clear that estimating the $X$-parameters is a nonlinear optimization problem. While it is advantageous that the model describe the unsteady and nonlinear relation between lift and AOA using only 4 parameters, obtaining a set of globally optimal parameters is not guaranteed. Furthermore, nonlinear optimization methods are computationally more expensive than linear ones. Several options of algorithms are available for this purpose, which are discussed in Section 5.2.4. If such an algorithm converges to proper estimates the value of the flow separation point $X$ can be determined.

### 1.3.2. Effects of the Flow Separation Parameters

The four parameters that describe the nonlinear behavior of an aircraft stall ($\tau_1$, $\tau_2$, $a_1$, $\alpha^*$) are henceforth referred to as the *$X$-parameters*. The effect of varying the $X$-parameters on the progression and the flow separation are presented in Figure 1.9 through Figure 1.16.

A clear shaping effect can be identified by varying the static parameter $a_1$ in Figure 1.9 and Figure 1.10. For larger values of $a_1$ the flow separation occurs more abruptly, leading to a more abrupt reduction in lift.

$\alpha^*$ schedules the AOA at which flow separation occurs. Note that an increase in this parameter yields an increase in the maximum lift coefficient of the airfoil. Therefore $\alpha^*$ is a direct measure of stall performance of an arfoil.

The effect of $\tau_1$ can best be described as a transient effect that results in a delay of reaching the maximum lift coefficient. $\tau_2$ describes the aerodynamic hysteresis phenomenon. It describes the lagging effect of the AOA rate on the flow separation progression.

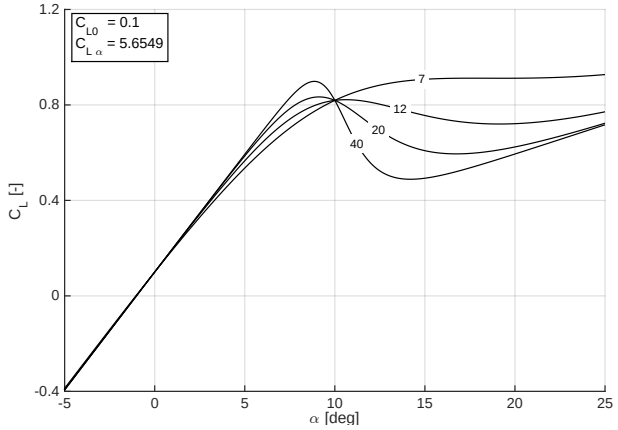


**Figure 1.9:** The effect of varying $a_1$ on the lift coefficient. Reproduced from [9].

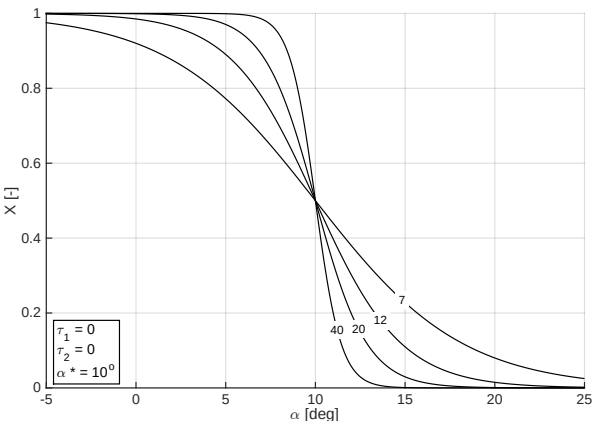


**Figure 1.10:** The effect of varying $a_1$ on the flow separation. Reproduced from [9].

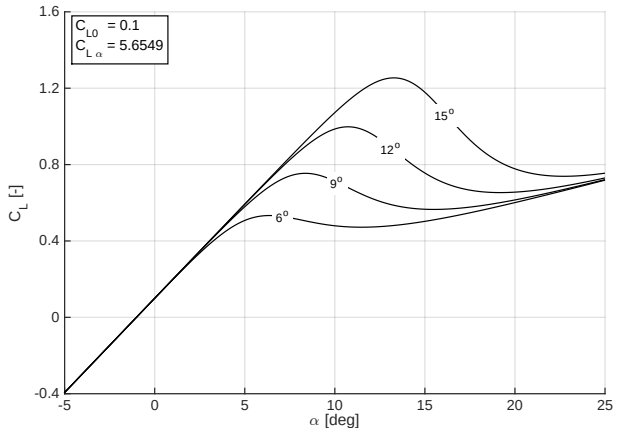


**Figure 1.11:** The effect of varying $\alpha^*$ on the lift coefficient. Reproduced from [9].

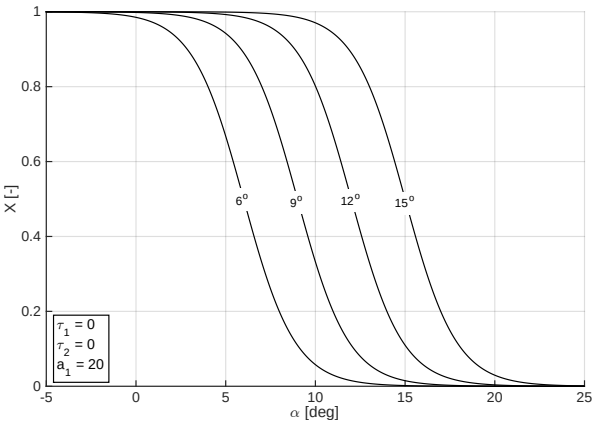


**Figure 1.12:** The effect of varying $\alpha^*$ on the flow separation. Reproduced from [9].

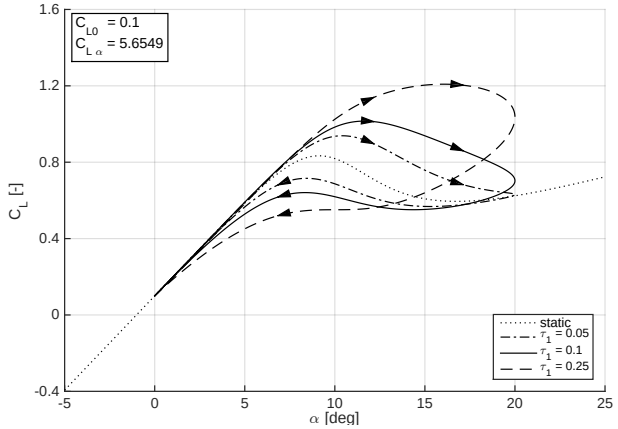


**Figure 1.13:** The effect of varying $\tau_1$ on the lift coefficient. Reproduced from [9].

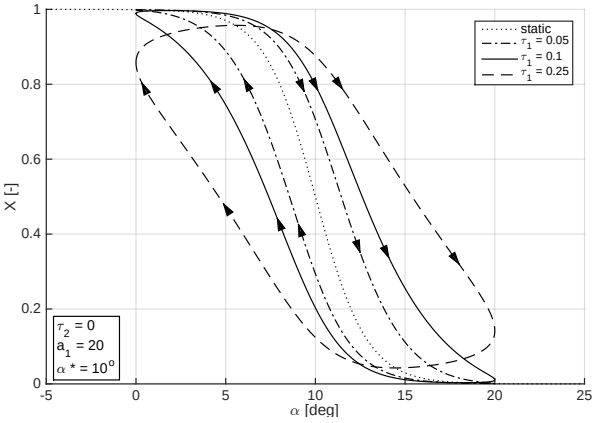


**Figure 1.14:** The effect of varying $\tau_1$ on the flow separation. Reproduced from [9].

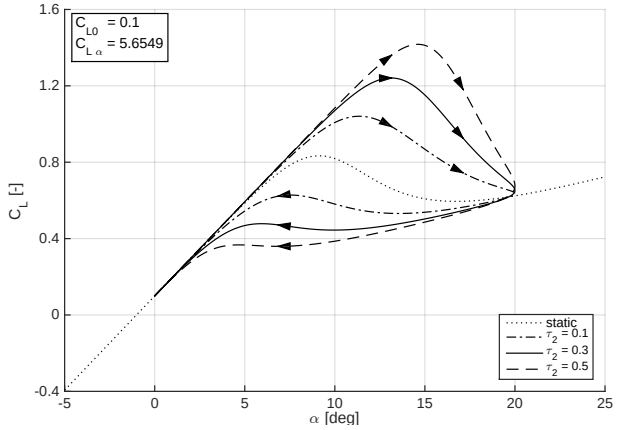


**Figure 1.15:** The effect of varying $\tau_2$ on the lift coefficient. Reproduced from [9].

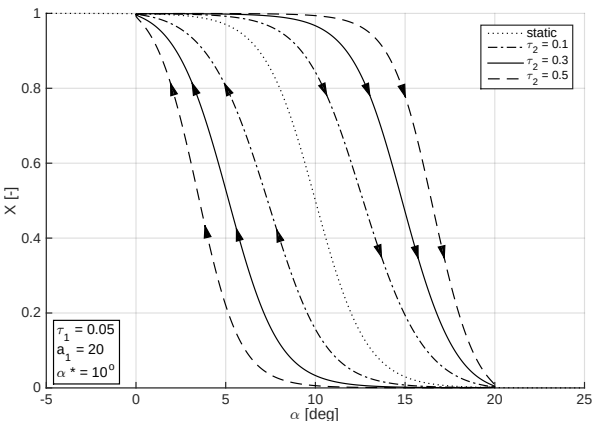


**Figure 1.16:** The effect of varying $\tau_2$ on the flow separation. Reproduced from [9].

### 1.3.3. Longitudinal Stall Model

The lift model of Eq. (1.1) is valid for a symmetrical airfoil. Extending this formulation to a complete aircraft requires the addition of derivatives related to elevator deflection $\delta_e$, pitch rate $q$, and rate of change of AOA $\dot{\alpha}$ [8]. Furthermore, the literature suggests the following longitudinal model structure for the lift, drag, and pitching moment coefficients [13] [5]:

$$C_L = C_{L_\alpha} \left( \frac{1+\sqrt{X}}{2} \right)^2 \alpha + C_{L_q} \frac{q\bar{c}}{V} + C_{L_{\delta_e}} \delta_e \tag{1.5}$$

$$C_D = C_{D_0} + \frac{1}{e\pi\Lambda} C_L^2 + C_{D_X}(1-X) \tag{1.6}$$

$$C_m = C_{m_0} + C_{m_\alpha}\alpha + C_{m_q} \frac{q\bar{c}}{V} + C_{m_{\delta_e}} \delta_e + C_{m_X}(1-X) \tag{1.7}$$

Note that the drag model of Eq. (1.6) includes the lift coefficient in its lift-induced drag term. $C_L$ itself already includes separation effects. This term could cause complications when applying linear parameter estimation methods, as it would require an accurate $C_L$ estimation to be available. Furthermore, the drag model and the pitch moment model include empirical correction terms $C_{D_X} = \frac{\delta C_D}{\delta X}$ and $C_{m_X} = \frac{\delta C_m}{\delta X}$. The choice of the drag term is intuitive: an increase in flow separation ($X$ moves toward 0) results in increased drag. Finally, it must be noted that this model reduces to the conventional linear form when $X = 1$, or when the flow is fully attached.

### 1.3.4. Two-point Aerodynamic Model

One of the first stall models that was developed through Kirchhoff's flow separation theory used a 2-point aerodynamic model, which describe the forces for the wing and horizontal tail separately [5]. The wing body (wb) lift coefficient was modelled as:

$$(C_L)_{\text{wb}} = C_{L_0} + (C_{L_\alpha})_{\text{wb}} \left( \frac{1+\sqrt{X}}{2} \right)^2 \alpha + (C_{L_q})_{\text{wb}} \frac{qc}{V} + (C_{L_{\dot{\alpha}}})_{\text{wb}} \frac{\dot{\alpha}c}{V} \tag{1.8}$$

and the horizontal tail lift:

$$(C_L)_{\text{t}} = (C_{L_\alpha})_{\text{t}} \alpha_{\text{t}} + (C_{L_{\delta_e}})_t \delta_e \tag{1.9}$$

When wing body lift and the horizontal tail lift are computed separately, the total pitching moment can be computed from this result [34].

Note that this is not the only possibility for a 2-point aerodynamic model. A similar approach can be applied to each side of the main wing, which is further discussed in the next section.

### 1.3.5. Asymmetric Flow Separation

The introduced Kirchhoff model features a single flow separation point that describes all stall-related aerodynamic characteristics of the aircraft. However, an aircraft has 6 Degrees Of Freedom (DOF) and its longitudinal and lateral-directional response during stall are equally relevant. In Section 1.1.3 the degradation in static and dynamic lateral-directional stability was introduced as a consequence of stall. Furthermore, a degradation in aileron effectiveness and an uncommanded roll response are also expected effects of aerodynamic stall. These effects are largely attributed to the concept of asymmetric stall: flow separation does not occur simultaneously on both wings.

Singh [10] demonstrated that the lateral-directional effects of aircraft stall can be modeled more accurately by considering a different flow separation point for each wing. Fischenberg [11] applied this approach for an unsteady 5-DOF aerodynamic model for flow separation and stall. In this approach, two separation points exist: $X_L$ and $X_R$ with the subscripts denoting the left (L) or right (R) wing. Kirchhoff's model can then be defined for the individual wings as follows:

$$(C_L)_w = (C_{L_\alpha})_w \left( \frac{1 + \sqrt{X_w}}{2} \right)^2 \alpha_w, \quad w \in \{L, R\} \tag{1.10}$$

where $\alpha_w$ is the local AOA on the respective wing panel.

Asymmetric flow separation can be accounted for in the lateral-directional model by considering the lift over the individual wings separately. The additional roll and yaw moment due to this asymmetric stall can be approximated as [11]:

$$\Delta C_l = \{(C_L)_L - (C_L)_R\} \Delta y \tag{1.11}$$

$$\Delta C_n = \{(C_D)_L - (C_D)_R\} \Delta y \tag{1.12}$$

where $\Delta y$ denotes the moment arm, which can be estimated from flight test data. An attempt was made to estimate this parameter by making it configuration-dependent [6].

Note that a nonzero contribution to the yaw moment is achieved through unequal drag between the wings. This differential can be achieved by a difference in local AOA, or some dependency of $X$ could be included as a drag model term. The model structure given in Eq. (1.6) could be appropriate for this purpose.

Finally, the notion of different angles of attack corresponding to each wing, as used in Eq. (1.10), is explored. The AOA describes the ratio of the velocity components that the aircraft experiences. The velocity vector at an arbitrary point $P$ on a rigid body flying in a non-moving atmosphere is expressed as follows:

$$\mathbf{V}_p = \begin{bmatrix} u_P \\ v_P \\ w_P \end{bmatrix} = \begin{bmatrix} u_{cg} \\ v_{cg} \\ w_{cg} \end{bmatrix} + \begin{bmatrix} 0 & -r & q \\ r & 0 & -p \\ -q & p & 0 \end{bmatrix} \begin{bmatrix} x_P \\ y_P \\ z_P \end{bmatrix} \tag{1.13}$$

where $p$, $q$, and $r$ describe the roll, pitch, and, yaw rates, respectively.

The local AOA at point $P$ can then be expressed:

$$\alpha_P = \text{atan} \left( \frac{w_P}{u_P} \right) = \text{atan} \left( \frac{w - q\Delta x_P + p\Delta y_P}{u - r\Delta y_P + q\Delta z_P} \right) \tag{1.14}$$

This equation can be applied to the reconstructed AOA returned by a flight path reconstruction method. Alternatively, the local angles of attack can be considered in the observation model of the state estimation step. The used method for flight path reconstruction is discussed in Chapter 3.

## 1.4. Control Surface Effectiveness Modeling

The control surface effectiveness describes the effect of a control surface deflection on the moment about the respective axis.

During an aircraft stall it is possible that the control surfaces stall as well. A recent effort from the research group has shown the effectiveness of using Kirchhoff's flow separation variable $X$ in combination with the elevator deflection $\delta_e$ to model a reduction in elevator effectiveness [9]. In this paper, a similar

approach was attempted for roll control. However, no conclusions for reduced aileron effectiveness could be made.

In order to design a more effective modeling approach it is important to gain more understanding of how the aileron effectiveness, or rolling control authority, changes. Recently, the supposed deterioration of the rolling control authority during stall was experimentally assessed. Specifically, the effect of the negative lift curve slope right after stall on aileron effectiveness was studied [35]. An airplane model and load balance were used for wind tunnel testing at high angles of attack up to 63°. Figure 1.17 presents some important results from this experiment. While the aileron effectiveness is almost constant in the pre-stall AOA range, it deteriorates significantly for all aileron deflections during the stall range of 10°-18°. Note that in this example, for realistic AOAs the effectiveness reduces to about 60% of the pre-stall value.

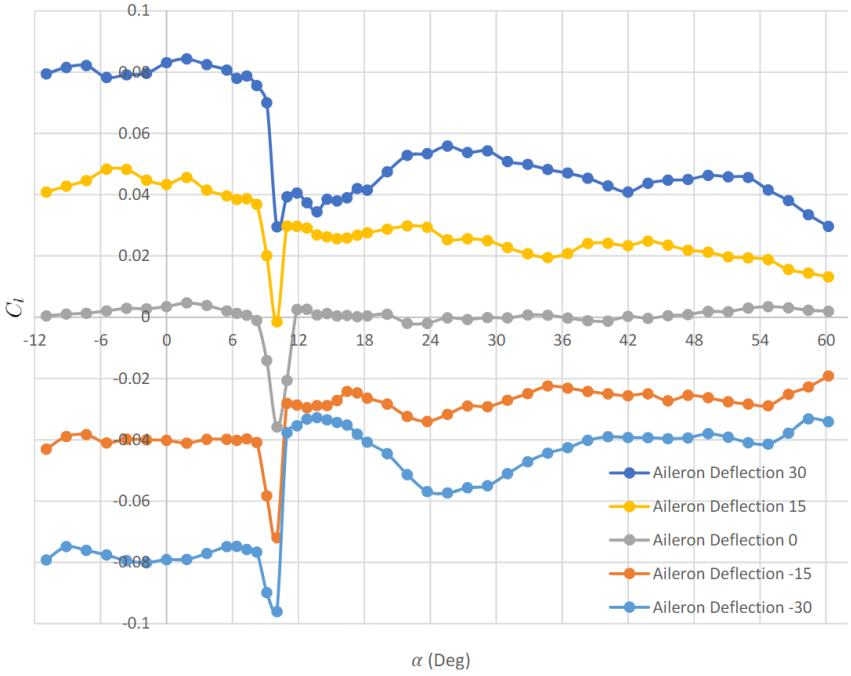


**Figure 1.17:** The roll moment versus AOA at several aileron deflections, as resulted from a wind-tunnel experiment on a scale model. Adapted from [35].

## 1.5. Conclusions

An extensive literature review was performed to gain insight into the aerodynamic stall phenomenon, the primary characteristics to be modeled, the progressions in the stall modeling field, and the state of the art. Kirchhoff's flow separation model is identified as a suitable option, due to its simplicity and its ability to model the lift variation in stall fairly accurately. The model has also been used to demonstrate a stall-related reduced elevator effectiveness. A drawback of Kirchhoff's model is that it provides no method for modeling asymmetric flow separation, resulting in limited lateral-directional model fidelity. To address this issue, modifications to Kirchhoff's model are introduced, which have shown the potential of improving the model in these axes.

From the available measurements, the roll moment signal is most likely to contain information on asymmetric flow separation. In this thesis, the asymmetric Kirchhoff model is implemented to identify flow separation on the individual wings, from the roll moment measurement. Moreover, an attempt is made to identify any stall-related variations in lateral-directional control surface effectiveness.

# 2

# Flight Experiments and Data

There are many alternatives to performing system identification from flight data, such as modern computational methods and wind-tunnel testing. However, important motivations still exist for using flight data. An increasingly more important motivation is the development and requirements of flight simulators, which require accurate representation of the aircraft in all flight regimes. Another purpose of these flight experiments is to verify aircraft specification compliance [36].

For this thesis, a set of flight experiments were conducted. This chapter describes the research aircraft and the instrumentation onboard. Furthermore, a description of the experiment design is presented, in terms of the maneuvers and control inputs. Next, decisions are made about the data sets that are to be used in the identification phase. Finally, some general notes on the flight experiments are given.

## 2.1. Research Aircraft and Instrumentation

The flight data is gathered by conducting experiments with a Cessna Citation II aircraft. Its dimensions, mass, and inertia can be found in Table 2.1. It is owned and operated jointly by Delft University of Technology and the Netherlands Aerospace Center (NLR). The aircraft model is originally designed for the purpose of executive travel. This specific vehicle has been extensively modified by the university and NLR to serve as a versatile airborne research platform. Most notably, the aircraft features an advanced Flight Test Instrumentation System (FTIS), which is a collection of monitoring and recording equipment that is used during flight tests. A crucial part of the FTIS is the air data boom. This device allows for accurate AOA and sideslip measurements. These measurements are especially important when considering system identification. An overview of the FTIS and the measured signals is presented by Table 2.2. For more information on the measured signals and how they are processed, please refer to Chapter 3.

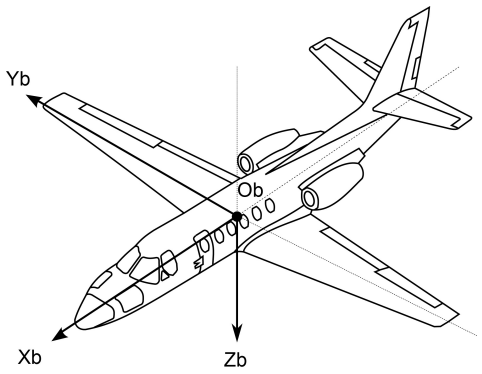


**Figure 2.1:** Schematic diagonal view of the research aircraft with its body-fixed reference frame. Adopted from [9].

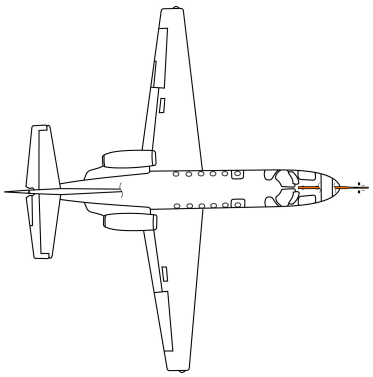

**Figure 2.2:** Schematic top view of the research aircraft, including the air data boom. Adopted from [9].

| Dimensions | | | Mass and inertia | | |
|---|---|---|---|---|---|
| $b$ | 15.9 | m | $MTOW$ | 6600 | kg |
| $l$ | 14.4 | m | $MLW$ | 6100 | kg |
| $\bar{c}$ | 2.09 | m | $M_{dry}$ | 4157 | kg |
| $S$ | 30.0 | $m^2$ | $I_{xx}$ | 12392 | $kgm^2$ |
| $b_{tail}$ | 5.80 | m | $I_{yy}$ | 31501 | $kgm^2$ |
| $S_{tail}$ | 6.20 | $m^2$ | $I_{zz}$ | 41908 | $kgm^2$ |
| | | | $I_{xz}$ | 2252.2 | $kgm^2$ |

**Table 2.1:** Cessna Citation II general specifications.

| Signal(s) | Description | Unit | Source |
|---|---|---|---|
| $x$, $y$, $h$ | Position in ECEF | m | GPS |
| $\dot{x}$, $\dot{y}$, $\dot{h}$ | Velocity in ECEF | $m\,s^{-1}$ | GPS |
| $\phi$, $\theta$, $\psi$ | Attitude | ° | AHRS |
| $V_{TAS}$ | Total airspeed | kt | DADC |
| $\alpha_v$, $\beta_v$ | Boom vane angles | ° | Synchro |
| $\delta_a$, $\delta_e$, $\delta_r$ | controls surface deflections | ° | Synchro |
| $A_x$, $A_y$, $A_z$ | Body accelerations | $m/s^2$ | AHRS |
| $p$, $q$, $r$ | Body rotation rates | ° | AHRS |

**Table 2.2:** FTIS: the measured signals and sources. The position and velocity are measured in the Earth-centered Earth-fixed (ECEF) coordinate system.

## 2.2. Experiment Design

In order to obtain data that is useful for the model identification task at hand, several objectives and recommendations are generated. Furthermore, special attention must be paid to the type of dynamic stall maneuvers that are performed.

### 2.2.1. Objectives and Recommendations

Previous efforts at the research group have led to a substantial database of stall maneuvers. The earliest data was not gathered with the objective of stall model identification. The encouraging results that followed from this research yielded some important recommendations [13]. Firstly, the availability of an accurate sideslip angle measurement was deemed crucial to explain lateral-directional effects. Secondly, dynamic stall maneuvers should be recorded to estimate the dynamic parameters of the flow separation point properly.

An important source of these recommendations was the FAA simulator qualification requirements document [37]. This document emphasizes the stall characteristics to be modeled, as presented in Section 1.1.3. Furthermore, it dictates the maneuvers that are evaluated in the qualification process. Finally, some additional recommendations were given as a result of the most recent stall modeling efforts [9] [12]. The following list serves as a guide for gathering flight data that is useful for stall model identification:

- Fly two types of stall maneuvers:
  1. Wing-level stall (1g).
  2. Accelerated stall (1.1g or 1.3g).
- Fly each of these two stall maneuvers in three conditions:
  1. High altitude in clean configuration.
  2. Approach/landing with corresponding flaps and gear down.
  3. Second-stage climb with flaps other than approach/landing and gear up.
- Excite the aircraft in all three axes to make it possible to estimate transient and unsteady effects.

This also reduces the effect of highly correlated variables, such as $\dot{\alpha}$ and $q$.
- Obtain accurate measurements of the states and inputs (especially the angle of attack and sideslip).
- Include control surface excitations ($\delta_a$, $\delta_e$ and $\delta_r$), during stall approach *and* during the stall itself. Effort must be taken to avoid correlation between the input channels.
- Sufficiently cover the flight envelope for ensuring the model's validity for a wide range of flight conditions.
- Each maneuver should be repeated sufficiently often, such that over-fitting can be avoided and a sufficiently extensive validation data set can be formed.
- Attempt to achieve an angle of attack that is as high as possible.
- Perform a control surface excitation maneuver, such as 3-2-1-1 or doublet, during stall approach. This could be beneficial for identifying control surface effectiveness reduction due to stall

### 2.2.2. Dynamic Maneuvers

As this research's objective is to improve the lateral-directional stall model, specific choices are made to make this an easier task.

Firstly, for some maneuvers it was chosen to deliberately enter the stall with a significant sideslip angle. The pilots had a sideslip readout available to them in the cockpit and they attempted to keep this angle close to 5°. The reason for this choice lies in the fact that normally the sideslip signal is relatively small. This can lead to difficulties in identifying the influence of the sideslip angle on lateral-directional dynamics, while this influence is expected to be quite strong. Furthermore, this means that rudder inputs should be applied during the stall approach and the stall itself, which is one of the recommendations mentioned above.

Another experiment design choice that was made concerned the inputs during the stall on the aileron and elevator channels. Two types of dynamic maneuvers were applied.

**3-2-1-1** This maneuver is used to excite the aircraft dynamics by applying a specific sequence of inputs on a given channel. It is a multi-step signal in which the power is distributed uniformly over a wide frequency range, which was originally proposed by Koehler [38]. It was also part of an analysis of input signals for the purpose of parameter identification [39]. The name of the maneuver describes the time a control surface is deflected into a certain direction: 3 time units positive, 2 negative, 1 positive and 1 negative. An example of a 3-2-1-1 maneuver on the roll channel is presented in Figure 2.3. For the experiment in this thesis an automatic 3-2-1-1 fly-by-wire system was available, which ensures reliable excitations in the roll axis.

The time unit and the amplitude are chosen based on the maximum roll or pitch angle that is safe to achieve. For this same reason, it was chosen to direct the longest positive input ("3") in the opposite direction of the roll angle at which the stall was initiated.

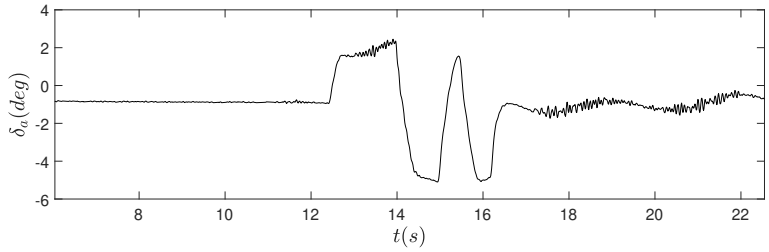


**Figure 2.3:** An example of the 3-2-1-1 aileron maneuver, obtained from the 2022 stall flight experiment.

**Quasi-random (QR) disturbance inputs** Another option for dynamic excitation is to apply quasi-random disturbance inputs. For this maneuver, the pilots attempt to apply seemingly random inputs with as little correlation as possible. Note that this is not a trivial task and correlations and patterns are likely to occur to some extent. This input was applied to the elevator for all stall maneuvers of this experiment. It was also applied to the aileron for some maneuvers. An example of quasi-random disturbance inputs on the elevator is plotted in Figure 2.4.

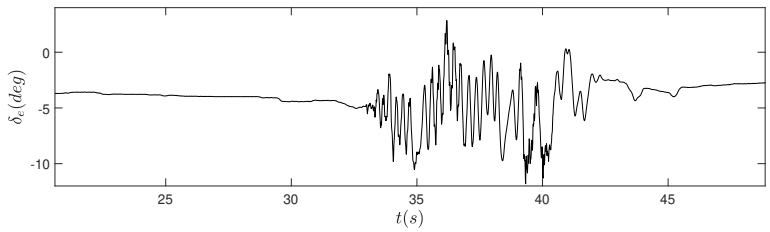


**Figure 2.4:** An example of quasi-random disturbance inputs on the elevator, obtained from the 2022 stall flight experiment

## 2.3. Data Set Synthesis

The data gathered from the newly performed experiments is substantial but insufficient for proper parameter estimation. A collection of stall maneuver data is available from earlier stall modeling efforts at the research group [13] [9]. This section describes how the data is synthesized into a data set which should be useful for the identification of asymmetric stall behavior.

Firstly, only data that includes air data boom measurements are used. The accurate angle of attack and sideslip measurements are deemed vital for identifying asymmetric stall effects. Moreover, a sideslip angle reading is available to the pilots, which makes it possible to intentionally hold this angle during the stall approach.

Secondly, only accelerated stall maneuvers are included in the data set. The main motivation behind this decision is the fact that more asymmetric effects are expected to occur for accelerated stalls than for symmetric ones. Moreover, aileron inputs in the nominal flight envelope are necessary to reach the desired roll angle. This could be of use in modeling a reduction in aileron effectiveness due to stall.

Thirdly, the flight conditions (altitude and configuration) are considered. Since modeling the effects of these flight conditions on the stall behavior is not one of the objectives of this thesis, it is chosen to keep these conditions as constant as possible. The new experiment was performed between FL150 and FL200, as 17 data sets of earlier experiments were also recorded at this level. Finally, only the clean configuration is considered.

The data set that results from these considerations consists of 30 stall maneuvers and is dubbed the *Asym* data set. The data is split into a training set of 24 maneuvers and a validation set of 6 maneuvers (a 80-20 split).

Another data set is considered for the purpose of verification. This collection consists of the data that was used for the earlier stall model, and it is dubbed the *van Ingen* data set. Note that there is a significant overlap in the data sets. The *van Ingen* data set is used as a verification tool of the $X$-parameter estimation method. The data set is split into a training set of 27 maneuvers and a validation set of 7 maneuvers (also roughly a 80-20 split).

| Flight Level | Load factor | Intended sideslip (°) | Input ($\delta_a$ \| $\delta_e$) | Number of data sets |
|---|---|---|---|---|
| 150-200 | 1.1g | 0 | QR \| QR | 12 |
| 150-200 | 1.1g | 0 | 3211 \| QR | 5 |
| 150-200 | 1.1g | 5 | QR \| QR | 1 |
| 150-200 | 1.1g | 5 | 3211 \| QR | 5 |
| 150-200 | 1.3g | 0 | QR \| QR | 7 |

**Table 2.3:** An overview of the maneuvers included in the *Asym* data set.

## 2.4. General Experiment Notes

Previous work in the field of stall model identification has emphasized the importance of the type of stall maneuver that is flown. Several notes were made about the flight experiments by the research group and the test pilots. This section describes the most important takeaways.

| Flight Level | Load factor | Intended sideslip (°) | Input ($\delta_a$ \| $\delta_e$) | Number of data sets |
|---|---|---|---|---|
| 80-110 | 1.0g | 0 | QR \| QR | 2 |
| 110-150 | 1.0g | 0 | QR \| QR | 4 |
| 150-200 | 1.0g | 0 | QR \| QR | 11 |
| 150-200 | 1.1g | 0 | QR \| QR | 10 |
| 150-200 | 1.3g | 0 | QR \| QR | 7 |

**Table 2.4:** An overview of the maneuvers included in the *van Ingen* data set.

The flight test plan was printed in the form of Flight Test Cards (FTCs). These cards describe every maneuver on a separate line. Originally, 40 stall maneuvers were planned, with 10 repetitions of each maneuver. However, due to last-minute technical issues with the fly-by-wire system, a significant portion of the flight time was cut. This led to the decision to repeat every maneuver only 5 times. Moreover, the maneuvers with QR disturbance inputs on both the aileron and elevator channels were repeated in a closely following fashion, as presented in Figure 2.5. This choice will be evaluated at a later stage.

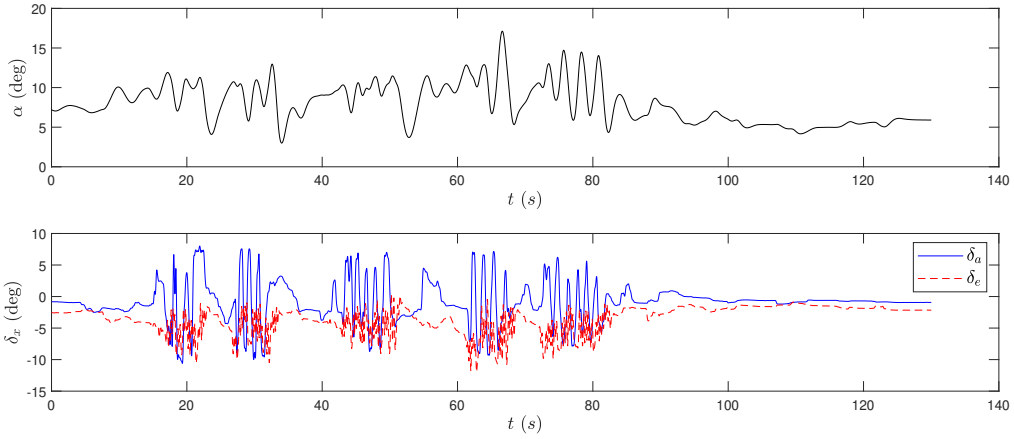


**Figure 2.5:** An example of 5 closely following stalls and the dynamic inputs, obtained from the 2022 stall flight experiment

Additionally, it was planned to apply 3-2-1-1 inputs on the aileron channel and the elevator channel, simultaneously. This was also prevented by technical issues with the fly-by-wire system. Instead, quasi-random disturbance inputs were applied to the elevator.

Furthermore, the test pilots mentioned that it was difficult to keep the sideslip angle at a steady value. For some maneuvers, the test plan described the objective of a 5-degree sideslip angle, which was difficult to maintain. This is not expected to pose an issue as the 5-degree angle is not a requirement in and of itself. The main motivation behind the sideslip specification is having a significant $\beta$ signal when entering the stall; a specific value is not required.

## 2.5. Conclusions

An experiment plan was designed and performed using a research aircraft equipped with an extensive instrumentation suite. A set of objectives and recommendations was generated a priori. To induce asymmetric stall effects, only accelerated stalls are flown and half of the stalls are approached with a nonzero sideslip angle. The 3-2-1-1 input and the Quasi-random disturbance input are used as dynamic maneuvers in the experiment. For this thesis, two data sets are used for different purposes; *van Ingen* for verification of the novel method, and *Asym* for identification and validation of a new stall model.

# 3

# Flight Path Reconstruction

This chapter describes an important step between data gathering and parameter estimation: Flight Path Reconstruction (FPR).

This process aims to address the fact that the measured data is subject to sensor noise and bias. Furthermore, some variables that are used in the parameter estimation step cannot be measured directly. Using the available knowledge of the system dynamics, the state of the aircraft can be estimated with a higher degree of accuracy.

A short recapitulation of previous efforts on FPR method selection for stall model identification is presented. The selected method, the Unscented Kalman Filter, is then described mathematically. Subsequently, The system dynamics are described in terms of the navigation equation and the observation equation. An analysis follows on the observability of the system, and finally, the method's performance is demonstrated.

## 3.1. Kalman Filter Selection

The most widely used method for state estimation is the application of the Kalman Filter. The working principle of the Kalman filter is the computation of a weighted average between the measured and the predicted state, where the weight depends on the statistical uncertainty of the measurements. Several different types of Kalman Filters were developed, each having its own purpose.

The original Kalman Filter (KF) is an optimal linear filter, but can only be used for linear systems. In reality, dynamic systems are rarely linear and the stall maneuvers that are flown for this thesis clearly produce highly nonlinear aircraft dynamics.

The Extended Kalman Filter (EKF) is an adaptation that makes use of linearization of the system, which makes it possible to use for nonlinear systems. However, it does not provide guarantees of global convergence to optimality, which requires an initial condition to be relatively close to the optimum. The Iterated EKF (IEKF) is another adaptation that attempts to improve the convergence using local iterations through measurement update steps, thereby improving the linearization accuracy.

The Unscented Kalman Filter (UKF) has the advantage that no linearization is needed for the algorithm. It is based on the scaled unscented transformation [40]. An important step is the creation of so-called sigma points $\mathcal{X}$, which are subsequently propagated through the system dynamics equations.

The most relevant candidates for this thesis are the IEKF and the UKF. It is important to note that for all Kalman Filters the state and the covariance matrix need to be initialized by the user. Both filters have been implemented by the research group before and an analysis has been performed that selected the UKF as the most suitable option for the purpose of stall modeling [13]. It was reported that, in terms of convergence, no clear distinction between the IEKF and the UKF was identified. However, it was observed that the UKF was more robust to initial conditions. From these considerations, it was decided that this UKF implementation is suitable for the purpose of this thesis.

## 3.2. The Unscented Kalman Filter

The main idea of the UKF is the creation of the sigma-points $\mathcal{X}$ existing in the state space, around the current state estimate, and the propagation of these points through the navigation and observation equations.

The augmented state vector $\mathbf{x}_k^a = \begin{bmatrix} \mathbf{x}_k^\top \mathbf{v}_k^\top \mathbf{w}_k^\top \end{bmatrix}^\top$ is obtained by appending the state vector $\mathbf{x}_k$ with the process noise variables $\mathbf{v}_k$ and the observation noise variables $\mathbf{w}_k$.

To obtain the estimate of the augmented state vector its expectation is computed. It is assumed that the noise can be described by a zero-mean Gaussian distribution. This yields the following estimate:

$$\hat{\mathbf{x}}_{k,k}^a = E\left\{\mathbf{x}_{k,k}^a\right\} = \begin{bmatrix} \hat{\mathbf{x}}_k^\top & \mathbf{0} & \mathbf{0} \end{bmatrix}^\top \tag{3.1}$$

The augmented covariance matrix can also be written. Defining $Q$ and $R$ as the process and observation noise covariance matrices, respectively:

$$P_{k,k}^a = E\left\{\mathbf{x}_{k,k}^a - \hat{\mathbf{x}}_{k,k}^a\right\} = \begin{bmatrix} P_{k,k} & 0 & 0 \\ 0 & Q & 0 \\ 0 & 0 & R \end{bmatrix} \tag{3.2}$$

The augmented set of sigma points is constructed as follows:

$$\begin{aligned} \mathcal{X}_0^a &= \hat{\mathbf{x}}_{k,k}^a \\ \mathcal{X}_i^a &= \hat{\mathbf{x}}_{k,k}^a + \left(\sqrt{(L+\lambda)P_{k,k}^a}\right)_i \qquad i = 1, 2, \ldots, L \\ \mathcal{X}_i^a &= \hat{\mathbf{x}}_{k,k}^a - \left(\sqrt{(L+\lambda)P_{k,k}^a}\right)_{i-L} \qquad i = L+1, L+2, \ldots, 2L \end{aligned} \tag{3.3}$$

where the index $i$ indicates the $i^{th}$ column of a matrix and $L$ is the dimension of $\hat{\mathbf{x}}_{k,k}^a$. The scaling parameter $\lambda$ is defined by some parameters:

$$\lambda = \alpha^2(L + \kappa) - L \tag{3.4}$$

The parameters $\alpha \in [0, 1]$ and $\kappa$ select the spread of the sigma points around the mean. $\kappa$ is set such that $\lambda \neq 0$.

Each sigma point has two corresponding weights. The weights indicated by superscript $m$, are used for computing the new state estimate. Superscript $c$ denotes the weights that are used for computing the updated covariance matrix.

$$\begin{aligned} W_0^{(m)} &= \lambda/(L+\lambda), \\ W_i^{(m)} &= \lambda/(L+\lambda) \end{aligned} \quad i = 1, 2, \ldots, 2L \tag{3.5}$$

and:

$$\begin{aligned} W_0^{(c)} &= \lambda/(L+\lambda) + \left(1 - \alpha^2 + \beta\right), \\ W_i^{(c)} &= W_i^{(m)} \end{aligned} \quad i = 1, 2, \ldots, 2L. \tag{3.6}$$

where $\beta$ is a non-negative tuning parameter. For Gaussian distributions, $\beta = 2$ is optimal. The augmented sigma points set is split into three categories: corresponding to the state, corresponding to the process noise, and corresponding to the observation noise variables.

$$\mathcal{X}_{k,k}^a = \left[\left(\mathcal{X}_{k,k}^{\mathbf{x}}\right)^\top \left(\mathcal{X}_{k,k}^{\mathbf{v}}\right)^\top \left(\mathcal{X}_{k,k}^{\mathbf{w}}\right)^\top\right]^\top \tag{3.7}$$

The split is made to be able to transform the sigma points through their corresponding equations. $\mathcal{X}_{k,k}^{\mathbf{x}}$ is transformed through equation $f$ (Eq. (3.8)). Subsequently, the predicted state estimate, and the predicted state covariance matrix can be computed using these transformed sigma points and their weights (Eq. (3.9) and Eq. (3.10), respectively).

$$\mathcal{X}_{k+1,k}^{\mathbf{x}} = \mathcal{X}_{k,k}^{\mathbf{x}} + \int_{t_k}^{t_{k+1}} f\left(\mathcal{X}_{k,k}^{\mathbf{x}}, \mathbf{u}_k, \mathcal{X}_{k,k}^{\mathbf{v}}\right) dt \tag{3.8}$$

$$\hat{\mathbf{x}}_{k+1,k} = \sum_{i=0}^{2L} W_i^{(m)} \left(\mathcal{X}^{\mathbf{x}}_{k+1,k}\right)_i \tag{3.9}$$

$$P_{k+1,k} = \sum_{i=0}^{2L} W_i^{(c)} \left[\left(\mathcal{X}^{\mathbf{x}}_{k+1,k}\right)_i - \hat{\mathbf{x}}_{k+1,k}\right] \left[\left(\mathcal{X}^{\mathbf{x}}_{k+1,k}\right)_i - \hat{\mathbf{x}}_{k+1,k}\right]^\top \tag{3.10}$$

where $\mathbf{u}_k$ denotes the input vector at discrete time $k$. Furthermore, $\mathcal{X}^{\mathbf{x}}_{k+1,k}$ is transformed again, now by the observation equation $h$ (Eq. (3.11)). Now, the measurement prediction can be calculated (Eq. (3.12)).

$$\mathcal{Y}_{k+1,k} = h\left(\mathcal{X}^{\mathbf{x}}_{k+1,k}, \mathbf{u}_k, \mathcal{X}^{\mathbf{w}}_{k,k}\right) \tag{3.11}$$

$$\hat{\mathbf{y}}_{k+1,k} = \sum_{i=0}^{2L} W_i^{(m)} \left(\mathcal{Y}_{k+1,k}\right)_i \tag{3.12}$$

This concludes the computations of the state prediction and the measurement prediction. Using thes epredictions the innovation covariance $P_{yy}$ and the cross-covariance $P_{xy}$ are obtained as follows:

$$P_{yy} = \sum_{i=0}^{2L} W_i^{(c)} \left[\left(\mathcal{Y}_{k+1,k}\right)_i - \hat{\mathbf{y}}_{k+1,k}\right] \left[\left(\mathcal{Y}_{k+1,k}\right)_i - \hat{\mathbf{y}}_{k+1,k}\right]^\top \tag{3.13}$$

$$P_{xy} = \sum_{i=0}^{2L} W_i^{(c)} \left[\left(\mathcal{X}^{\mathbf{x}}_{k+1,k}\right)_i - \hat{\mathbf{x}}_{k+1,k}\right] \left[\left(\mathcal{Y}_{k+1,k}\right)_i - \hat{\mathbf{y}}_{k+1,k}\right]^\top \tag{3.14}$$

Finally, the Kalman gain $K_{k+1}$ is computed, which makes it possible to update the state and covariance matrix predictions, using the new measurements $\mathbf{y}_{k+1}$.

$$K_{k+1} = P_{xy} P_{yy}^{-1} \tag{3.15}$$

$$\hat{\mathbf{x}}_{k+1,k+1} = \hat{\mathbf{x}}_{k+1,k} + K_{k+1}\left(\mathbf{y}_{k+1} - \hat{\mathbf{y}}_{k+1,k}\right). \tag{3.16}$$

$$P_{k+1,k+1} = P_{k+1,k} - K_{k+1} P_{yy} K_{k+1}^\top \tag{3.17}$$

The steps that were followed above comprise the workings of the UKF at timestep $k$. The procedure is repeated for every timestep.

## 3.3. Navigation Equation

Any Kalman Filter needs to make predictions of the state, thus it requires an internal model of the system dynamics. It is important to realize that a successful Kalman Filter cannot be developed if insufficient knowledge of the system dynamics is available. The system dynamics are expressed through the navigation equation.

### 3.3.1. The Navigation States

The standard navigation equations are written by expressing the aircraft velocity vector in the Earh-centered, Earth-fixed reference frame (ECEF):

$$\begin{aligned}
\dot{x}_E &= [u\cos\theta + (v\sin\phi + w\cos\phi)\sin\theta]\cos\psi - (v\cos\phi - w\sin\phi)\sin\psi + W_{xE} \\
\dot{y}_E &= [u\cos\theta + (v\sin\phi + w\cos\phi)\sin\theta]\sin\psi + (v\cos\phi - w\sin\phi)\cos\psi + W_{yE} \\
\dot{z}_E &= -u\sin\theta + (v\sin\phi + w\cos\phi)\cos\theta + W_{zE}
\end{aligned} \tag{3.18}$$

where ($\phi$, $\theta$, $\psi$) are the Euler angles and ($W_{xE}$, $W_{yE}$, $W_{zE}$) are the estimated wind velocities in ECEF. Furthermore, it is known that the aircraft body velocity ($u$, $v$, $w$) is governed by:

$$\begin{aligned}
\dot{u} &= (A_x - \lambda_x - w_x) - g_0\sin\theta - (q - \lambda_q - w_q)\,w + (r - \lambda_r - w_r)\,v \\
\dot{v} &= (A_y - \lambda_y - w_y) + g_0\cos\theta\sin\phi - (r - \lambda_r - w_r)\,u + (p - \lambda_p - w_p)\,w \\
\dot{w} &= (A_z - \lambda_z - w_z) + g_0\cos\theta\cos\phi - (p - \lambda_p - w_p)\,v + (q - \lambda_q - w_q)\,u
\end{aligned} \tag{3.19}$$

where ($A_x$, $A_y$, $A_z$) and ($p$, $q$, $r$) are the measured linear body accelerations and rotational rates, respectively. Note that sensor biases are taken into account here; ($\lambda_x$, $\lambda_y$, $\lambda_z$) and ($\lambda_p$, $\lambda_q$, $\lambda_r$) describe the accelerometers and rotation rate sensor biases, respectively. Similarly, ($w_x$, $w_y$, $w_z$) and ($w_p$, $w_q$, $w_r$) describe the respective sensor noises. Finally, $g_0 = 9.80665\ \frac{m}{s^2}$ is the constant gravitational acceleration.

Finally, the dynamics of the Euler angles is described by:

$$\begin{aligned}\dot{\phi} &= (p - \lambda_p - w_p) + (q - \lambda_q - w_q)\sin\phi\tan\theta + (r - \lambda_r - w_r)\cos\phi\tan\theta \\ \dot{\theta} &= (q - \lambda_q - w_q)\cos\phi - (r - \lambda_r - w_r)\sin\phi \\ \dot{\psi} &= (q - \lambda_q - w_q)\frac{\sin\phi}{\cos\theta} + (r - \lambda_r - w_r)\frac{\cos\phi}{\cos\theta}\end{aligned} \tag{3.20}$$

### 3.3.2. Additional States and Equations

Several additional states are described in this section. The sensor biases are assumed to be constant, meaning it has no dynamics:

$$\dot{\lambda_i} = 0 \ \forall\ i \in \{x, y, z, p, q, r\} \tag{3.21}$$

The wind velocities are assumed to change slowly over time. Previous research has found that making these variables random walk variables has been effective [13] [9]. The following relation describes this:

$$\dot{W}_{iE} = 0.01 w_N \ \forall\ i \in \{x, y, z\} \tag{3.22}$$

where $w_N$ is a standard normally distributed random variable.

The air data boom vane measures the direction of the local flow ($u_v$, $v_v$, $w_v$). However, the relevant angle of attack is the angle at the center of gravity (CG). The differences between the vane angle ($\alpha_v$) and the angle of attack at the CG ($\alpha$) occur due to aircraft-induced flow effects and body-rotation induced flow velocity components. Similar effects exist for the sideslip angle. An approximation of the vane angles that incorporated the above effects can be written [41]:

$$\alpha_{\mathsf{v}} = \mathsf{atan}\left(\frac{w_{\mathsf{v}}}{u_{\mathsf{v}}}\right) \approx \left(1 + C_{\alpha_{\mathsf{up}}}\right)\mathsf{atan}\left(\frac{w}{u}\right) - \frac{x_{\mathsf{v}_\alpha}\left(q - \lambda_q - w_q\right)}{u} + C_{\alpha_0} \tag{3.23}$$

$$\beta_{\mathsf{v}} = \mathsf{atan}\left(\frac{v_{\mathsf{v}}}{u_{\mathsf{v}}}\right) \approx \left(1 + C_{\beta_{\mathsf{si}}}\right)\mathsf{atan}\left(\frac{v}{u}\right) + \frac{x_{\mathsf{v}_\beta}\left(r - \lambda_r - w_r\right)}{u} - \frac{z_{\mathsf{v}_\beta}\left(p - \lambda_p - w_p\right)}{u} + C_{\beta_0} \tag{3.24}$$

where $x_{v_\alpha}$, $x_{v_\beta}$ and $z_{v_\alpha}$ are the offset distances of the respective vanes, with respect to the CG location.

The body-induced flow effects are described by $C_{\alpha_{up}}$, $C_{\beta_{si}}$, $C_{\alpha_0}$ and $C_{\beta_0}$. Specifically, the former pair describes the upwash and sidewash effects, respectively. Any remaining bias is modeled by the latter pair. The upwash and sidewash components are modeled as random walk variables and the bias terms are assumed constant:

$$\begin{aligned}\dot{C}_{\alpha_{up}} &= C_{\beta_{si}} = 0.01 w_N \frac{\pi}{180} \\ \dot{C}_{\alpha_0} &= \dot{C_{\beta_{si}}} = 0\end{aligned} \tag{3.25}$$

### 3.3.3. Local Angle of Attack

This research will require knowledge of the local AOAs $\alpha_L$ and $\alpha_R$, on the respective wings. For this purpose, the measurement vector can be extended to describe the local angle of attack at location $P$ on the aircraft body:

$$\alpha_P = \mathsf{atan}\left(\frac{w_P}{u_P}\right) = \mathsf{atan}\left(\frac{w - q\Delta x_P + p\Delta y_P}{u - r\Delta y_P + q\Delta z_P}\right) \tag{3.26}$$

where $\Delta x_P$, $\Delta y_P$, and $\Delta z_P$ are the distances of the point P, with respect to the CG location.

Alternatively, the computation of local AOAs can be done after the flight path reconstruction, using the reconstructed body velocities. This approach is taken initially, with $\{\Delta x_L, \Delta y_L, \Delta z_L\} = \{0, -\frac{b}{2}, 0\}$ m and $\{\Delta x_R, \Delta y_R, \Delta z_R\} = \{0, \frac{b}{2}, 0\}$ m. Including this equation in the observation model is investigated in a later phase. This approach could result in observability issues, as possibly the AOA measurement would have to be re-used.

### 3.3.4. Complete Navigation Equation

The navigation equation has the form

$$\dot{\mathbf{x}} = f(\mathbf{x}(t), \mathbf{u}(t), \mathbf{w}(t)) \tag{3.27}$$

The complete navigation equation can now be written out as follows:

$$\dot{\mathbf{x}} = \begin{bmatrix} [u\cos\theta + (v\sin\phi + w\cos\phi)\sin\theta]\cos\psi - (v\cos\phi - w\sin\phi)\sin\psi + W_{xE} \\ [u\cos\theta + (v\sin\phi + w\cos\phi)\sin\theta]\sin\psi + (v\cos\phi - w\sin\phi)\cos\psi + W_{yE} \\ -u\sin\theta + (v\sin\phi + w\cos\phi)\cos\theta + W_{zE} \\ (A_x - \lambda_x - w_x) - g\sin\theta - (q - \lambda_q - w_q)\,w + (r - \lambda_r - w_r)\,v \\ (A_y - \lambda_y - w_y) + g\cos\theta\sin\phi - (r - \lambda_r - w_r)\,u + (p - \lambda_p - w_p)\,w \\ (A_z - \lambda_z - w_z) + g\cos\theta\cos\phi - (p - \lambda_p - w_p)\,v + (q - \lambda_q - w_q)\,u \\ (p - \lambda_p - w_p) + (q - \lambda_q - w_q)\sin\phi\tan\theta + (r - \lambda_r - w_r)\cos\phi\tan\theta \\ (q - \lambda_q - w_q)\cos\phi - (r - \lambda_r - w_r)\sin\phi \\ (q - \lambda_q - w_q)\,\frac{\sin\phi}{\cos\theta} + (r - \lambda_r - w_r)\,\frac{\cos\phi}{\cos\theta} \\ \mathbf{0_{6\times 1}} \\ 0.01 w_N \\ 0.01 w_N \\ 0.01 w_N \\ 0.01 w_N \frac{\pi}{180} \\ 0.01 w_N \frac{\pi}{180} \\ \mathbf{0_{2\times 1}} \end{bmatrix} \tag{3.28}$$

with the state vector **x**, the input vector (the measurements) **u** and the process noise vector **w**, respectively:

$$\mathbf{x} = \begin{bmatrix} x & y & z & u & v & w & \phi & \theta & \psi & \lambda_x & \lambda_y & \lambda_z & \lambda_p & \lambda_q & \lambda_r & W_{xE} & W_{yE} & W_{zE} & C_{\alpha_{\text{up}}} & C_{\beta_{\text{si}}} & C_{\alpha_0} & C_{\beta_0} \end{bmatrix}^\top \tag{3.29}$$

$$\mathbf{u} = \begin{bmatrix} A_x & A_y & A_z & p & q & r \end{bmatrix}^\top \tag{3.30}$$

$$\mathbf{w} = \begin{bmatrix} w_x & w_y & w_z & w_p & w_q & w_r \end{bmatrix}^\top \tag{3.31}$$

## 3.4. Observation Equation

As mentioned before, not all desired variables of interest can be measured directly. However, some relationship often exists between variables of interest and the measured states. The observation equation describes these relationships. It is a crucial part of the Kalman Filter definition.

### 3.4.1. GPS Positioning

The aircraft's position state is already measured by GPS in the ECEF frame, with the exception that the $z$-position is measured negatively. The GPS noise vector is defined as $\mathbf{v}_{GPS} = \begin{bmatrix} v_{x_{GPS}} & v_{x_{GPS}} & v_{x_{GPS}} \end{bmatrix}^T$.

The Kalman Filter makes predictions of the measurements. A transformation from body velocities to ECEF velocities is done in order to make this prediction possible:

$$\begin{aligned} \dot{x}_{\text{GPS}} &= [u\cos\theta + (v\sin\phi + w\cos\phi)\sin\theta]\cos\psi - (v\cos\phi - w\sin\phi)\sin\psi + W_{xE} + v_{\dot{x}_{\text{GPS}}} \\ \dot{y}_{\text{GPS}} &= [u\cos\theta + (v\sin\phi + w\cos\phi)\sin\theta]\sin\psi + (v\cos\phi - w\sin\phi)\cos\psi + W_{yE} + v_{\dot{y}_{\text{GPS}}} \\ \dot{z}_{\text{GPS}} &= u\sin\theta - (v\sin\phi + w\cos\phi)\cos\theta + W_{zE} + v_{\dot{z}_{\text{GPS}}} \end{aligned} \tag{3.32}$$

### 3.4.2. Attitude and Heading Reference System

The aircraft's attitude is expressed by the Euler angles $\phi$, $\theta$, and $\psi$. They are the angles that describe the transformation between an inertial frame and the aircraft body frame.

$$\begin{aligned} \phi_{\text{AHRS}} &= \phi + v_{\phi_{\text{AHRS}}} \\ \theta_{\text{AHRS}} &= \theta + v_{\theta_{\text{AHRS}}} \\ \psi_{\text{AHRS}} &= \psi + v_{\psi_{\text{AHRS}}} \end{aligned} \tag{3.33}$$

The Euler angles, rotational rates, and rotational accelerations are measured by the Attitude and Heading Reference System (AHRS). The rates and accelerations are not included in the observation equation but instead in the inputs to the navigation equation.

### 3.4.3. Digital Air Data Computer

The pressure altitude and the total airspeed are computed in the Digital Air Data Computer (DADC). The altitude measurements from the GPS are more reliable, so the pressure altitude is not used in the Kalman Filter. The total airspeed is computed as follows:

$$V_{TAS} = \sqrt{u^2 + v^2 + w^2} + v_{TAS_{DADC}} \tag{3.34}$$

where $v_{TAS_{DADC}}$ is a noise variable that must not be confused with a velocity component.

### 3.4.4. Air Data Boom

The air data boom has vanes perpendicularly placed to measure the local flow direction, at the vane location. It was already introduced in  that these angles are not equal to the angles at the CG. The sideslip vane measures the so-called flank angle $\beta_{fl}$, which relates to the sideslip angle by $\tan(\beta) = \tan(\beta_{fl})\cos(\alpha)$. The observation equations for the boom vanes are the equations of Eq. (3.28) with a noise term added to each equation.

### 3.4.5. Complete Observation Equation

The observation equation is of the form

$$\mathbf{y} = h(\mathbf{x}(t), \mathbf{u}(t), \mathbf{v}(t)) \tag{3.35}$$

Summarizing the above measurements leads to the complete observation equation:

$$\mathbf{y} = \begin{bmatrix} x + v_{x_{\text{GPS}}} \\ y + v_{y_{\text{GPS}}} \\ -z + v_{z_{\text{GPS}}} \\ [u\cos\theta + (v\sin\phi + w\cos\phi)\sin\theta]\cos\psi - (v\cos\phi - w\sin\phi)\sin\psi + W_{xE} + v_{\dot{x}_{\text{GPS}}} \\ [u\cos\theta + (v\sin\phi + w\cos\phi)\sin\theta]\sin\psi + (v\cos\phi - w\sin\phi)\cos\psi + W_{yE} + v_{\dot{y}_{\text{GPS}}} \\ u\sin\theta - (v\sin\phi + w\cos\phi)\cos\theta + W_{zE} + v_{\dot{z}_{\text{GPS}}} \\ \phi + v_{\phi_{\text{AHRS}}} \\ \theta + v_{\theta_{\text{AHRS}}} \\ \psi + v_{\psi_{\text{AHRS}}} \\ \sqrt{u^2 + v^2 + w^2} + v_{TAS_{\text{DADC}}} \\ \left(1 + C_{\alpha_{\text{up}}}\right)\text{atan}\left(\frac{w}{u}\right) - \frac{x_{\text{v}_\alpha}(q - \lambda_q - w_q)}{} + C_{\alpha_0} + v_{\alpha_{\text{boom}}} \\ \left(1 + C_{\beta_{\text{si}}}\right)\text{atan}\left(\frac{v}{u}\right) + \frac{x_{\text{v}_\beta}(r - \lambda_r - w_r)}{u} - \frac{z_{\text{v}_\beta}(p - \lambda_p - w_p)}{u} + C_{\beta_0} + v_{\beta_{\text{boom}}} \end{bmatrix} \tag{3.36}$$

with the measurement vector **y**, the input vector **u** from Eq. (3.30) and the measurement noise vector **v**.

$$\mathbf{y} = \begin{bmatrix} x_{GPS} & y_{GPS} & z_{GPS} & \dot{x}_{GPS} & \dot{y}_{GPS} & \dot{z}_{GPS} & \phi_{AHRS} & \theta_{AHRS} & \psi_{AHRS} & V_{TAS} & \alpha_{v_{boom}} & \beta_{v_{boom}} \end{bmatrix}^T \tag{3.37}$$

$$\mathbf{v} = \begin{bmatrix} v_{x_{\text{GPS}}} & v_{y_{\text{GPS}}} & v_{z_{\text{GPS}}} & v_{\dot{x}_{\text{GPS}}} & v_{\dot{y}_{\text{GPS}}} & v_{\dot{z}_{\text{GPS}}} & v_{\phi_{\text{AHRS}}} & v_{\theta_{\text{AHRS}}} & v_{\psi_{\text{AHRS}}} & v_{TAS_{\text{DADC}}} & v_{\alpha_{\text{boom}}} & v_{\beta_{\text{boom}}} \end{bmatrix}^\top \tag{3.38}$$

## 3.5. Observability and Convergence

Observability of the system is a necessary condition for a Kalman Filter to converge. A global observability analysis is quite straightforward for linear systems, but it becomes highly complex for nonlinear systems such as the one in question. Local observability analyses can be implemented relatively easily.

A method for local observability analysis from [42] has been implemented in the state reconstruction steps of several system identification projects (including stall modeling), and has led to useful results [43] [9].

The local observability matrix at test point $\mathcal{O}(x_i)$ is constructed using Lie derivatives, at test point $x_i$. This method is highly similar to the observability analysis of linear systems; the condition of local observability is:

$$\text{rank}(\mathcal{O}(x_i)) = n \text{ with } x_i \in \mathbb{R}^n \tag{3.39}$$

The Lie derivative of a system with state equation $f(x)$ and output equation $h(x)$ is expressed as:

$$L_f h(x) = \frac{\partial h(x)}{\partial x} f(x) \tag{3.40}$$

where $L_f$ is the Lie derivative operator and $\frac{\partial h(x)}{\partial x}$ is the Jacobian of the output equation with respect to the state vector $x$. The observability matrix is constructed using a recursive series of Lie derivatives:

$$\mathcal{O}(x) = \begin{bmatrix} L_f^0 h(x) \\ L_f^1 h(x) \\ L_f^2 h(x) \\ \vdots \\ L_f^{n-1} h(x) \end{bmatrix} = \begin{bmatrix} \frac{\partial h(x)}{\partial x} \\ L_f h(x) \\ L_f L_f h(x) \\ \vdots \\ L_f \left( L_f^{n-2} h(x) \right) \end{bmatrix} \tag{3.41}$$

The MATLAB code of [43] and the adjustments of [9] were available for usage with the current observation model. The Lie derivatives and the observation matrices were derived using MATLAB's symbolic toolbox. The observability test was performed on a set of example states which were uniformly sampled from a range that was expected to be reasonable by [9].

| **State** | $x$ | $y$ | $z$ | $u$ | $v$ | $w$ | $\phi$ | $\theta$ | $\psi$ | $\lambda_x$ | $\lambda_y$ |
|---|---|---|---|---|---|---|---|---|---|---|---|
| **Lower Limit** | 0 | 0 | -8000 | 50 | 0 | -10 | 0 | -1.5 | 0 | -0.5 | -0.5 |
| **Upper Limit** | 0 | 0 | 0 | 200 | 20 | 40 | 1.5 | 1.5 | $2\pi$ | 0.5 | 0.5 |

| **State** | $\lambda_z$ | $\lambda_p$ | $\lambda_q$ | $\lambda_r$ | $W_{xe}$ | $W_{ye}$ | $W_{ze}$ | $C_{\alpha_{up}}$ | $C_{\beta_{si}}$ | $C_{\alpha_0}$ | $C_{\beta_0}$ |
|---|---|---|---|---|---|---|---|---|---|---|---|
| **Lower Limit** | -0.5 | -0.5 | -0.5 | -0.5 | 0 | 0 | -10 | 0 | 0 | -1 | -1 |
| **Upper Limit** | 0.5 | 0.5 | 0.5 | 0.5 | 20 | 20 | 10 | 0.5 | 0.5 | 1 | 1 |

**Table 3.1:** The sample range of the test states used for the local observability tests.

The local observability analysis at 1000 test points. All tests returned full observability. Note that while this result improves the confidence in the observability of the system, no guarantees are given for global observability. Since the model is of a high dimension, the range is not fully covered. In order to increase the coverage as much as possible, the number of samples was chosen to be as high as it is. Moreover, the chosen range may not cover the range in actual flight, as for some states the values are more easily estimated than others. In conclusion, a fairly high confidence in observability is gained through this analysis, but the convergence of the filter on real flight data needs to be analyzed for improving this confidence.

The convergence of the UKF implementation with the given system was tested in an earlier effort of stall modeling at the research group [9], by applying the UKF on an accelerated stall maneuver set, using 3 different initial conditions. As for the current research accelerated stall maneuvers are the most relevant

(this maneuver is even included in the data set), the results from this convergence test will be used. It was found that some states do not converge well. The vertical wind component $W_{zE}$ was generally small and removing it from the system improved estimation of the remaining wind components. The bias term of the AOA vane equation $C_{\alpha_0}$ was removed as it was highly correlated with $C_{\alpha_{up}}$, which made the estimates ambiguous. Finally, the sidewash component of the sideslip vane $C_{\beta_{si}}$ and the bias $C_{\beta_0}$ were removed as the sideslip estimations were unreliable if either one was kept in the system.

## 3.6. UKF Performance

The performance of the UKF with the described system is tested by applying it on a stall maneuver data set. One of the newly gathered data sets, from the *Asym* data set is used, as the performance of the UKF implementation on a data set that includes a 3-2-1-1 dynamic aileron maneuver and significant sideslip has not been evaluated before.

The results of the reconstructed measurements and their innovations are presented in Figure 3.1 and Figure 3.2. The filtered states are plotted with their confidence bounds in Figure 3.3 and Figure 3.4. Finally, the raw measurements and the reconstructed inputs are displayed in Figure 3.5. Note the narrow confidence bounds of all relevant states, indicating reliable results of these state estimates. Only the position measurements show significantly larger confidence bounds. however, the positions are irrelevant for the purpose of stall modeling. The states that were removed are indicated with a blank plot.

Finally, the UKF seems to yield reliable results for the sideslip angle when removing both $C_{\beta_{si}}$ and $C_{\beta_0}$, as the confidence bounds on the innovations are relatively narrow. Moreover, the fact that this angle is significantly larger than in previous stall maneuver data sets does not seem to further complicate the reconstruction of this measurement.

## 3.7. Conclusions

To reconstruct the states of the aircraft from the flight data, UKF was selected as the most suitable Kalman Filter, based on an earlier analysis of similar stall data. The navigation equation and the observation equation are described for the current system. A local observability test resulted in observable systems at 1000 test points. the system is slightly modified to improve the convergence of the UKF, according to an earlier analysis with similar data. Finally, the performance of the UKF is demonstrated by applying it to the data of a newly obtained maneuver.

The local AOAs of the individual wings are required for subsequent steps of this thesis. They are computed after the FPR step, using the kinematic relationship of Eq. (3.26), derived from the velocity components on a rigid body. A similar relationship can be used in the observation equation in order to reconstruct the local AOAs through the UKF. This option and the potential issues are further investigated in the remainder of the thesis.

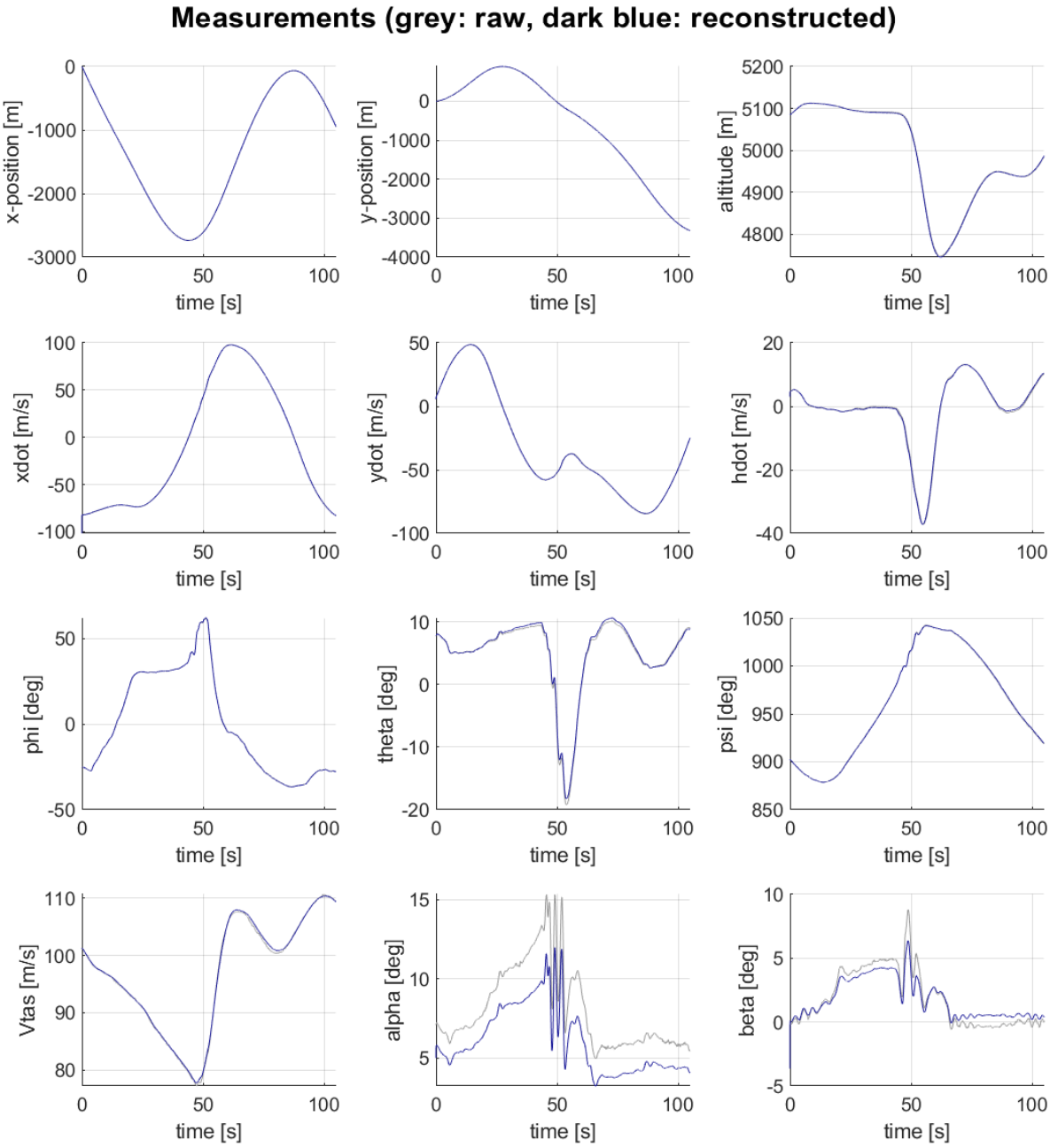


**Figure 3.1:** The reconstructed measurements resulting from the UKF run and the raw measurements, applied to an accelerated stall maneuver.

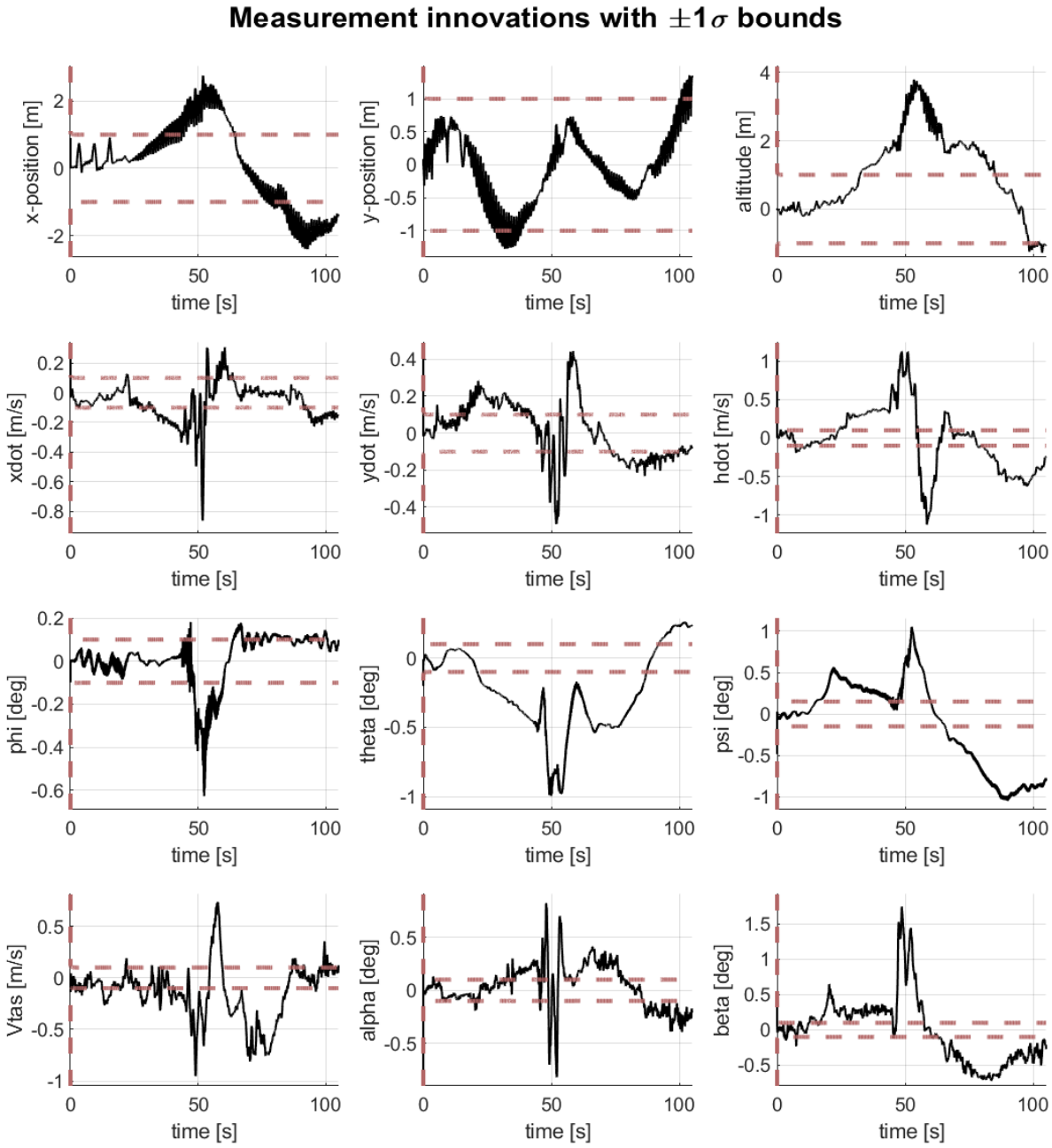


**Figure 3.2:** The measurement innovations and their confidence bounds of the UKF run and the raw measurements, applied to an accelerated stall maneuver.

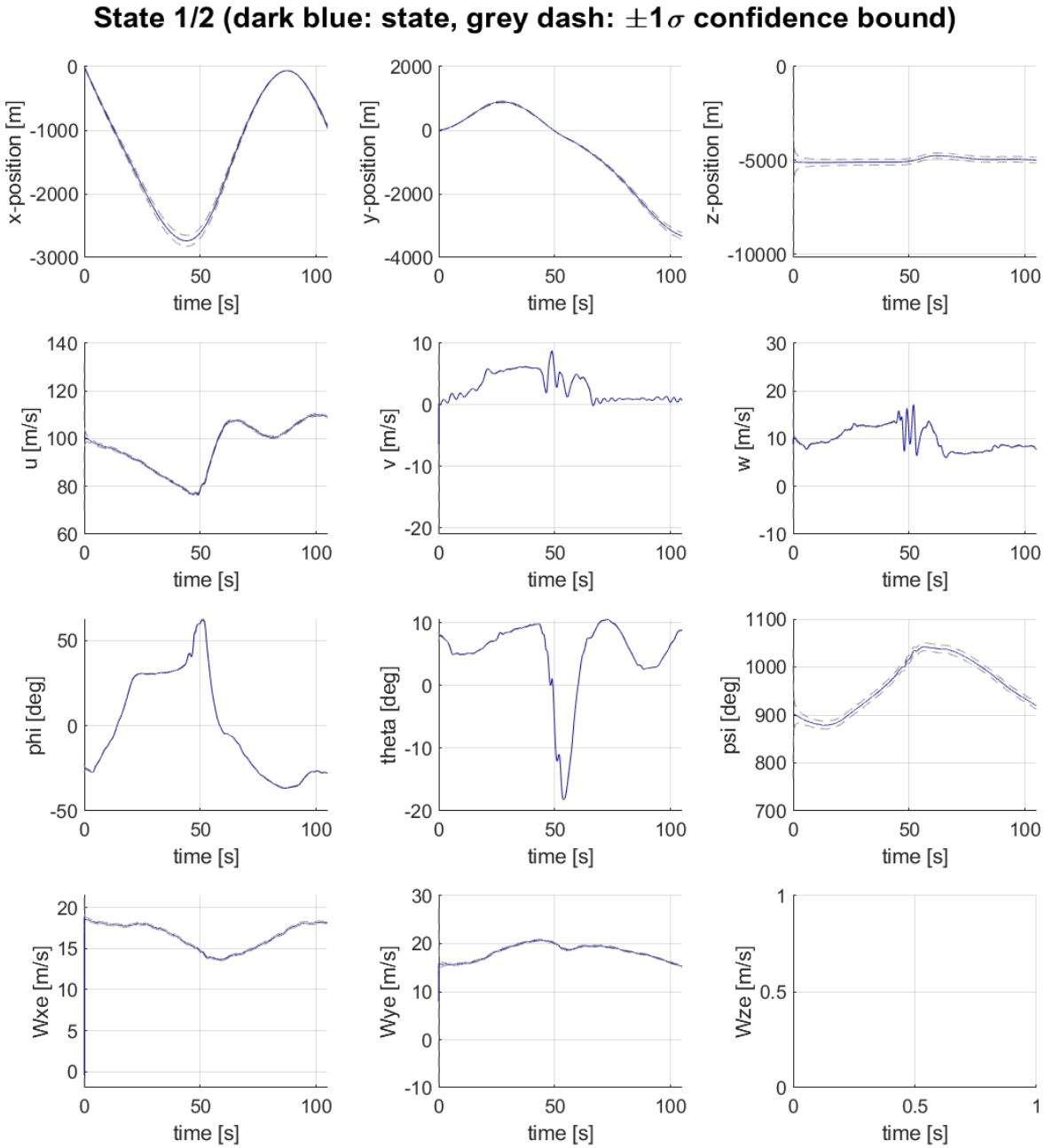


**Figure 3.3:** The filtered states resulting from the UKF applied to an accelerated stall, with the corresponding confidence bounds (1/2).

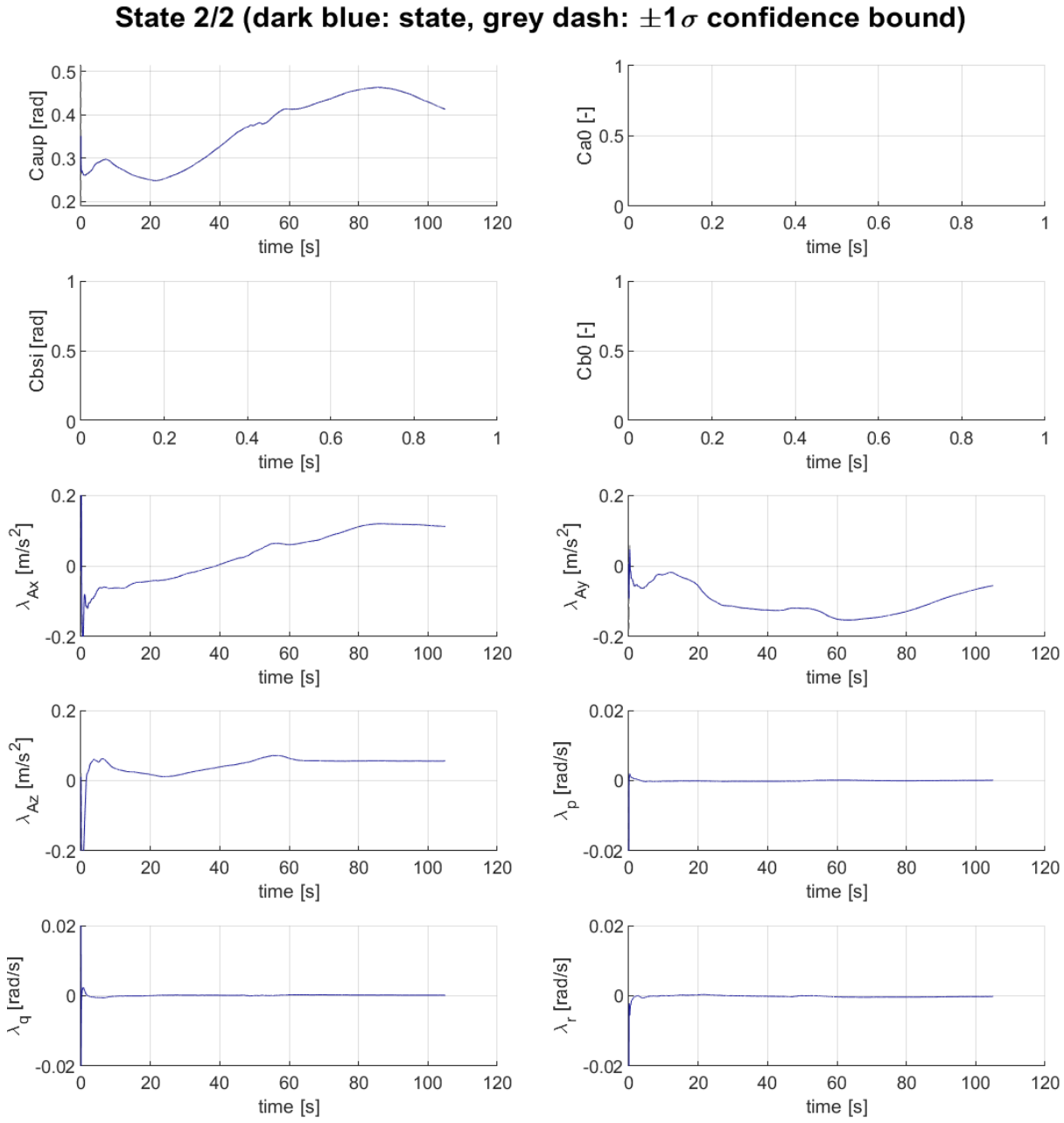


**Figure 3.4:** The filtered states resulting from the UKF applied to an accelerated stall, with the corresponding confidence bounds (2/2).

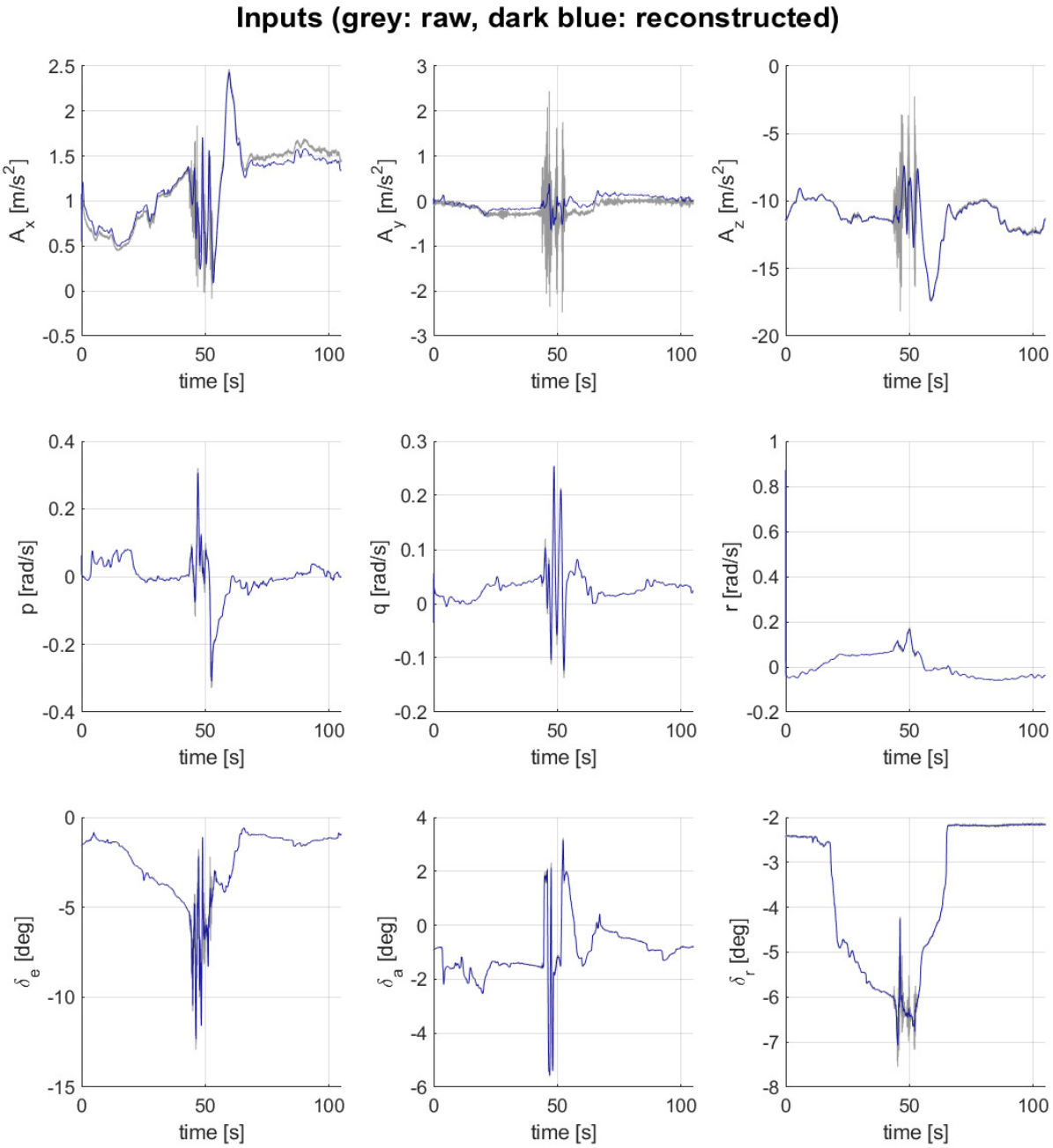


**Figure 3.5:** The raw inputs and the reconstructed inputs to the UKF from an accelerated stall maneuver with a 3-2-1-1 aileron maneuver.

# 4

# Model Structure Selection

This chapter describes the process of selecting the model structure to be used for the linear parameter estimation step. Another model structure selection step is required for the nonlinear parameter estimation step, which will be discussed in Section 5.2. Any model structure that has enough approximation power should be capable of describing the high AOA dynamics of any aircraft. The challenge lies in determining the model terms that describe the specific phenomena of aircraft stall. Initially, a conventional linear aerodynamic model is introduced. Subsequently, regressors are added to the pool of terms through second-order terms and time derivatives of states. Special attention is paid to candidate regressors that describe flow separation and control surface effectiveness. Finally, a semi-objective selection algorithm is described, which uses multivariate orthogonal functions.

## 4.1. Linear Aerodynamic Model

A linearized model structure that describes the longitudinal and lateral-directional behavior of an aircraft in quasi-steady conditions is obtained from literature [36]:

$$C_L = C_{L_0} + C_{L_\alpha}\alpha + C_{L_q}\tilde{q} + C_{L_{\delta_e}}\delta_e \tag{4.1}$$
$$C_D = C_{D_0} + C_{D_\alpha}\alpha + C_{D_q}q + C_{D_{\delta_e}}\delta_e \tag{4.2}$$
$$C_Y = C_{Y_0} + C_{Y_\beta} + C_{Y_p}\tilde{p} + C_{Y_r}\tilde{r} + C_{Y_{\delta_a}}\delta_a + C_{Y_{\delta_r}}\delta_r \tag{4.3}$$
$$C_l = C_{l_0} + C_{l_\beta} + C_{l_p}\tilde{p} + C_{l_r}\tilde{r} + C_{l_{\delta_a}}\delta_a + C_{l_{\delta_r}}\delta_r \tag{4.4}$$
$$C_m = C_{m_0} + C_{m_\alpha}\alpha + C_{m_q}\tilde{q} + C_{m_{\delta_e}}\delta_e \tag{4.5}$$
$$C_n = C_{n_0} + C_{n_\beta} + C_{n_p}\tilde{p} + C_{n_r}\tilde{r} + C_{n_{\delta_a}}\delta_a + C_{n_{\delta_r}}\delta_r \tag{4.6}$$

where $\tilde{p} = \frac{pb}{2V}$, $\tilde{q} = \frac{q\bar{c}}{2V}$ and $\tilde{r} = \frac{rb}{2V}$ are the dimensionless body rotation rates. Removing the dimension allows for a better comparison of the model terms. This model forms the base of the pool of model terms that should each be evaluated.

## 4.2. Additional Model Terms

The Kirchhoff term of Eq. (1.1) has been added to the model structure in previous efforts. This has been shown to significantly increase the approximation power of these high AOA models [5] [13].

Further nonlinearities and dependencies between explanatory variables can be expressed by allowing higher-order terms of the Taylor expansion to be included in the model. Doing so extends the range of validity of the model. Consider the example of the conventional first-order model structure of the pitch moment coefficient of Eq. (4.5). Adding second-order terms yields the following complex form:

$$C_m = C_{m_0} + C_{m_\alpha}\alpha + C_{m_q}\tilde{q} + C_{m_{\delta_e}}\delta_e + C_{m_{\alpha^2}}\alpha^2 + C_{m_{q^2}}\tilde{q}^2 + C_{m_{\delta_e^2}}\delta_e^2 + C_{m_{\alpha q}}\alpha\tilde{q} + C_{m_{\alpha\delta_e}}\alpha\delta_e + C_{m_{q\delta_e}}\tilde{q}\delta_e \tag{4.7}$$

Note that despite the nonlinear terms, the parameter estimation problem is still linear. However, this model is much more complex, and its power in terms of describing the dynamics of the system is not necessarily higher. In fact, high-order polynomial models can suffer from high variance (over-fitting) and they have bad generalization properties outside of the training data range. In order to make a good decision

on the model structure, the explanatory power of each model term must be investigated. This concept is further discussed in Section 4.5.

Univariate spline functions can also be used as model terms. The terms in Eq. (4.1) to Eq. (4.6) and Eq. (4.7) are all globally defined; they are valid for the entire range of the variables. It is impossible to make independent local adjustments that do not influence the rest of the domain. In such cases it is expected that a higher order of terms is required to deal with local nonlinearities. Spline terms are defined locally and undefined elsewhere, allowing for local adjustments at specific ranges of the variables. An example of the mathematical representation of a spline term is:

$$(\alpha - \alpha_i)_+^m = \begin{cases} (\alpha - \alpha_i)^m & \text{if } \alpha > \alpha_i \\ 0 & \text{otherwise} \end{cases} \tag{4.8}$$

Time-dependent effects can be accounted for by including time derivatives of the explanatory variables as model terms. An example of such a term could be $\dot{\alpha}$. This model structure is also linear in the parameters, which ensures finding a globally optimal set of parameters, and greatly decreases the computational burden of parameter estimation.

Finally, an engine model is used for computing the thrust based on measured signals, such as thrust lever setting, and atmospheric conditions. Errors in the engine model are propagated into the computed aerodynamic force and moment coefficients. Therefore, these coefficients are not actually measurements, but rather estimations. Since the thrust coefficient $C_T$ is based on the same engine model, it is beneficial to add this as a regressor in the model. This is evidenced by a similar stall modeling model structure selection process of this aircraft. A more detailed explanation behind this occurence can be found in [9].

## 4.3. Flow Separation Model Terms

Previous work has demonstrated the effectiveness of adding terms that include the flow separation point $X$ to the pool of model terms [5] [34] [11] [8] [9]. The current parameter estimation method allows for the estimation of three flow separation points: $X_L$, $X_R$, and $X$. Chapter 5 details the estimation procedure of these variables. The former two describe the flow separation at the respective wings, while the last-mentioned is the average value of the two variables. Several transformations of these variables are added to the pool of model terms:

$$X, \quad \text{max}(a, X), \quad (1 - X), \quad \left(\frac{1+\sqrt{X}}{2}\right)^2$$

$$(X_L - X_R), \quad \Delta Kirchhoff = \left\{ \left(\frac{1+\sqrt{X_L}}{2}\right)^2 \alpha_L - \left(\frac{1+\sqrt{X_R}}{2}\right)^2 \alpha_R \right\}$$

- $X$ can be used for explaining a reducing or disappearing effect during stall. Conversely, $(1 - X)$ only has an effect when flow separation occurs.
- max$(a, X)$ is used to explain effects that change during stall, but do not completely disappear for fully separated flow. The lower bound $a$ will be empirically chosen based on training results.
- $\left(\frac{1+\sqrt{X}}{2}\right)^2$ is the Kirchhoff term in the lift model. As presented in Figure 4.1, it has a similar shape as $X$ and it is only active in stall.
- $(X_L - X_R)$ describes the difference in flow separation between the two wings. The term is only active when flow separation has occurred on at least one of the wings. It could therefore be a useful term for describing asymmetric stall effects.
- $\Delta Kirchhoff$ describes the difference in the lift between the wings, as described by Kirchhoff's model. In Figure 4.1 the term is denoted by $\Delta Kirchhoff$. Note that the term is stills lightly active outside of the stall. A more detailed description is given for its usage in the initial roll moment model in Section 5.2.2.

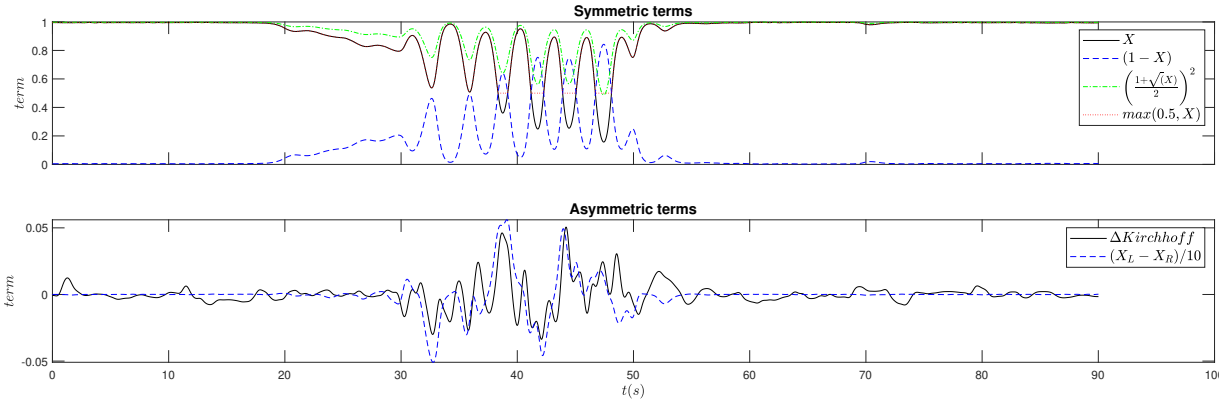


**Figure 4.1:** The symmetric and asymmetric transformations of $X$, $X_L$ and $X_R$ of an example data set, evaluated with the estimated $X$-parameters of [9]. Note that $(X_L - X_R)$ is scaled, which allows for better visual comparison with other terms.

## 4.4. Modeling Variations In Control Surface Effectiveness

In an earlier effort of modeling the stall behavior of the Cessna Citation II, the influence of flow separation on elevator effectiveness was modeled [9]. This was done by considering the regressor max$(a, X)$ with $a = 0.5$. When second-order terms were generated, the cross-term max$(a, X)\delta_e$ was deemed a good explanatory variable. Note that this is an intuitive result; the elevator effectiveness is expected to decrease, but it is not expected to be totally lost. This term describes such an effect.

In Section 1.4 a study was introduced that demonstrated that a maximum loss of aileron effectiveness of around 50% was found for a scale model. A similar approach can be taken towards modeling the hypothesized reduction in aileron effectiveness. However, it must be noted that the left and right aileron may have different flow separation conditions, especially during dynamic maneuvers. Here the convenience of the separate wing flow separation points $X_L$ and $X_R$ is demonstrated. A new regressor is added to the pool:

$$\text{max}(a, \text{min}(X_L, X_R))$$

This regressor describes the maximum amount of flow separation existing at the two wings, with an upper bound $a$. A maximum loss of 50% aileron effectiveness would correspond to $a = 0.5$. However, this upper bound can be adjusted based on the resulting model fit.

## 4.5. Multivariate Orthogonal Function Modeling

A good model structure must have enough explanatory power of the measured data. Furthermore, the model structure must be parsimonious: it must not be more complex than strictly necessary.

For the model to have these qualities, a method must be applied for evaluating the explanatory power of a model term. This is no trivial task, as the terms influence each other. Adding and removing terms is expected to change the estimated value of the other terms. Another challenge is the potential correlation between model terms from flight data. An intuitive example is the correlation between the rate of change of angle of attack $\dot{\alpha}$ and the rotational velocity in pitch $q$. To tackle these challenges use can be made of a Multivariate Orthogonal Functions (MOF) modeling algorithm. Earlier work has proven the effectiveness of this technique for the application of aircraft stall modeling [7] [9].

To initiate the procedure, all model terms are orthogonalized. The main reason behind this step is that it creates the possibility to compute the effect of individual model terms, independently of each other. This yields an objective procedure for model structure selection. The initial inputs to the algorithm are a set of base regressors and a maximum term order variable. Based on the base regressors and the maximum order a set of candidate model terms is generated. Then a bias term is added for every model structure.

$$\mathbf{a_1} = \mathbf{p_1} = \mathbf{1} \tag{4.9}$$

Subsequently, a Gram-Schmidt orthogonalization procedure is performed to orthogonalize all remaining

candidate terms with respect to the currently selected terms. This procedure yields the orthogonalized regression variables $\mathbf{p_j}$, which are linear combinations of the regression variables $\mathbf{a_j}$.

$$\mathbf{p}_j = \mathbf{a}_j - \sum_{k=1}^{j-1} \gamma_{k,j} \mathbf{p}_k, \quad j = 2, 3, \ldots, n, \quad \text{where} \quad \gamma_{k,j} = \frac{\mathbf{p}_k^\top \mathbf{a}_j}{\mathbf{p}_k^\top \mathbf{p}_k} \tag{4.10}$$

After this procedure, the candidate terms can be evaluated. This is done by means of the Predicted Square Error (PSE), which describes a combination of fit error, or MSE, and a term that penalizes complexity.

$$\text{PSE} = \frac{(\mathbf{y} - \hat{\mathbf{y}})^\top (\mathbf{y} - \hat{\mathbf{y}})}{N} + \sigma_y^2 \frac{n}{N} \tag{4.11}$$

where $N$ and $n$ indicate the number of data points and the number of currently selected model terms. $\sigma_Y^2$ is the variance of the modeled signal and acts as a scaling parameter. A requirement for an effective scaling parameter is that its value is independent of the chosen model structure. Alternatively, Morelli considers this term equal to the residual variance estimate for a constant model equal to the mean of the measured response value [7]. The orthogonality property makes it possible to compute the change in PSE which would result from adding candidate $j$ can be computed as follows:

$$\Delta\text{PSE}_j = -\frac{\left(\mathbf{p}_j^\top \mathbf{y}\right)^2}{\mathbf{p}_j^\top \mathbf{p}_j} + \sigma_y^2 \frac{1}{N} \tag{4.12}$$

The candidate term that leads to the greatest reduction in PSE is added to the model. The process of orthogonalization and model term selection is repeated until $\Delta\text{PSE}_j \leq 0 \; \forall \; j \in \{1, 2, ..., n\}$. This condition indicates that the added complexity of any term outweighs the reduction in MSE.

A matrix $P = [\ \mathbf{p}_1 \quad \mathbf{p}_2 \quad ... \quad \mathbf{p}_n\ ]$ is constructed, which is the regression matrix that is used for obtaining the maximum-likelihood parameters $\hat{\phi}$ associated to the orthogonalized regressors. A standard Ordinary Least Squares (OLS) procedure is applied for this purpose. Using a matrix $\Gamma$, a collection of $\gamma_{k,j}$ variables, the OLS result $\hat{\mathbf{y}} = P\hat{\phi}$ is transformed back to the original regression form $\hat{\mathbf{y}} = A\hat{\theta}$:

$$A = P\Gamma \quad \text{with} \quad \Gamma = \begin{bmatrix} 1 & \gamma_{1,2} & \gamma_{1,3} & \cdots & \gamma_{1,n} \\ 0 & 1 & \gamma_{2,3} & \cdots & \gamma_{2,n} \\ 0 & 0 & 1 & \cdots & \gamma_{3,n} \\ \vdots & \vdots & \vdots & \ddots & \vdots \\ 0 & 0 & 0 & \ldots & 1 \end{bmatrix} \tag{4.13}$$

Finally, the optimal original parameter vector $\hat{\theta}$ is obtained through substitution:

$$\hat{\mathbf{y}} = P\hat{\phi} = PI\hat{\phi} = P\left(\Gamma\Gamma^{-1}\right)\hat{\phi} = A\Gamma^{-1}\hat{\phi}, \quad \longrightarrow \quad \hat{\theta} = \Gamma^{-1}\hat{\phi} \tag{4.14}$$

After the optimal parameter vector has been obtained, a final check for the contribution to the model output is performed. This check is carried out by comparing the Root Mean Square (RMS) of the model output $\hat{\mathbf{y}}$ with the RMS of the unchanged model output.

$$\text{RMS} = \frac{1}{N}\sqrt{\hat{\mathbf{y}}^\top \hat{\mathbf{y}}} \tag{4.15}$$

If the change in RMS is lower than threshold of 0.5%, the term is removed due to its small impact. This concludes the execution of the model structure selection algorithm of a single data set. The described algorithm is executed on all flight data sets. Generalization is done by counting the times that a given model term is selected. If the term is selected in at least 50% of the data sets it is included in the model.

While the results of this algorithm are useful for identifying the effectiveness of model terms, other analyses could be required for obtaining a robust model, such as comparisons in model performance, estimated parameter correlations and engineering judgement. For instance, van Ingen [9] demonstrated that cross-terms such as $(1 - X)C_T$ could be selected. However, such a term is impractical to include in a model and its does not explain any known physical phenomena. Hence, it was discarded.

## 4.6. Conclusions

In this chapter, a pool of candidate model terms is collected, starting from the linearized model. Second-order terms, time-derivatives, and spline terms are added to the pool for more explanatory power. Transformations of the flow separation variables $X$, $X_L$, and $X_R$ are added to describe stall-related effects, whereby a distinction is made between symmetric and asymmetric terms. A specific flow separation term is suggested that potentially describes variations in control surface effectiveness. Finally, a Multivariate Orthogonal Functions algorithm is described, which is applied to finally select the most suitable model.

# 5 Parameter Estimation

The objective of parameter estimation is to determine an optimal set of model parameters given a model structure and a set of measurements. The optimality is obtained from the minimization of some cost function. This chapter describes the methodology behind the process. Methods for nonlinear and linear parameter estimation are described and applied to the problem at hand. To conclude the chapter, an overview of evaluation options is presented.

## 5.1. Parameter Estimation Methodology

The system identification approach of this thesis consists of four phases. Figure 5.1 depicts the flow and interdependence between these phases.

*Phase 1: Initialization* consists of (1) gathering a training set of the reconstructed flight data, (2) constructing an initial roll moment model structure that allows for the identification of asymmetric flow separation, and (3) randomly generating initial X-parameters for the nonlinear estimation.

*Phase 2: nonlinear parameter estimation* and *Phase 4: linear parameter estimation* are discussed in detail in this chapter. The model structure selection procedure of *phase 3* was already discussed in Chapter 4.

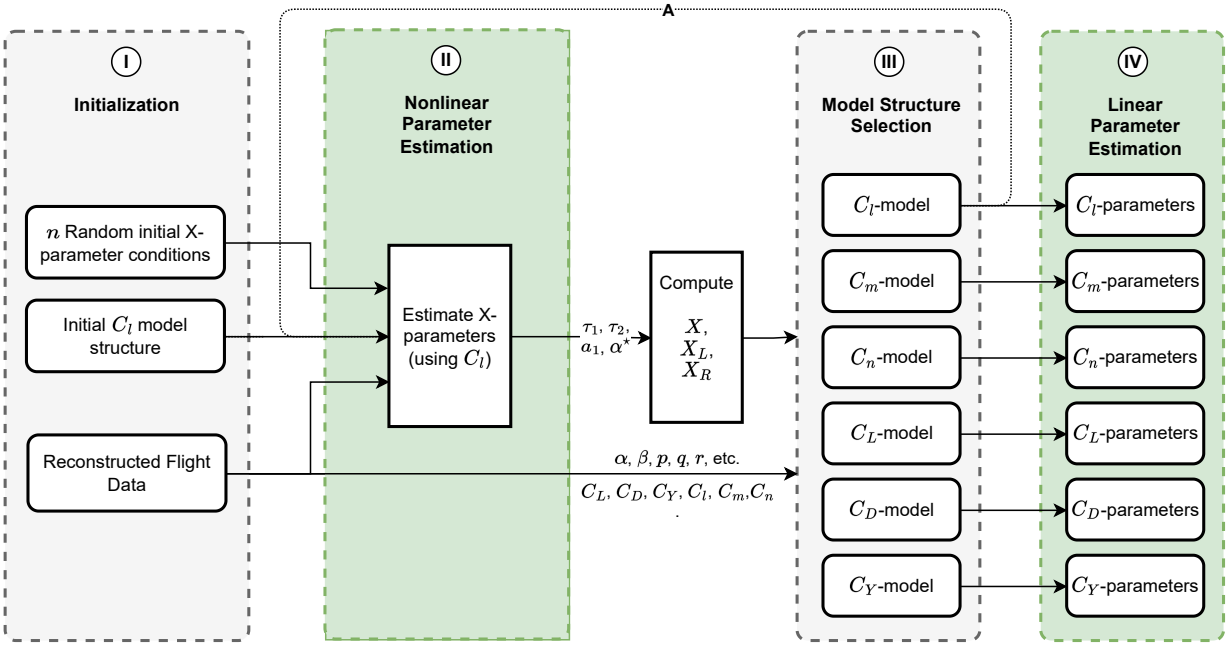


**Figure 5.1:** The parameter estimation methodology in the form of a block diagram.

The parameter estimation approach is split into two parts: the nonlinear X-parameter estimation and the linear $C_i$-parameter estimation. Specifically, the nonlinear parameter estimation concerns the estimation of the vector $\hat{\theta}_X = \begin{bmatrix} \tau_1 & \tau_2 & a_1 & \alpha^* \end{bmatrix}^T$, while the linear parameter estimation concerns the estimation of the coefficients of the force and moment models $C_i$ with $i \in \{L, D, Y, l, m, n\}$. A similar split was made in earlier efforts from the research group [9] [12]. The primary motivation behind this split is the fact that the flow separation variables $X$, $X_L$, and $X_R$, and transformations thereof, can be used as regressors in the $C_i$ model structures. Since these variables are fixed after the first step, the following estimation step concerns a regression model that is linear in the parameters, enabling the use of well-known, reliable, and efficient linear regression techniques. Moreover, the task of model structure selection of the linear model becomes easier, as quick iterations can be evaluated due to the efficient nature of these regression techniques.

## 5.2. Nonlinear Parameter Estimation

Ideally, an objective measure of flow separation is available that can be used as (part of) model terms in the force and moment models. However, determining the $X$-parameters would require extensive wind tunnel testing. Alternatively, the parameters can be estimated from flight data. The flow separation is not measured during flight; alternative measurements should be used as a reference instead. An obvious candidate is the lift coefficient $C_L$. Through Kirchhoff's theory of flow separation, a well-known relation is available between this measurement and flow separation. Previous research has presented good $X$-parameter estimation results using this method [9]. However, applying the MOF-algorithm for model structure selection did not identify useful stall-related terms for the lateral-directional model ($C_Y$, $C_l$, and $C_n$). Moreover, the lateral-directional model had generally much lower accuracy than the longitudinal model. An alternative method is proposed that still allows for the utilization of the relatively simple Kirchhoff model.

### 5.2.1. Kirchhoff's Flow Separation Theory

As a short recapitulation, Kirchhoff's model is presented again. The theory describes that flow separation influences the lift as follows:

$$C_L = C_{L_\alpha} \left( \frac{1 + \sqrt{X}}{2} \right)^2 \alpha \tag{5.1}$$

where the flow separation point $X \in [0, 1]$ is a non-dimensional parameter that takes the value 1 when the flow is fully attached, and it is equal to 0 at full flow separation. This variable is governed by the following differential equation:

$$\tau_1 \frac{dX}{dt} + X = \frac{1}{2} \left\{ 1 - \tanh \left( a_1 \left( \alpha - \tau_2 \dot{\alpha} - \alpha^* \right) \right) \right\} \tag{5.2}$$

### 5.2.2. Initial Roll Moment Model

In Section 1.3.5 the concept of asymmetric flow separation was introduced. Earlier efforts of evaluating the lift of each wing panel separately to model asymmetric flow separation were discussed. While, the total lift coefficient $C_L$ is available from flight data, the individual contributions of each wing $(C_L)_{L,R}$ are not. However, other measurements are available that describe asymmetric behavior: the roll moment coefficient $C_l$ and the yaw moment coefficient $C_n$. The roll moment can be characterized as a lift differential between the two wing panels. Kirchhoff's model could be applied here as well by considering both wings. Assuming the roll moment can be fully described by this lift differential with some unknown moment arm $\Delta y$, and a bias, a model structure for $C_l$ is proposed:

$$\hat{C}_l = C_{l_0} + \Delta y \{ (C_L)_L - (C_L)_R \} \tag{5.3}$$

Then applying Kirchhoff's model to the individual lift contributions:

$$\hat{C}_l = C_{l_0} + \Delta y \left\{ (C_{L_\alpha})_L \left( \frac{1 + \sqrt{X_L}}{2} \right)^2 \alpha_L - (C_{L_\alpha})_R \left( \frac{1 + \sqrt{X_R}}{2} \right)^2 \alpha_R \right\} \tag{5.4}$$

The wings are (almost) perfectly symmetrical. Hence, the following simplification is made:

$$(C_{L_\alpha})_L = (C_{L_\alpha})_R = C_{L_\alpha} \tag{5.5}$$

The initial model structure of the roll moment can than be expressed as

$$\hat{C}_l = C_{l_0} + \Delta y C_{L_\alpha} \left\{ \left( \frac{1+\sqrt{X_L}}{2} \right)^2 \alpha_L - \left( \frac{1+\sqrt{X_R}}{2} \right)^2 \alpha_R \right\} \tag{5.6}$$

Finally, the substitution $C_{l_{\tilde{\alpha}}} = \Delta y C_{L_\alpha}$ is made to obtain the second $C_l$-parameter in this model structure. Note that there is a direct relationship between $C_{L_\alpha}$ and $C_{l_{\tilde{\alpha}}}$. At a later stage, the value of $C_{l_{\tilde{\alpha}}}$ could be verified by applying this relationship with an earlier verified $C_{L_\alpha}$ estimate.

$$\hat{C}_l = C_{l_0} + C_{l_{\tilde{\alpha}}} \left\{ \left( \frac{1+\sqrt{X_L}}{2} \right)^2 \alpha_L - \left( \frac{1+\sqrt{X_R}}{2} \right)^2 \alpha_R \right\} \tag{5.7}$$

Note that it is desirable to have as few parameters as possible to estimate. This model structure requires estimates for 4 $X$-parameters and only 2 additional $C_l$ parameters. A similarly simple model structure of 2 parameters for $C_L$ was used in previous work for successful $X$-parameter estimation [5] [9].

While it is convenient to use a limited number of $C_l$-parameters, it is quite inaccurate. Previous model structure selection procedures have found that dynamic parameters such as the roll rate $p$, the yaw rate $r$ and the aileron deflection $\delta_a$ are good candidates for the roll moment model [9]. Adding these terms yields the initial $C_l$ model:

$$\hat{C}_l = C_{l_0} + C_{l_\beta}\beta + C_{l_p}p + C_{l_r}r + C_{l_{\delta_a}}\delta_a + C_{l_{\tilde{\alpha}}} \left\{ \left( \frac{1+\sqrt{X_L}}{2} \right)^2 \alpha_L - \left( \frac{1+\sqrt{X_R}}{2} \right)^2 \alpha_R \right\} \tag{5.8}$$

This concludes the derivation of the initial roll moment model structure. This model structure is initially used to estimate the $X$-parameters. If a more suitable model structure is selected in subsequent phases, the model is updated and another iteration of the nonlinear estimation is run (refer to loop "B" in Figure 5.1). For instance, note that this structure does not model any aileron effectiveness reduction due to flow separation. At this initial point, no evidence exists of this phenomenon, so it should not be included. If this phenomenon is indeed identifiable, it will be evident from the model structure selection and another iteration of the nonlinear estimation can be performed.

### 5.2.3. $X$-parameter Estimation Procedure

This section described the nonlinear optimization problem. The objective of the estimation method is to minimize the mean squared error between the measured roll moment coefficient $C_l$, and the model output $\hat{C}_l(\theta, x)$. The mathematical formulation of the problem is:

$$\hat{\theta} = \arg\min_{\theta} J(\theta, x) \quad \text{with} \quad J(\theta, x) = \frac{1}{N} \left( C_l - \hat{C}_l(\theta, x) \right)^\top \left( C_l - \hat{C}_l(\theta, x) \right) \tag{5.9}$$

where $C_l$, $\hat{C}_l \in \mathbb{R}^{N \times 1}$ and $N$ denotes the number of data points. $J(\theta, x)$ describes the cost function of the minimization problem.

As introduced before, the $X$-parameters are defined as described by Eq. (5.10). It is assumed that one set of parameters describes the behavior of the flow separation on both wings. This greatly simplifies the problem as the number of parameter is reduced. The fact that the wings are (nearly) perfectly symmetrical makes this assumption likely valid.

$$(\theta_X)_L = (\theta_X)_R = \theta_X = \begin{bmatrix} \tau_1 & \tau_2 & a_1 & \alpha^* \end{bmatrix}^\top \tag{5.10}$$

The parameter vector is constructed by appending the $C_l$-parameters to the $X$-parameters:

$$\theta = \begin{bmatrix} \tau_1 & \tau_2 & a_1 & \alpha^* & C_{l_0} & C_{l_\beta} & C_{l_p} & C_{l_r} & C_{l_{\delta_a}} & C_{l_{\tilde{\alpha}}} \end{bmatrix}^\top \tag{5.11}$$

The nonlinear estimation algorithm that is used does not guarantee convergence to a global optimum. To address this issue, some measures are taken. The cost function is computed for $N_{try}$ randomly generated initial conditions. The estimation is then run for the best $N_{init}$ of these conditions, which are ranked by cost function value. For all the parameters, upper and lower bounds are imposed on the estimation method. The bounds of the $X$-parameters are chosen based on engineering judgement and from results from previous efforts of stall modeling of this aircraft [13] [9] [12].

### 5.2.4. Optimization algorithm selection

Numerous nonlinear optimization algorithms which could be suitable for the current problem exist. The implementation of such an algorithm is outside of the scope of this thesis. Instead, a pre-implemented algorithm from MATLAB's Optimization Toolbox is utilized. In particular, the `fmincon` routine is used, which aims to find the minimum of a constrained nonlinear multi-variable function. The function to be minimized is the cost function of Eq. (5.9).

`fmincon` can be used with four different optimization algorithms:

- Interior-point
- Trust-Region-Reflective
- Sequential Quadratic Programming (SQP)
- Active-set

Several characteristics of the optimization problem are discussed to make a suitable selection for the optimization algorithm. Note that nonlinear optimization is a complex field of research in itself; the objective of this thesis is not to provide the best optimization method possible for this purpose, but rather to select a suitable implementation based on its characteristics.

**Gradient-based methods versus gradient-free methods** The `fmincon` algorithms are gradient-based methods: the partial derivatives with respect to the parameters need to be computed to apply these methods. Alternatively, if the gradient is difficult to obtain, derivative-free algorithms can be applied. These optimization methods are not as well developed as gradient-based methods; current derivative-free algorithms are effective only for small problems [44]. For this reason, and the fact that a gradient can be computed, gradient-free methods are discarded for the current problem.

For gradient-based methods, `fmincon` automatically computes the gradient of the objective function with respect to its parameters, using finite differences. However, it also allows for the manual specification of an objective function gradient. When applying the trust-region-reflective algorithm, the solver even requires this specification. This can improve the speed and reliability of the gradient computations. Moreover, the use of finite differences to obtain the gradient of the solution of an ODE, such as the flow separation point, can be especially prone to numerical errors [45]. Providing a gradient specification can prevent the occurrence of these issues.

**Global optima versus local optima** Nonlinear optimization problems commonly seek only a local solution; a point at which the objective function is smaller than at all other feasible nearby points. A large part of the research on general nonlinear programming has focused on methods for local optimization, which has led to well-developed methods. General nonlinear problems, both constrained and unconstrained, may possess local solutions that are not global solutions. If the objective is to find the global optimum, a possible approach is to perform the optimization for several different initial conditions, and aggregate the results with the smallest cost function values. If a sufficient number of different initial conditions are attempted, it can be said with reasonable confidence that the global solution is found. This is the approach that is taken for this thesis.

**Convexity** The concept of convexity is fundamental in optimization. Many practical problems possess this property, which often makes the problem easier to solve. If the objective function in the optimization problem and the feasible region are both convex, then any local solution of the problem is in fact a global solution [44].

Since the current problem has only lower and upper bounds, the feasible region is convex. The Convexity of the objective function can be tested through the hessian matrix; the jacobian matrix of the objective gradient:

$$\mathbf{H}_J = \begin{bmatrix} \frac{\partial^2 J}{\partial \theta_1^2} & \frac{\partial^2 J}{\partial \theta_1 \partial \theta_2} & \cdots & \frac{\partial^2 J}{\partial \theta_1 \partial \theta_n} \\ \frac{\partial^2 J}{\partial \theta_2 \partial \theta_1} & \frac{\partial^2 J}{\partial \theta_2^2} & \cdots & \frac{\partial^2 J}{\partial \theta_2 \partial \theta_n} \\ \vdots & \vdots & \ddots & \vdots \\ \frac{\partial^2 J}{\partial \theta_n \partial \theta_1} & \frac{\partial^2 J}{\partial \theta_n \partial \theta_2} & \cdots & \frac{\partial^2 J}{\partial \theta_n^2} \end{bmatrix}. \tag{5.12}$$

where $\theta_i$ denote the parameters of the optimization problem.

The objective function is said to be convex when the hessian matrix is positive semi-definite, or equivalently when all of its eigenvalues are non-negative [46]. The `fmincon` routine can return a quasi-Newton approximation of the Hessian matrix at the solution. In general, this Hessian result can be inaccurate, as it is a numerical approximation. Furthermore, proving convexity locally, if possible, does not guarantee global convexity. However, if local convexity is demonstrated at the found solutions it further increases the confidence in it being a global solution. In this thesis, an attempt is made to visualize the cost function and its convexity properties.

**Large-scale algorithms versus medium-scale algorithms** A large-scale optimization problem uses linear algebra that avoids storing and performing operations on full matrices. Sparse linear algebra is applied and sparse matrices are utilized for this purpose. The algorithms contained in the method preserve this sparsity. In contrast, medium-scale methods internally create full matrices and use dense linear algebra. It is not recommended to use these methods on large problems, as full matrices take up more memory, and dense linear algebra can require long execution times. The problem at hand has a limited number of decision variables, meaning it can be classified as medium-scale. Interior-point and trust-region-reflective are large-scale methods, as they are suitable for large, sparse problems, as well as small dense problems. Conversely, the Active-set and SQP methods are medium-scale methods. However, the Active-set algorithm has the ability to take large steps toward the solution direction, which increases the convergence speed.

In general, since the algorithms are available, it is recommended to attempt to solve using interior-point first, then try SQP and Active-set, in the given order, to gain convergence speed. This approach is taken for the first iteration of the nonlinear parameter estimation step.

### 5.2.5. Objective Gradient Specification

Obtaining the gradient of the objective function is not a straightforward task. The difficulty lies in the fact that the flow separation point is governed by an ODE.

The cost function is stated again for clarity:

$$J(\theta, x) = \frac{1}{N} \left( C_l - \hat{C}_l(\theta, x) \right)^\top \left( C_l - \hat{C}_l(\theta, x) \right) \tag{5.13}$$

Furthermore, the initial roll moment model is assumed for this description:

$$\hat{C}_l = C_{l_0} + C_{l_\beta}\beta + C_{l_p}p + C_{l_r}r + C_{l_{\delta_a}}\delta_a + C_{l_{\bar{\alpha}}} \left\{ \left( \frac{1+\sqrt{X_L}}{2} \right)^2 \alpha_L - \left( \frac{1+\sqrt{X_R}}{2} \right)^2 \alpha_R \right\} \tag{5.14}$$

and the objective is to find the gradient of the objective function with respect to the parameter vector:

$$\theta = \begin{bmatrix} \tau_1 & \tau_2 & a_1 & \alpha^* & C_{l_0} & C_{l_\beta} & C_{l_p} & C_{l_r} & C_{l_{\delta_a}} & C_{l_{\bar{\alpha}}} \end{bmatrix}^\top \tag{5.15}$$

For the $C_l$-parameters, the gradient is relatively straightforward, as the roll moment has a linear relationship with these parameters. However, the $X$-parameters are not directly related to the roll moment, but through the ODEs of the respective flow separation points:

$$\frac{\mathrm{d}}{\mathrm{d}t} X_w(t, x, \theta) = \frac{1}{\tau_1}(-X_w + \frac{1}{2} - \frac{1}{2}\tanh\left[a_1\left(\alpha_w - \tau_2 \dot{\alpha_w} - \alpha^*\right)\right]) \quad \text{for} \quad w \in \{L, R\} \tag{5.16}$$

where $x$ denotes the aircraft state, as the ODE depends on the angle of attack and its rate. Note that the assumption of a single set of $X$-parameters is maintained in this derivation. To obtain the gradient of

the objective function with respect to these parameters the chain rule needs to be applied. The full gradient formulation is then as follows:

$$\frac{\partial J(\theta,x)}{\partial \theta_i} = \begin{cases} \frac{\partial J}{\partial \hat{C}_l}\frac{\partial \hat{C}_l}{\partial X_L}\frac{\partial X_L}{\partial \theta_i} + \frac{\partial J}{\partial \hat{C}_l}\frac{\partial \hat{C}_l}{\partial X_R}\frac{\partial X_R}{\partial \theta_i} & \text{with } \theta_i \in \{\tau_1\ \tau_2\ a_1\ \alpha^*\} \\ \frac{\partial J}{\partial \hat{C}_l}\frac{\partial \hat{C}_l}{\partial \theta_i} & \text{with } \theta_i \in \left\{C_{l_0}\ C_{l_\beta}\ C_{l_p}\ C_{l_r}\ C_{l_{\delta_a}}\ C_{l_{\tilde{\alpha}}}\right\} \end{cases} \tag{5.17}$$

Obtaining the sensitivity of the flow separation points to its parameters $\frac{\partial X_L}{\partial \theta_i}$ and $\frac{\partial X_R}{\partial \theta_i}$ is the most challenging step. A method is used that evaluates the gradient numerically and solves the ODE simultaneously, as described by [47]. It was successfully implemented for a single flow separation point in [9].

The flow separation ODEs of Eq. (5.16) are rewritten:

$$\frac{\mathrm{d}X_w(t,x,\theta)}{\mathrm{d}t} = G_w(X_w,t,x,\theta) \quad \text{for} \quad w \in \{L,R\} \tag{5.18}$$

and the partial derivatives to be obtained are written as follows:

$$\frac{\partial X_w(t,x,\theta)}{\partial \theta} = S_w(t,x,\theta) \quad \text{for} \quad w \in \{L,R\} \tag{5.19}$$

The partial derivatives of Eq. (5.18) with respect to $\theta$ are taken to get the result:

$$\frac{\partial}{\partial \theta}\frac{\mathrm{d}}{\mathrm{d}t}X_w(t,x,\theta) = \frac{\partial G_w(X_w,t,x,\theta)}{\partial X_w}\frac{\partial X_w(t,x,\theta)}{\partial \theta} + \frac{\partial G_w(X_w,t,x,\theta)}{\partial \theta} \quad \text{for} \quad w \in \{L,R\} \tag{5.20}$$

Finally, Eq. (5.19) is substituted to obtain an additional ODE:

$$\frac{\mathrm{d}}{\mathrm{d}t}S_w(t,x,\theta) = \frac{\partial G(X_w,t,x,\theta)}{\partial X}S_w(t,x,\theta) + \frac{\partial G_w(X_w,t,x,\theta)}{\partial \theta} \quad \text{for} \quad w \in \{L,R\} \tag{5.21}$$

where the initial conditions are $S_w(0,x,\theta) = \mathbf{0}$. These ODEs can be solved numerically for $S_w(t,x,\theta)$ to complete the gradient computation of Eq. (5.17).

## 5.3. Linear Parameter Estimation

Many difficulties of nonlinear optimization methods do not exist for linear optimization. For instance, a global optimum can be guaranteed and gradients are computed easily. Moreover, linear optimization techniques are generally computationally much more efficient, and therefore, fast.

When the flow separation point is included in the model structure of a force or moment coefficient $C_i$ with $i \in \{L,D,Y,l,m,n\}$, the structure becomes nonlinear, rendering the usage of linear methods impossible. However, the benefit of isolating the parameter estimation steps is found when the flow separation points are fixed after the nonlinear estimation phase; the $C_i$ model structures become linear.

The set of regression variables is now appended with $X$, $X_L$ and $X_R$ and transformations thereof. The model output $\hat{C}_i$ can be written in terms of a matrix of regression variables $A(x)$ and the model parameters $\theta$:

$$\hat{C}_i = A(x)\theta \tag{5.22}$$

where $x$ are the regression variables. For brevity, the regression matrix will be denoted $A = A(x)$. The linear parameter estimation problem is defined with a quadratic cost function, similar to the nonlinear problem. Note that the cost function is not the MSE, but a similar second-order function.

$$\hat{\theta} = \arg\min_{\theta} J(\theta,x) \quad \text{with} \quad J(\theta,x) = \frac{1}{2}\left(C_i - \hat{C}_i(\theta,x)\right)^\top \left(C_i - \hat{C}_i(\theta,x)\right) \tag{5.23}$$

The Ordinary Least-Squares (OLS) method is derived by substitution of Eq. (5.22) and setting the cost function gradient with respect to the parameters equal to zero:

$$J(\theta,x) = \frac{1}{2}\left(C_i - A\theta\right)^\top \left(C_i - A\theta\right) \tag{5.24}$$

$$\frac{\partial J(\hat{\theta})}{\partial \theta} = 0 \quad \longleftrightarrow \quad -A^T(C_i - A\hat{\theta}) = 0 \tag{5.25}$$

$$A^T A\hat{\theta} = A^T C_i \tag{5.26}$$

$$\hat{\theta} = \left[A^T A\right]^{-1} A^T C_i \tag{5.27}$$

The second gradient of the cost function with respect to the parameter vector is equal to $A^\top A$, which is positive definite, indicating a minimum rather than a maximum. The least-squares estimator was developed under the assumptions of a model structure that is linear in the parameters, with deterministic regressors, and a white measurement noise with constant variance [36].

If the model error sources only include sensor noise, then the white noise assumption is reasonable. However, if the remnant includes other modeling errors, more advanced methods such as weighted least-squares (WLS) could improve the results.

## 5.4. Evaluation

This chapter has discussed two optimization methods. An important given for optimization is the requirement of an objective function or cost function. The nonlinear parameter estimation problem utilizes the MSE as the cost function, while the linear estimation method is derived from a similar quadratic cost function. However, the quality of the resulting model can be evaluated through several different metrics, each with its own purpose. In this section, some metrics are introduced and their relevancy to asymmetric stall modeling is discussed.

### 5.4.1. Mean-Squared-Error

The MSE describes the average value of the model residuals:

$$\text{MSE } = \frac{1}{N}\sum_{k=1}^{N}\left(z_k - \hat{z}_k\right)^2, \tag{5.28}$$

where $N$ is the number of measurement samples, $z_k$ is the $k$-th measurement sample and $\hat{z}_k$ denotes the corresponding model output.

Note that despite the averaging, the MSE is a measure of absolute difference. When applying the metric to the model output of the aerodynamic coefficients, the results between the two coefficients cannot be compared directly. For instance, the MSE of the $C_L$ model is expected to be higher than that of the $C_l$ model, while the model fit is expected to be better. Furthermore, the MSE can be averaged over the six models in order to obtain an absolute measure of overall model fit.

### 5.4.2. Parameter Variance and Correlation

Both estimation steps are performed on a group of data sets. Before the estimations are averaged to obtain The final estimate, the variance of every parameter estimate can be evaluated. Especially for the nonlinear estimation step the variance can give important information about the convergence of the method. Furthermore, the correlation between parameters can be evaluated through the correlation matrix:

$$C(\theta) = \text{cor}(\Theta) \tag{5.29}$$

where $\Theta$ is a ($n_d$ x $n_p$)-matrix containing the $n_d$ estimates (data sets) of the $n_p$ parameters. The matrix element $C_{ij}$ describes the correlation between parameters $\theta_i$ and $\theta_j$. If this value is close to 1 (positive correlation) or -1 (negative correlation), the parameters are expected to describe the same phenomena, which could lead to difficulties with the physical interpretation of the parameter values. A solution is to remove the model term in question. A common rule is to regard correlations as problematic if the absolute correlation value is larger than 0.9 [36].

### 5.4.3. Variance Accounted For

An absolute measure of model fit, such as MSE, cannot be used to compare the accuracy of the different models, as the scale differs with the aerodynamic coefficients. The Variance Accounted For (VAF) is a relative measure of fit, due to scaling with the measurement value:

$$\text{VAF} = 100\% \times \left(1 - \frac{\sum_{k=1}^{N} (z_k - \hat{z}_k)^2}{\sum_{k=1}^{N} z_k^2}\right) \tag{5.30}$$

The upper limit of the VAF metric is 100%, but it can take any negative value.

This metric can be utilized for comparing the model of the accuracy of the individual aerodynamic coefficients.

### 5.4.4. Coefficient of Determination

The coefficient of determination $R^2$ represents the proportion of the variation in the measured output that is explained by the model. It is useful for evaluating the relevance of model terms. Adding a regressor to the model will always increase $R^2$. An adequate model is achieved when $R^2$ is not substantially increased by the addition of any new term [36].

$$R^2 = 1 - \frac{\sum(\mathbf{z} - \hat{\mathbf{z}})^2}{\sum (\mathbf{z} - \mu_z)^2} \tag{5.31}$$

where $0 \leq R^2 \leq 1$ and $R = 1$ represents a perfect fit to the data.

### 5.4.5. Theil's Statistics

Theil's U-coefficient is another normalized metric for model quality. It ranges from 0 to 1, corresponding to worst and best model fit, respectively.

$$U = \frac{\sqrt{\frac{1}{N}\sum(\mathbf{z} - \hat{\mathbf{z}})^2}}{\sqrt{\frac{1}{N}\sum \mathbf{z}^2} + \sqrt{\frac{1}{N}\sum(\hat{\mathbf{z}})^2}} \tag{5.32}$$

The coefficient can be divided by the error source; bias ($U_{bias}$), variance ($U_{var}$), and covariance ($U_{cov}$). The respective components are computed as follows:

$$U_{\text{bias}} = \frac{(\overline{\mathbf{z}} - \hat{\mathbf{z}})^2}{\frac{1}{N}\sum(\mathbf{z} - \overline{\mathbf{z}})^2} \tag{5.33}$$

$$U_{\text{var}} = \frac{(\sigma_y - \sigma_{\hat{z}})^2}{\frac{1}{N}\sum(\mathbf{z} - \overline{\mathbf{z}})^2} \tag{5.34}$$

$$U_{\text{cov}} = \frac{2\,(1 - \rho_{y\hat{z}})\,\sigma_y \sigma_{\hat{z}}}{\frac{1}{N}\sum(\mathbf{z} - \overline{\mathbf{z}})^2} \tag{5.35}$$

where $\sigma$ and $\rho$ denote the standard deviation and the cross-correlation, respectively.

An important given from these definitions is that the bias, variance, and covariance always add up to one. They can be used as fractions, where $U_{var}$ relates to scaling errors, $U_{cov}$ describes any errors that are uncorrelated to the signals, or random. Using Theil's statistics, an analysis can be performed on the error sources of the model.

### 5.4.6. Statistical Tests

Several statistical tests can be used for model evaluation, as they are readily implemented in MATLAB.

The one-sample Kolmogorov-Smirnov (KS) tests the null-hypothesis that data comes from a standard normal distribution, against the alternative hypothesis that it does not come from such a distribution. It is available in matlab through the `kstest` routine. In order to use this routine, the estimates need to be corrected for their mean and standard deviation [48].

The parametric one-sample $t$-test tests that the null hypothesis that the data comes from a zero-mean normal distribution, against the alternative hypothesis which states that the original distribution is not zero-mean. The test can be done by MATLAB's `ttest` routine. It can be used to gain a degree of certainty that the real parameter to be estimated is unequal to zero. If the null-hypothesis is accepted, including this parameter in the model might be unnecessary or incorrect.

The non-parametric Wilcoxon's signed-rank one-sample test has a similar objective: it tests the null hypothesis that the data comes from a distribution whose median is zero [49]. MATLAB's `signrank` routine can be utilized for this purpose.

For the $t$-test and the signed-rank test a Bonferroni correction can be applied to avoid incorrectly rejecting the null-hypothesis due to an increasing amount of rare events. This is done by testing each

hypothesis at a significance level of $\frac{\alpha}{m}$ where $\alpha$ is the overall significance level and $m$ is the number of hypotheses.

## 5.5. Conclusions

The proposed parameter estimation methodology has been presented in this chapter. The novelty of this thesis is introduced: the nonlinear estimation of flow separation parameters from the roll moment measurement. For this purpose, the selection of a suitable initial roll moment model structure is detailed. The readily available interior-point method is initially selected as the most suitable algorithm to solve the posed nonlinear optimization problem. Since this method is gradient-based, the gradient of the objective function with respect to the parameters needs to be evaluated. To avoid numerical inaccuracies of finite difference methods applied to ODE parameters, A method is used that evaluates the gradient numerically and solves the ODE simultaneously. To evaluate the nonlinear optimization, a parameter variance and correlation analysis, and statistical tests are performed.

When the flow separation parameters are estimated, a linear least-squares regression procedure ensues to estimate the aerodynamic model structure parameters. The final model is validated by applying the model to a separate validation set and computing metrics such as MSE, VAF, $R^2$, and Theil's Statistics.

# 6

# Preliminary Results

This chapter presents the results of the proposed preliminary asymmetric stall model. The feasibility study of estimating the $X$-parameters from the roll model is evaluated, by analysis of the $X$-parameter estimates. Subsequently, using the estimated parameters, the model structure selection results are presented. In this section, special attention must be paid to selecting model structures that allow for identifying changes in control surface effectiveness. The selected model structure is finally used for the linear parameter estimation process, which yields the aerodynamic parameter estimates.

## 6.1. $X$-parameter Estimation

This section describes the results of the first iteration of the $X$-parameter estimation step. Note that the only model structure selection step that is performed until this point is the initial roll moment model, as was detailed in Section 5.2.2. While the nonlinear optimization problem has 10 decision variables, only the 4 $X$-parameters are used for the subsequent model structure selection and linear parameter estimation steps. Therefore the analysis of the estimates is limited to the $X$-parameters.

The results of the estimation method is presented in Table 6.1. The estimation procedure is ran on the *Asym* and *van Ingen* data sets. The table also features the estimations from the previous method for comparison [9].

The optimization is run for all training sets of both data sets. To reduce the total number of optimizations the cost function was evaluated at 500 different initial conditions. The optimization was executed on the best 300 of these initial conditions, based on the cost function value. To obtain the final estimates $\hat{\theta}_X$, the median over all training sets is taken for every parameter. In this section, statistical analyses are performed on the results of both data sets.

| | **van Ingen - new method** | | | **van Ingen - previous method** | | | **Asym - new method** | | |
|---|---|---|---|---|---|---|---|---|---|
| $\theta$ | $\hat{\theta}$ | Bounds | $\sigma_{\hat{\theta}}$ | $\hat{\theta}$ | Bounds | $\sigma_{\hat{\theta}}$ | $\hat{\theta}$ | Bounds | $\sigma_{\hat{\theta}}$ |
| $\tau_1$ [s] | 0.0874 | [0.001, 0.80] | 0.1648 | 0.2547 | [0.001, 0.80] | 0.1565 | 0.0743 | [0.001, 0.80] | 0.1257 |
| $\tau_2$ [s] | 0.5649 | [0.000, 0.95] | 0.1770 | 0.0176 | [0.000, 0.50] | 0.0819 | 0.6224 | [0.000, 0.95] | 0.1625 |
| $a_1$ [-] | 17.068 | [15.00, 40.0] | 5.3410 | 27.671 | [15.00, 40.0] | 6.7177 | 17.452 | [15.00, 40.0] | 3.4355 |
| $\alpha^*$ [rad] | 0.1551 | [0.100, 0.35] | 0.0466 | 0.2084 | [0.100, 0.35] | 0.0202 | 0.1444 | [0.100, 0.35] | 0.0422 |

**Table 6.1:** $X$-parameter estimates of the proposed method applied on the *van Ingen* and the *Asym* data sets. The estimates of [9] are dispayed for comparison.

### 6.1.1. Van Ingen Data Set

The primary motivation of applying the proposed method on the *van Ingen* data set is to investigate the feasibility of estimating the $X$-parameters from the roll moment. This is a novel approach that can be partially verified by the comparison with the available results.

Figure 6.1 presents the parameter estimates of the proposed method in the form of a matrix plot. The individual training set estimates and the final aggregated estimates are plotted, together with the final estimates from [9]. Furthermore, the figure includes histograms that present the distribution of the

parameter estimates over the data sets. The correlation coefficient $\rho$ between the two parameters of the corresponding axes is also depicted in the respective plots. Finally, the individual estimates are grouped by the type of stall maneuver that was flown, in terms of load factor.

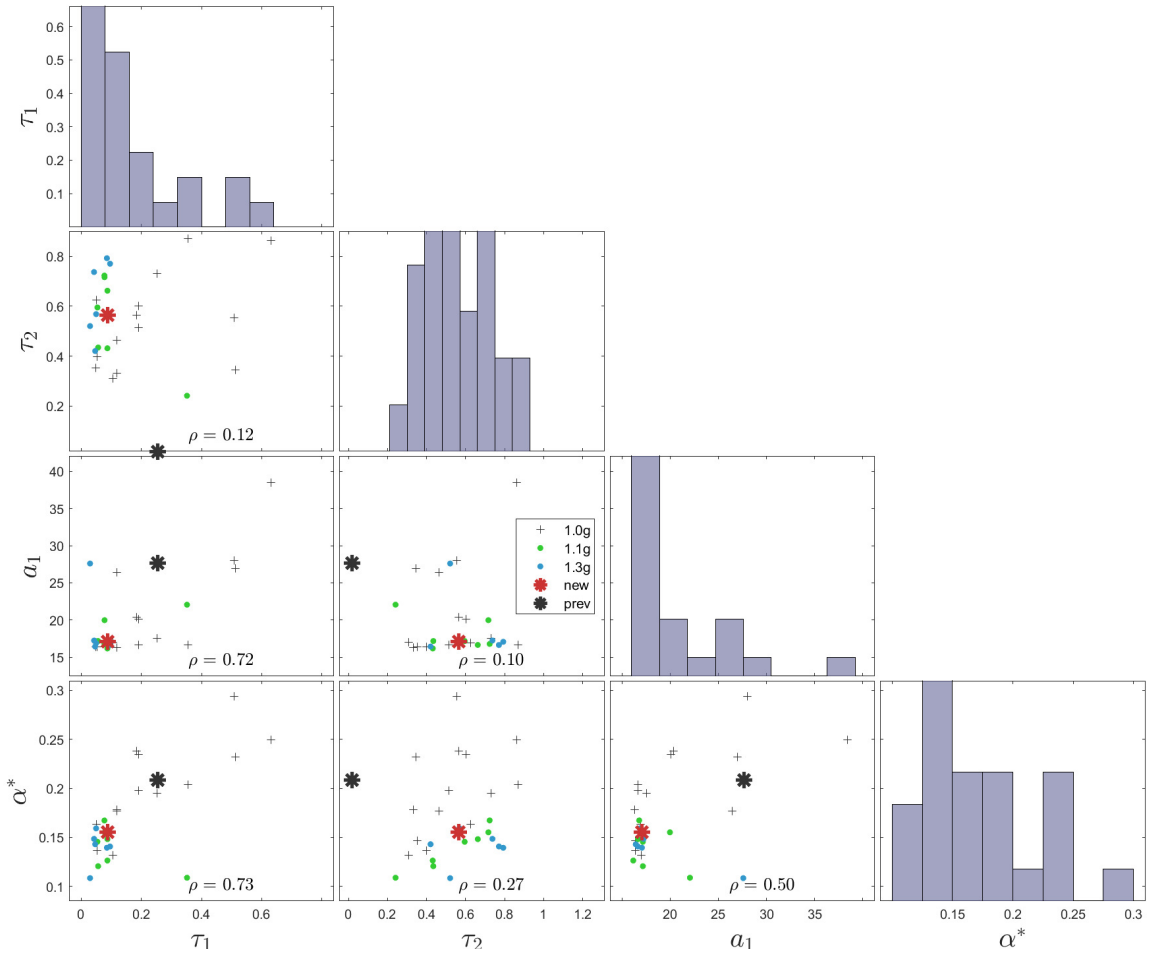


**Figure 6.1:** The $X$-parameter estimations of the *van Ingen* data set, including the final estimate of the previous stall model [9].

From Table 6.1 it can be seen that the bounds of $\tau_2$ were altered for the proposed method. As is evident from Figure 6.1, generally the optimization would converge in a much higher range than for the previous approach. Changing the upper bound was necessary to avoid the estimates clustering around this bound.

In general, the estimated parameter variances are of similar magnitude as for the previous method, except for $\tau_2$. A likely explanation for this result is the fact that previously this parameter was estimated to be close to zero, or its lower bound. When many estimates are at the bound, the variance is small but it does not necessarily provide more reliability.

An important observation is made when considering the grouping of the estimates in Figure 6.1. A large part of the variance seems to originate from the symmetric stall maneuvers (1.0g). While the estimates of the sets corresponding to accelerated stall maneuvers are fairly clustered, the symmetric stall estimates are scattered. A possible cause of this result is the fact that the $X$-parameters are estimated through the roll moment. During symmetric stalls there is a relatively small roll moment signal with respect to accelerated stalls, potentially resulting in estimation difficulties. This would confirm that the *Asym* data set is more suitable for the proposed estimation method, as it does not include any symmetric stalls.

In general, it is evident that the estimated parameters of the proposed method are significantly different from van Ingen's lift-based estimations. For instance, $\alpha^*$ is estimated approximately 0.05 rad below the previous estimation, which would indicate the wing is at 50% flow separation at an AOA of approximately 9°. Also, the $a_1$ estimates imply a significantly less abrupt stall behavior. Furthermore, while the lift-based approach resulted in $\tau_2$ estimates close to zero, the proposed method returns much larger estimates.

Conversely, the $\tau_1$ estimates of the proposed method are clustered close to zero. Hence, while the estimation method is successful in estimating parameters with sufficiently low variances, the physical interpretation of the newly gained parameters could be changed.

### 6.1.2. Asym Data Set

A similar plot matrix is presented in Figure 6.2, which depicts the results of the proposed estimation method for the *Asym* data set. Since no symmetric stalls are included in the *Asym* data set, the outliers that were found with the *van Ingen* data set have disappeared. However, the new training sets introduce a new source of spread in the estimates. Surprisingly, the training set that included 5 consecutive stalls (indicated as "2022 1.1g 5x" in the legend) is estimated close to the final estimate. Since only one of such a maneuver is included in the training data set, no strong conclusions can be made from this result.

The final parameter estimations, the optimization bounds and the standard deviation can be found in Table 6.1. Note that the standard deviations of the newly estimated parameters of the *Asym* data set are all lower than that of the *van Ingen* data set. This is likely in part due to the removal of symmetric stalls in the data set. Moreover, the *Asym* data set has a slightly smaller training set than *van Ingen*; 24 versus 27, respectively.

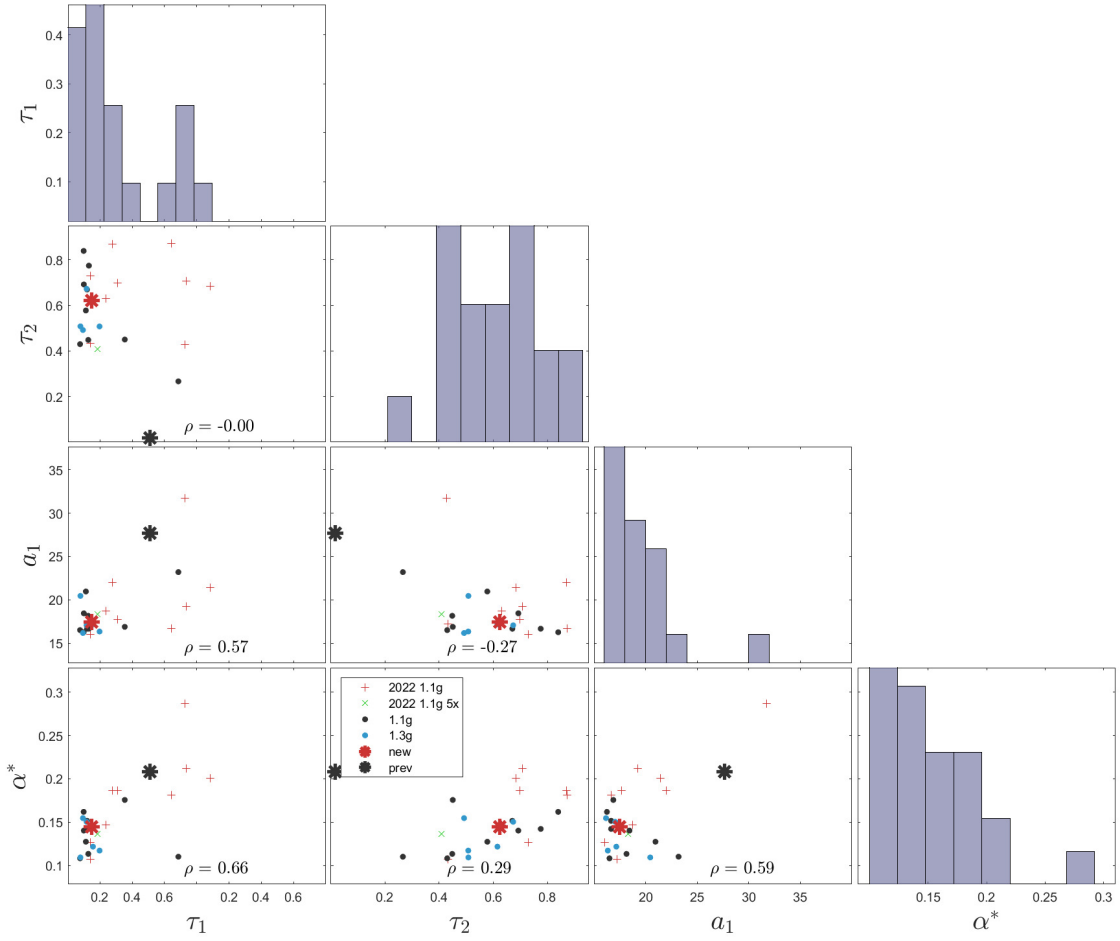


**Figure 6.2:** The $X$-parameter estimations of the *Asym* data set, including the final estimate of the previous stall model [9].

## 6.2. Statistical Tests

The results of the statistical tests that are described in Section 5.4.6 are presented in Table 6.2. The tests are only applied to the results of the newly proposed method.

For all KS-tests a significance level of $\alpha = 0.1$ was used. The output column of the KS-test $h$ indicates 'N' when the population distribution can be assumed to be approximately normal, and 'X' when this is not the case. The $p$-value associated with the test is displayed in the $p$-column. For *van Ingen*, only $\tau_1$ and $a_1$ cannot be considered to originate from a normal distribution. As can be seen in the histograms, both parameter estimates are clustered relatively close to the lower optimization bound. This could have a strong influence on the test statistic. For future iterations, it could be worth-wile to reduce the lower bound slightly and observe the results of the KS-test. However, a stronger indication of an unsuitable bound would be observing that the estimates are clustered *at* the lower bound, instead of close to it.

For *Asym* only the $\tau_1$ estimates cannot be considered to be sampled from a normal distribution. Again, the estimates are largely clustered around the lower bound. However, the new maneuvers seem to be making the distribution closer to normal, as evidenced by the higher KS-test $p$-value for *Asym* with respect to *van Ingen*. This increase in $p$-value is observed even more strongly for the $a_1$ estimates, which are concluded to be normally distributed according to the KS-test.

The output columns $h$ of the $t$-test and Wilcoxon's signed rank test are indicated by an asterisk if the data suggests that the real parameter is significantly different from zero. The significance level was chosen to be $\alpha = 0.01$ with a Bonferroni correction. It can be clearly seen from Figure 6.1 and Figure 6.2 that for both data sets all parameter estimates are nonzero. The results of these tests indicate therefore unsurprisingly, that the real parameters have significant nonzero values.

| | **van Ingen** | | | | | | **Asym** | | | | | |
|---|---|---|---|---|---|---|---|---|---|---|---|---|
| | **KS-test** | | **$t$-test** | | **Signed rank** | | **KS-test** | | **$t$-test** | | **Signed rank** | |
| $\theta$ | $h$ | $p$ | $h$ | $p$ | $h$ | $p$ | $h$ | $p$ | $h$ | $p$ | $h$ | $p$ |
| $\tau_1$ $[s]$ | X | 0.025 | * | 0.000 | * | 0.000 | X | 0.075 | * | 0.000 | * | 0.000 |
| $\tau_2$ $[s]$ | N | 0.883 | * | 0.000 | * | 0.000 | N | 0.754 | * | 0.000 | * | 0.000 |
| $a_1$ $[-]$ | X | 0.005 | * | 0.000 | * | 0.000 | N | 0.192 | * | 0.000 | * | 0.000 |
| $\alpha^*$ $[rad]$ | N | 0.458 | * | 0.000 | * | 0.000 | N | 0.647 | * | 0.000 | * | 0.000 |

**Table 6.2:** Results of statistical tests performed on the $X$-parameter estimates on the *van Ingen* and *Asym* data sets.

## 6.3. Cost Function Analysis

In order to get an idea of the shape of the cost function, it is evaluated for one of the training sets. This is done at 50 grid-points for the $X$-parameters within the optimization bounds. The result is presented in Figure 6.3, in 4 different plots that describe the cost function while varying the parameters on the horizontal axes.

The cost function surface tends to be rough for higher values of $\tau_1$ and $\tau_2$. Since the optimization method uses the gradient of the cost function with respect to the parameters, this could lead to complications. $\tau_1$ is rarely estimated at these higher regions but $\tau_2$ is generally estimated between 0.4 and 0.8; significantly higher than previous research has found.

## 6.4. Parameter Sensitivity Analysis

When considering only the accelerated stall sets, the static parameters $a_1$ and $\alpha^*$ are estimated with relatively low variance, while the dynamic parameters $\tau_1$ and $\tau_2$ show a wider range of estimates. This phenomenon was observed for the previous method. A possible explanation was that the sensitivity of the model output with respect to changes in the static parameters was larger than the sensitivity with respect to changes in the dynamic parameters. Since the model output of the proposed method is the roll moment coefficient, a sensitivity analysis is done to evaluate this hypothesis.

Figure 6.4 presents the result of the analysis. For every $X$-parameter, the baseline model output is evaluated along with the model output from 4 different deviations from the parameter value. They are

multiplied by the factors 0.33, 0.67, 1, 1.33, and 1.667. The remaining parameters are held constant at the estimated value. The figure also features a plot with the AOA and the flow separation during this maneuver.

Note that the roll moment is sensitive to changes in the static $X$-parameters during stall but also before stall occurs. This is also the case, to a lesser degree, for the dynamic parameters. Previously, when the relevant model output was the lift coefficient, it was found that the lift model output was completely insensitive to changes in the dynamic parameters outside the stall regime [9]. The discrepancy likely originates from the fact that the $a_1$ and $\alpha^*$ estimates are significantly lower than the previous estimates. This results in a less sudden, but earlier stall onset, as is demonstrated by the flow separation plot in Figure 6.4.

Furthermore, the least sensitivity is found with respect to changes in parameter $\tau_1$. This is also in contrast with the results of previous method, where $\tau_2$ was clearly the weakest contributor. A possible explanation for this discrepancy could be the fact that the $\tau_2$ estimates were mostly evaluated close to zero, while significantly higher estimates occur for the current approach. For the previous approach, $\tau_2$ generally seemed of less importance than any other $X$-parameter to the model output.

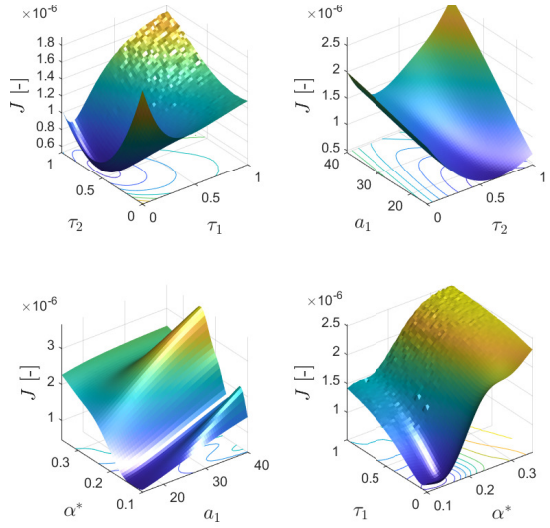


**Figure 6.3:** Cost function visualization for four different pairs of $X$-parameters.

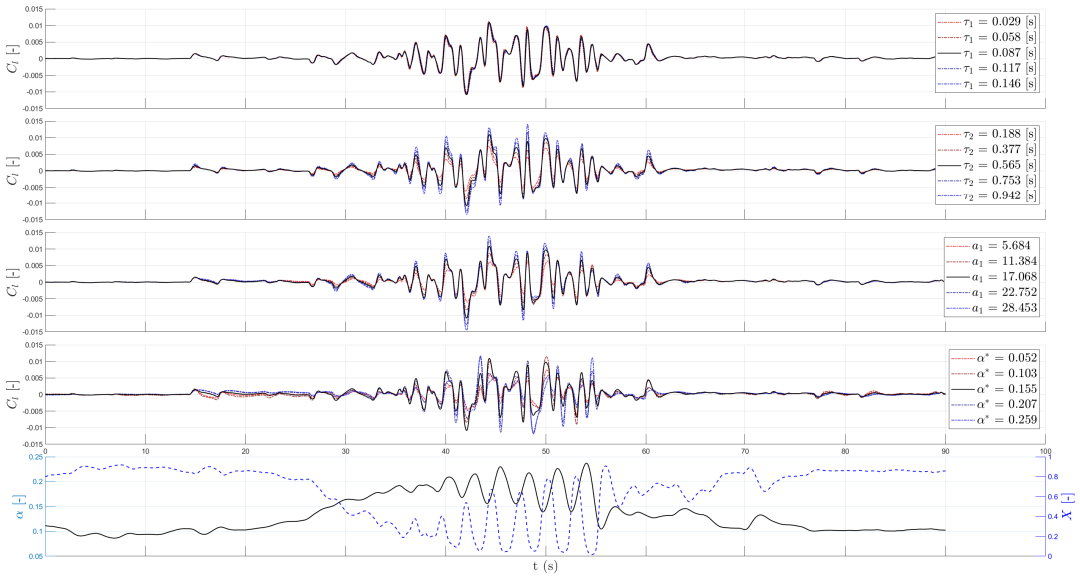


**Figure 6.4:** Sensitivity analysis of the roll moment coefficient model output with respect to the $X$-parameters, for an example maneuver that was used for training.

# 7

# Conclusion and Research Plan

This chapter holds the preliminary conclusions of this thesis. The conclusions that can be made at this stage are presented first. Finally, an action plan is made for the research questions that cannot be fully answered with the current knowledge and results.

## 7.1. Conclusion

This research has set out to improve the model fidelity of the Cessna Citation II dynamic stall model. A novel system identification approach is designed and implemented, with the objective of identifying asymmetric stall characteristics and potential changes in lateral-directional control surface effectiveness.

The parameters describing the flow separation over a wing, according to Kirchhoff's model of flow separation, the $X$-parameters, are estimated at the left and the right wing. The novelty of the approach is the estimation of these parameters through the minimization of the roll moment model error, for a predetermined roll model. The $X$-parameters are assumed to be equal at both wings.

As a result of this preliminary phase of implementation and analysis, some of the research questions that were posed can be (partially) answered. For others a plan is described that will allow for conclusions at the final stage of the thesis.

*1. Which flight test maneuvers and control inputs are suitable for identifying lateral-directional stall behavior, including potential changes in control surface effectiveness?*

From literature and earlier efforts of the stall task force, a set of recommendations was incorporated into the data set selection of this stall model. In order to observe changes in control surface effectiveness it is recommended to apply control inputs inside the stall-regime and outside the stall-regime. To account for this, the aileron inputs that are required for the accelerated stall are included in the maneuver sets.

The hypothesis was stated that asymmetrical stall effects would be better identifiable when only including accelerated stalls in the data set. To evaluate this hypothesis the proposed $X$-parameter estimation method was applied to the data set from an earlier stall model (*van Ingen*), which included symmetric stalls, and a new data set (*Asym*) with only accelerated stalls. The *van Ingen* data set is split into 27 training sets and 7 validation sets, whereas *Asym* is split into 24 training sets and 8 validation sets. Preliminary results of the $X$-parameter estimation step suggest that the proposed method estimates the parameters more reliably when no symmetric stalls are included in the data set.

Furthermore, due to limited flight time and technical difficulties some of the new stall maneuvers were performed in a closely-following manner. They were combined into one training set. Preliminary $X$-parameter estimation results suggest that this data synthesis method leads to similar parameter estimates. However, since this is only the case for one training set it would be premature to conclude that this method is suitable; more of these maneuvers would have to be flown.

*2. How can the local angle of attack of the aircraft wings be determined?*

The local AOA can be computed by applying a kinematic relationship, which describes the angle of attack at an arbitrary point on a rigid body subjected to a rotation. Note that this is an approximation of the actual local AOA, as the aircraft is in fact not a rigid body and local airflow effects can exist at the wing.

*3. Which nonlinear parameter estimation methodology is suitable for efficient and sufficiently accurate estimation of the parameters of the selected stall model structure from flight data?*

Previous efforts within the research group have led to a successful stall model, particularly the longitudinal model. The proposed parameter estimation methodology builds on the earlier approach; the flow separation parameters are estimated through a nonlinear estimation approach, after which the flow separation variables are computed and fixed. A model structure selection algorithm is employed, where (transformations of) the fixed flow separation variables are included as possible model terms. Finally, a least-squares approach is used for the linear estimation of the aerodynamic coefficient models.

The proposed methodology uses the roll moment coefficient measurement and a suitable roll moment model for the estimation of flow separation over the two wings, in an attempt to improve the fit of the lateral-directional model.

*4. How can the parameters that describe the flow separation point be identified from the flight-derived roll moment coefficient and a suitable roll moment model structure?*

Results of the proposed estimation approach indicate that the $X$-parameters can be estimated with sufficiently low variances. This evaluation is done by applying the proposed approach on the *van Ingen* data set and comparing the resulting estimate variance. Subsequently applying the method on the *Asym* data set results in slightly smaller estimate variances, which is likely due to the absence of symmetric stall maneuvers in the data set.

Statistical tests indicate that some of the $X$-parameter estimates cannot be assumed to be sampled from a normal distribution. This result can be attributed to the fact that these parameters are estimated close to the lower optimization bound. Additional statistical tests indicate that the real parameter values can be assumed to be significantly larger than zero.

The $X$-parameter estimates significantly differ from the results of van Ingen's lift-based approach. The physical interpretation of the new estimates is less straightforward than for previous methods, as they describe the flow separation over a single wing, instead of the integral wing. For instance, the results show significantly lower estimates of both $\alpha^*$ and $a_1$, indicating an earlier but less abrupt stall onset at the wing than at the CG. Furthermore, while the lift-based approach resulted in $\tau_2$ estimates close to zero, the proposed method results in larger $\tau_2$ estimates. However, the $\tau_1$ estimates of the proposed method are clustered close to zero. Possibly these dynamic parameters have an ambiguous effect on the optimization.

*5. What modifications to Kirchhoff's flow separation model are required to enable it to effectively model asymmetric stall behavior and variations in control surface effectiveness?*

As of the current preliminary stage, only the initial roll model structure is selected. A requirement of the initial roll model is the inclusion of the flow separation point. The roll moment is modeled as a lift differential between the wings. This is mathematically described by subtracting Kirchhoff's model for the lift for the individual wings. The remaining terms are based on successful previous stall modeling attempts. The model structures of all aerodynamic parameters will be selected in the following stage of this thesis.

## 7.2. Remaining Research Plan

The research methodology of Chapter I is revisited in this section. At the current stage, the literature study, flight data gathering and data set selection are completed. In order to achieve the objectives of this research, a set of actions are developed for the remaining phases.

**Flight Path Reconstruction** While the used FPR method has been shown to be effective, an adjustment can be made that could potentially improve the model. The local AOA on each wing is currently computed after the FPR step, using the reconstructed body velocities and rates. Instead, the local AOAs can be determined through the UKF, by adding them to the observation model, as described in Section 3.3.2. This requires two additional observation equations. This option will be investigated in the remaining research period.

**Nonlinear parameter estimation** The estimated $X$-parameters significantly differ from earlier estimations. A more detailed investigation should follow to evaluate the physical interpretation of these parameters. For instance, the large difference in the estimation of the time constants $\tau_1$ and $\tau_2$ could be due to their ambiguous contributions to the roll model output; these parameters could be modeling the same

phenomena. These parameters could be better identifiable using a lift-based approach.

The parameters can be estimated at several spanwise locations over the wings to evaluate (1) the sensitivity of the parameter estimates to the spanwise location and (2) the spanwise flow separation distribution.

Currently, the $X$-parameters on each wing are assumed equal. This assumption neglects possible local differences in flow conditions. This also means that the only difference between the progression of $X_L$ and $X_R$ is due to differences in local AOA. An alternative methodology can be proposed where each wing has its own flow separation parameters. Note that this approach would complicate the problem significantly as 4 new parameters are introduced into the optimization problem. Moreover, the left and right $X$-parameters are likely highly correlated, which could lead to additional optimization difficulties.

**Model structure selection** A pool of possible model terms is introduced. This pool includes variables that describe flow separation, such as $X$, $X_L$ and $X_R$. Changes in control surface effectiveness can also possibly be described using these variables. A pre-implemented semi-objective model structure selection algorithm using multivariate orthogonal functions will be applied to evaluate the usefulness of the all model terms in the pool.

**Future iterations of the parameter identification approach** The results that are described in this preliminary thesis are limited to the first iteration of the $X$-parameter estimation step. An initial roll moment model is proposed based on a transformation of Kirchhoff's flow separation model. While this model is critical for the $X$-parameter estimation, it is not guaranteed to be the most suitable model structure. If in the model structure selection procedure a different model is found to be more suitable, the initial model is updated. This could lead to significantly different $X$-parameter estimates in the following iteration.

**Changes in control surface effectiveness** In order to identify changes in control surface effectiveness, a model term must be selected that combines a flow separation variable with a control deflection. Including such a term for aileron effectiveness in the roll moment model could change the $X$-parameter estimates of the following iteration significantly. The model structure selection procedure of that iteration could yield results that indicate a different change in aileron effectiveness than for the previous iteration. A method must be developed to converge to a single model structure that can be used for the $X$-parameter estimation and the aerodynamic parameters.

**Linear parameter estimation** The aerodynamic model parameters will be estimated through OLS. An analysis on the residuals could be performed to identify whether the white noise assumption of the OLS method is reasonable. Possibly, WLS can be applied to improve the results of the linear parameter estimation step.

**Validation** The final aerodynamic model will be validated by evaluating the fit on the validation sets. The metrics to be used are MSE, VAF, $R^2$ and Theil's statistic. Other options are possible and should be further investigated. Since no ground-truth is available for the $X$-parameters, objective metrics such as MSE are not applicable to validation of the $X$-parameters. A simple comparison with previous $X$-parameter estimations is likely the best validation approach.

# Part IV

## Thesis Conclusion

# Thesis Conclusion

The most important findings and conclusions of this research were summarized in the scientific paper of Part II. In this thesis conclusion, the research definition of Part I is revisited, to provide direct answers to the research questions, and to offer recommendations for future work. Note that the answers to sub-questions 4 and 5 overlap, and are therefore treated simultaneously.

**Research Question 1**

Which flight test maneuvers and control inputs are suitable for identifying lateral-directional stall behavior, including potential variations in control surface effectiveness?

Exclusively accelerated stall maneuvers were included in the identification data set. Quasi-random disturbance inputs and 3-2-1-1 inputs were applied on the aileron during the stall to maximally excite the aircraft dynamics. Every maneuver also included Quasi-random disturbance inputs on the elevator. A novel approach was introduced: a subset of the stall maneuvers was performed with a reference sideslip angle.

Using the selected roll moment model structure, the results of the $X$-parameter estimates are found to be insensitive to the type of dynamic aileron input. Note that the alternative proposed model structure did lead to larger differences. Using the selected model structure and the current laboratory aircraft, 3-2-1-1 inputs are preferred, as they can be performed automatically for reliable roll axis excitation.

The inclusion of stall maneuvers with a reference sideslip angle ensured the application of sufficient rudder inputs. This resulted in the model term related to rudder deflection having significant contributions to the yaw moment and the lateral force models.

The current methodology and flight data did not provide a method of modeling variations in aileron effectiveness during the stall. For future work, it is recommended to include dynamic inputs during the stall approach, to better identify the difference in the response of the aircraft in the nominal region, with respect to the stall region.

**Research Question 2**

How can the local angle of attack of the aircraft wings be determined?

A kinematic equation is employed, assuming rigid body dynamics. The lateral location at which the angle of attack is computed is the lateral location of the MAC. This lateral location also describes the moment arm of the individual wing surface lift vector, with respect to the fuselage center line. Hence, ideally, this offset would be set equal to the lateral position of the center of lift of a single wing surface, However, this choice seems mostly arbitrary, as the parameter associated with the flow separation regressor simply scales, while identified flow separation characteristics are equal.

**Research Question 3**

Which nonlinear parameter estimation methodology is suitable for efficient and sufficiently accurate estimation of the parameters of the selected stall model structure from flight data?

The efficient two-step method developed by van Ingen et al. [9] was altered. The flow separation parameters were identified using nonlinear optimization, from the flight-derived roll moment coefficient, instead of the lift coefficient. Subsequently, the flow separation variables were computed and fixed. OLS was applied to obtain the optimal aerodynamic model parameter estimates. The method was found to be effective, as both optimizations result in similar parameter estimates. Furthermore, it is efficient, as only a single computationally expensive nonlinear optimization is required, instead of one for each degree of freedom (6).

The proposed roll moment-based method leads to significantly different flow separation parameter

estimates than the lift-based baseline model. To test whether they are suitable for longitudinal stall modeling, the selected longitudinal model structures from the baseline model were evaluated using these parameters. The model fit deteriorated in comparison with the baseline model. As a solution, a hybrid Kirchhoff method is proposed. This method combines two sets of parameters, describing symmetric and asymmetric flow separation separately. The longitudinal models would be evaluated using the symmetric flow separation parameters (obtained through the lift), whereas the lateral-directional models are evaluated using the asymmetric flow separation parameters (obtained through the roll moment).

**Research Question 4**

How can the parameters that describe the flow separation point be identified from the roll moment coefficient measurement and a suitable roll moment model structure?

**Research Question 5**

What modifications to Kirchhoff's flow separation model are required to enable it to effectively model asymmetric stall behavior and variations in control surface effectiveness?

Two asymmetric stall regressors were proposed for the roll moment model structures. For the first option, the lift of each wing surface was modeled using Kirchhoff's theory of flow separation, using an individual flow separation variable for each wing. The introduced model term consists of this lift differential multiplied by some moment arm. For the second option, a simpler model was proposed. Appreciating the fact that other regressors such as the rotational rates and control surface deflections are capable of describing a large part of the lift differential, only the flow separation differential is considered.

Incorporating the second choice into the roll moment model structure resulted in parameter estimates that were more consistent and reliable. After conducting OLS, this also yielded an improved model fit compared to the first option.

It was found that both proposed regressors showcase correlations with the roll rate, leading to difficulties with parameter estimation. For the first option, the degree of correlation was found to be highly dependent on the amount of flow separation. In general, the second option was less correlated with the roll rate, and the dependency on the flow separation variable was weaker. However, in both cases, the roll rate was not found to be of sufficient explanatory value to include it in the roll moment model. For future applications, it was recommended to include a spline term of the first option, which is only active in the stall region. This would allow for the addition of the roll rate, without the parameter estimation complications of strong correlations.

The asymmetric stall regressor (the second option) was selected in the roll moment, yaw moment, and lateral force models, to describe the stall-related dynamics. As mentioned, the flow separation variables were ineffective at describing variations in aileron effectiveness. Assuming the flight data contains enough information to identify these changes, perhaps a more suitable transformation of these variables exists that describes these variations accurately. Further research on the development of control surface effectiveness with flow separation is required to propose such a model.

# References


[1] Boeing. *Statistical Summary of Commercial Jet Airplane Accidents 1959-2017*. Tech. rep. 2017.

[2] International Civil Aviation Organization. *Aviation Occurrence Categories: Definitions and Usage Notes*. Tech. rep. 2011.

[3] Federal Aviation Administration. *Advisory Circular 120-109A - Stall Prevention and Recovery Training*. Tech. rep. 2015. URL: https://www.faa.gov/regulations_policies/advisory_circulars/index.cfm/go/document.information/documentID/1028646.

[4] D.R. Gingras et al. "Flight simulator augmentation for stall and upset training". In: *AIAA Modeling and Simulation Technologies Conference 2014* January (2014), pp. 1–14. DOI: 10.2514/6.2014-1003.

[5] D. Fischenberg. "Identification of an unsteady aerodynamic stall model from flight test data". In: *20th Atmospheric Flight Mechanics Conference Baltimore, MD, USA*. American Institute of Aeronautics and Astronautics Inc, AIAA, 1995, pp. 138–146. DOI: 10.2514/6.1995-3438. URL: https://arc.aiaa.org/doi/10.2514/6.1995-3438.

[6] J. Singh et al. "Flight determination of configurational effects on aircraft stall behavior". In: *21st Atmospheric Flight Mechanics Conference San Diego, CA, USA*. Vol. 33. 3. American Institute of Aeronautics and Astronautics, May 1996, pp. 657–665. DOI: 10.2514/6.1996-3441. URL: http://arc.aiaa.org.

[7] E.A. Morelli et al. "Global Aerodynamic Modeling for Stall/Upset Recovery Training Using Efficient Piloted Flight Test Techniques". In: *AIAA Modeling and Simulation Technologies (MST) Conference Boston, MA, USA*. 2013. DOI: https://doi.org/10.2514/6.2013-4976. URL: https://arc.aiaa.org/doi/10.2514/6.2013-4976.

[8] J.N. Dias. "High angle of attack model identification with compressibility effects". In: *AIAA Atmospheric Flight Mechanics Conference, 2015*. American Institute of Aeronautics and Astronautics Inc., 2015. DOI: 10.2514/6.2015-1477.

[9] J.B. van Ingen et al. "Stall model identification of a cessna citation II from flight test data using orthogonal model structure selection". In: *AIAA Scitech 2021 Forum Virtual Event* (2021), pp. 1–29. DOI: 10.2514/6.2021-1725. URL: https://arc.aiaa.org/doi/10.2514/6.2021-1725.

[10] J. Singh et al. "Identification of lateral-directional behavior in stall from flight data". In: *Journal of Aircraft* 33.3 (May 1995), pp. 627–630. DOI: 10.2514/3.46993. URL: https://arc.aiaa.org/doi/10.2514/3.46993.

[11] D. Fischenberg et al. "Identification of Aircraft Stall Behavior from Flight Test Data". In: *RTO SCI Symposium on System Identification for Integrated Aircraft Development and Flight Testing Madrid, Spain*. 1998. DOI: https://doi.org/10.2514/6.1996-3441. URL: https://arc.aiaa.org/doi/abs/10.2514/6.1996-3441.

[12] A Delfosse et al. "Asymmetric Stall and Control Effectiveness reduction Modeling for the Cessna Citation II". PhD thesis. 2022.

[13] L.J. Van Horssen et al. "Aerodynamic Stall and Buffet Modeling for the Cessna Citation II Based on Flight Test Data". In: *AIAA Modeling and Simulation Technologies Conference*. 2018. DOI: 10.2514/6.2018-1167. URL: http://arc.aiaa.org.

[14] J.D. Anderson. *Fundamentals of Aerodynamics (Mcgraw Hill Series in Aeronautical and Aerospace Engineering)*. 5th ed. Mcgraw Hill, 2009.

[15] M. Fouda et al. "Effect of Wing Planform on Airplane Stability and Control Authority in Stall". In: *AIAA Science and Technology Forum and Exposition, AIAA SciTech Forum 2022 San DIego, CA, USA* (2022). DOI: 10.2514/6.2022-1161.

[16] S.R. Jacobson. “Aircraft Loss of Control Causal Factors and Mitigation Challenges”. In: Toronto: NASA, Aug. 2010.

[17] J.A. Mulder et al. *Lecture Notes AE3202 Flight Dynamics*. Delft: Delft University Of Technology, Mar. 2013.

[18] J.R. Chambers et al. *historical review of uncommanded lateral-directional motions at transonic conditions (invited)*. 2003.

[19] J.R. Chambers et al. *Aerodynamic Characteristics of Airplanes at High Angles of Attack*. Tech. rep. Hampton, VA, USA: NASA, 1977. URL: https://ntrs.nasa.gov/archive/nasa/casi.ntrs.nasa.gov/19780005068.pdf.

[20] J.V. Foster et al. “Dynamics modeling and simulation of large transport airplanes in upset conditions”. In: *Collection of Technical Papers - AIAA Guidance, Navigation, and Control Conference*. Vol. 2. 2005, pp. 826–838. DOI: 10.2514/6.2005-5933.

[21] E.J. Jumper et al. “Lift-curve characteristics for an airfoil pitching at constant rate”. In: *AIAA Paper* (1986). DOI: 10.2514/6.1986-117. URL: https://arc.aiaa.org/doi/10.2514/6.1986-117.

[22] D.E. Hewes. *NASA Memo 5-20-59L Low-Subsonic Measurements of the Static and Oscillatory Lateral Stability Derivatives of a Sweptback-Wing Airplane Configuration from -10 to 90 deg*. Tech. rep. 1959.

[23] J.R. Chambers et al. *Analysis of lateral directional stability characteristics of a twin jet fighter airplane at high angles of attack*. Tech. rep. Hampton, VA, USA: NASA, 1969. URL: https://ntrs.nasa.gov/citations/19690022959.

[24] L.T. Nguyen. “Evaluation of importance of lateral acceleration derivatives in extraction of lateral-directional derivatives at high angles of attack”. In: *NASA technical note* (1974).

[25] B.J. Eulrich et al. *Identification and Correlation of the F-4E Stall/Post-Stall Aerodynamic Stability and Control Characteristics from Existing Test Data*. Tech. rep. Buffalo, NY, USA, 1973.

[26] K. Iliff et al. *Subsonic Stability and Control Derivatives for an Unpowered, Remotely Piloted 3/8-scale F-15 Airplane Model Obtained From Flight Test*. Tech. rep. Edwards, CA, USA: NASA, 1976. URL: https://ntrs.nasa.gov/citations/19760008088.

[27] K J Orlik-Ruckemann. “Aerodynamic aspects of aircraft dynamics at high angles of attack”. In: (Aug. 1982). DOI: 10.2514/6.1982-1363. URL: https://arc.aiaa.org/doi/10.2514/6.1982-1363.

[28] J.R. Chambers et al. “Summary of NASA stall/spin research for general aviation configurations”. In: 1986.

[29] M. Sri-Jayantha et al. “Determination of Nonlinear Aerodynamic Coefficients using the Estimation-Before-Modeling Methods”. In: *IFAC Proceedings Volumes* 18.5 (July 1985), pp. 837–844. DOI: 10.1016/S1474-6670(17)60666-9.

[30] J. Batterson et al. “Partitioning of flight data for aerodynamic modeling of aircraft at high angles of attack”. In: *14th Atmospheric Flight Mechanics Conference*. Reston, Virigina: American Institute of Aeronautics and Astronautics, Aug. 1987. DOI: 10.2514/6.1987-2621. URL: http://arc.aiaa.org/doi/10.2514/6.1987-2621.

[31] J.G. Leishman et al. “State-space model for unsteady airfoil behavior and dynamic stall”. In: *30th Structures, Structural Dynamics and Materials Conference Mobile, AL, USA*. Vol. 28. 5. American Institute of Aeronautics and Astronautics (AIAA), Apr. 1989. DOI: 10.2514/6.1989-1319. URL: https://arc.aiaa.org/doi/10.2514/6.1989-1319.

[32] M. Goman et al. “State-space representation of aerodynamic characteristics of an aircraft at high angles of attack”. In: *Astrodynamics Conference Hilton Head Island, SC, USA*. American Institute of Aeronautics and Astronautics Inc, AIAA, 1992, pp. 759–766. DOI: 10.2514/6.1992-4651. URL: https://arc.aiaa.org/doi/10.2514/6.1992-4651.

[33] Gwang gyo Seo et al. “Kalman-filter based online system identification of fixed-wing aircraft in upset condition”. In: *Aerospace Science and Technology* 89 (June 2019), pp. 307–317. DOI: 10.1016/J.AST.2019.04.012.

[34] R.V. Jategaonkar et al. “Identification of C-160 Simulator Data Base from Flight Data”. In: *IFAC Proceedings Volumes* 27.8 (July 1994), pp. 1031–1038. DOI: 10.1016/S1474-6670(17)47844-X.

[35] M. Fouda et al. “Experimental Investigations of Airplane Maneuverability and Stability in Stall”. In: (2021). DOI: 10.2514/6.2021-1819. URL: http://arc.aiaa.org.

[36] V Klein et al. *Aircraft System Identification: Theory and Practice*. AIAA, 2006.

[37] Federal Aviation Administration. *14 CFR Part 60 - Flight Simulation Training Device Initial and Continuing Qualification and Use*. Tech. rep. 2016. URL: https://www.ecfr.gov/current/title-14/chapter-I/subchapter-D/part-60.

[38] R. Koehler et al. “Auslegung von Eingangssignalen fur die Kennwerter-mittlung”. In: *DFVLR-IB* (1977), pp. 154–77.

[39] E. Plaetschke et al. “Flight Test Results of Five Input Signals for Aircraft Parameter Identification”. In: *IFAC Proceedings Volumes* 15.4 (June 1982), pp. 1149–1154. DOI: 10.1016/S1474-6670(17)63152-5.

[40] S.L. Julier. “The scaled unscented transformation”. In: *Proceedings of the 2002 American Control Conference* 6 (2002), pp. 4555–4559.

[41] M. Laban. “On-Line Aircraft Aerodynamic Model Identification”. PhD thesis. 1994. URL: https://repository.tudelft.nl/islandora/object/uuid%3A5183a61a-4263-4e70-964a-f8501f725398.

[42] B. L. Walcott et al. “Comparative study of non-linear state-observation techniques”. In: *International Journal of Control* 45.6 (June 1987), pp. 2109–2132. DOI: 10.1080/00207178708933870. URL: https://www.tandfonline.com/doi/full/10.1080/00207178708933870.

[43] C.C. de Visser. “Global Nonlinear Model Identification with Multivariate Splines”. PhD thesis. Delft University of Technology, 2011.

[44] J. Nocedal et al. *Nocedal, Wright - 2006 - Numerical Optimization (2nd Ed.)* 2nd ed. 2006.

[45] J. Norsett et al. *Solving Ordinary Differential Equations I*. Springer Berlin Heidelberg, 1993. DOI: 10.1007/978-3-540-78862-1.

[46] S. Boyd et al. *Convex Optimization*. New York: Cambridge University Press, 2004. URL: http://www.cambridge.org.

[47] J.R. Leis et al. *The Simultaneous Solution and Sensitivity Analysis of Systems Described by Ordinary Differential Equations*. Tech. rep. 1988.

[48] F.J. Massey. “The Kolmogorov-Smirnov Test for Goodness of Fit”. In: *Journal of the American Statistical Association* 46.253 (Mar. 1951), pp. 68–78. DOI: 10.2307/2280095.

[49] J.D. Gibbons et al. “Nonparametric Statistical Inference”. In: (July 2010). DOI: 10.1201/9781439896129. URL: https://www.taylorfrancis.com/books/mono/10.1201/9781439896129/nonparametric-statistical-inference-jean-dickinson-gibbons-subhabrata-chakraborti.